SISSA/ISAS
Scuola Internazionale Superiore di Studi Avanzati
International School for Advanced Studies

The Warm Ionized Gas thin layer

Thesis submitted for the degree of
“Doctor Philosophiæ”
In
Astrophysics

CANDIDATE

Roberta Paladini

SUPERVISORS

Prof. Gianfranco DeZotti
Prof. Rod Davies
Prof. Luigi Danese

October 2003

Contents

List of Figures

List of Tables

Abstract

Among the phases of the interstellar gas, the warm ionized is the least known. Its spatial distribution is characterized by a thin and a thick layer where the former corresponds to the ionized gas in the proximity of the plane and the latter to the gas which is found at larger distances from the plane. The thin layer comprises discrete HII regions and diffuse gas. Despite the important role assigned to the thin layer by current theoretical models, so far our knowledge of it has been based either on oversimplified analytical calculations or on the scattered observational information coming from pulsar dispersion and scattering measures which largely suffer from undersampling.

In this Thesis, after an overview of the current knowledge of the Galactic interstellar medium and of its constituents, and particularly of the warm ionized medium, we focus on our main goal which is to contribute to build a realistic picture of the thin layer by exploiting the information widely spread in the literature. This work has proceeded along two main lines: the systematic investigation of the thin-layer source-component, i.e. HII regions, and the study of the interplay between this source-component and the diffuse gas.

Collecting radio data on Galactic HII regions from 24 published works, we have built a self-consistent data base comprising 1442 sources. This work has resulted in the construction of a Master Catalog (which consists in 11 sub-catalogs storing the original information from the source references) and of a Synthetic Catalog (which is a readily accessible version of the Master Catalog at 2.7 GHz). This represents the most extensive list of compact HII regions to date. We have then exploited this data-base to investigate the distribution of the warm ionized gas, as well as for applications in the field of Cosmic Microwave Background studies (calibration, beam-shape and pointing reconstruction, straylight, understanding of the Galactic foregrounds).

The kinematic information contained in the catalog has allowed us to study the spatial distribution of 550 objects taken from the Synthetic Catalog. For each source, a galactocentric distance has been derived using the Fich et al. [106] rotation model. We have found a highly significant correlation between luminosities and linear diameters, which was exploited to resolve the solar-distance degeneracy. We have then been able to estimate the scale height of the HII region distribution. Within the solar circle, we have obtained an azimuthally-averaged thickness, $\sigma_z \simeq 52\,\mathrm{pc}$ which is comparable to the estimated scale height of the OB star distribution but narrower than that of the diffuse

HII and HI. The analysis of the z-distribution has retrieved other important results: a confirmation of the presence of the warp; evidence of an increasing width of the distribution as a function of the galactocentric radius; a confirmation of the electron temperature gradient with galactocentric radius; a spiral-like structure in agreement with the model by Taylor & Cordes [311].

The relationship between HII regions and the diffuse gas in the thin layer has been addressed by considering data at 408 MHz (Haslam et al. [150]) and at 5 GHz (Haynes et al. [151]) for the region of the Galactic Plane in the coordinate range $20^0 < l < 30^0$, $-1.5^0 < b < +1.5^0$. After adjusting the zero levels of the two surveys, we have applied a component separation technique to the observed radio continuum by exploiting the spectral dependence of the two kinds of emissions which overlap at these frequencies, namely free-free and synchrotron radiation. The synchrotron spectral index has been kept fixed during this phase of the analysis. The distribution of spectral indices for the total Galactic emission has been recovered across the considered region. Evidence of a flattening of the spectral index in proximity of the plane has been found. This has been interpreted as the effect of intense thermal emission due to HII regions. A comparison between the latitude distribution of the free-free and that of the HII regions located in this coordinate range has shown clearly the presence of diffuse gas in the thin layer. A preliminary estimate of the contribution of HII regions to the total emission budget has yielded a value of order of 11% which, again, supports the hypothesis of a dominant role of the diffuse ionized gas in the thin layer.

Finally, we want to point out that the analysis we have described has relied on radio data which, so far, have found limited applications in this context. The continuum free-free emission has long been considered (as in the case of experiments dedicated to the Cosmic Microwave Radiation) as a source of disturbance, rather than a source of information or, in other words, as a foreground to remove. This is mostly due to the fact that this emission is partly masked by intense synchrotron radiation produced by relativistic electrons accelerated in the Galactic magnetic field. However such data, when properly handled, have the unique advantage with respect to other tracers of providing access to the distribution of Galactic warm ionized gas without suffering from undersampling or extinction. The same advantages also characterize radio recombination lines. So far, due to the limited instrumental capabilities, it was not possible to exploit fully the wealth of information contained in these data. Yet, the next generation of experiments will open up a new window on the warm ionized gas, allowing its systematic, unbiased exploration throughout the Galaxy.

Introduction

Our Galaxy contains, as well as stars, a significant amount of tenuous matter, inhomogeneously spread out throughout interstellar space. The interstellar matter, which exists in the form of gas (atoms, molecules, ions and electrons) and dust (tiny solid particles), manifests itself primarily through obscuration, reddening, polarization of starlight, formation of absorption lines in stellar spectra plus various continuum and line emission mechanisms.

While dark lanes of dusty clouds obscuring portions of the sky are celestial landmarks, the realization that interstellar gas pervades space is relatively quite recent. In 1904, Hartmann [147] discovered a nebulous mass of interstellar gas in the direction of the binary star δ Orionis. A series of over 40 spectra showed that the Ca II K (3933 Å) absorption line was nearly stationary in wavelength, extraordinary weak and almost perfectly sharp in contrast to broader variable stellar absorption features. This fact was interpreted with the presence of a stationary absorbing cloud of vapor between the binary system and the observer. The Ca II and Na I lines constituted the primary tracer for interstellar gas during the first half of the century.

Since then, our knowledge of the interstellar gas has largely improved. Today we know that the gas in the galactic interstellar medium (ISM) is mainly hydrogen (around 70% by mass) and is present in three different thermal phases: molecular, neutral and ionized. These phases are mutually tightly coupled so that a global understanding of the process through which matter in the Galaxy is locked into stars and then recycled into the ISM requires detailed knowledge of each of its constituents.

The least known among the ISM gas phases is the ionized one for which several tracers exist. Ionizing radiation in our Galaxy is associated with massive O and B stars which, consequently, appear to be surrounded by the so-called HII regions. However, ionized hydrogen is also observed far from regions of stars formation. The first detection outside well-defined HII regions was reported by Struve & Elvey [309] who detected Hα and [O_{II}] 3727 Å emission from extended zones in Cygnus and Cepheus. Systematic studies of this gas, through its optical emission lines, did not begin until over 30 years later, with, amongst the others, an important Hα photographic survey by Sivan [294] and more sensitive Hα spectroscopic scans by Roesler et al. [267]. What emerged from this observational studies is that diffuse ionized gas exterior to HII regions exists in all directions around us. Further high-resolution Hα observations of selected portions of the sky have shown a complex structure made of patches, filaments and loops of enhanced Hα emission superimposed on a fainter background (Reynolds [258]; Reynolds et al. [263]). In the near future, a detailed view of the morphology and kinematics of the Hα-emitting gas will be provided by the combined information obtained from recently completed extensive surveys such as the Wisconsin H Alpha Mapper project (WHAM) and the Southern H Alpha Sky Survey Atlas (SHASSA), complemented by observations of the ongoing Virginia Tech Spectral-line Survey (VTSS), Manchester Wide Field Camera (MWFC) and the AAO/UK Schmidt Hα survey.

A real breakthrough in the investigation of the warm ionized gas has been due to pulsar dispersion and scattering measures which have started after the discovery of the first pulsar (Hewish et al. [161]). Thanks to these kind of measures, the modelling of the large-scale distribution of free electrons has begun. The electron density models have gradually been refined: from the simplified, axisymmetric models by Manchester & Taylor [206], Harding & Harding [146] and Vivekanand & Narayan [332] to the more elaborated versions by Taylor & Cordes [311], Cordes & Lazio [67], [68] which also include a spiral-arm component and local clumps of over/under dense regions. The development of such models has also led to the introduction of the systematic distinction between a thin and a thick layer in the description of the spatial distribution of the Galactic warm ionized gas.

The refinements of the observing technique has been important for starting the investigation of the source of the widespread ionization. Current theoretical (Reynolds [255]; Miller & Cox [223]; Dove & Shull [92]; Domgörgen & Mathis [91]; Elmergreen [100]) models seem to favor a scenario in which ultraviolet photons emitted by OB stars escape regions of star formation and cause ionization of interstellar material far from OB associations facilitated by the fractal distribution of the intracloud medium (ICM). The relevance of the role of the thin layer, i.e. the site of star formation in the Galaxy, then seems to have been clearly assessed and motivates the work which is here presented.

The Thesis is organized as follows. In Chapter 1 we review the Interstellar Medium and, in particular, the gas component and its different thermal phases (molecular, neutral and ionized). In Chapter 2 we focus on the WIM and we discuss the reasons motivating its investigation, the properties of the different tracers and the state-of-the-art of the modelling. We also provide definitions of the thick and thin layers. In Chapter 3, we describe the construction of an extensive radio catalog (1442 objects) of Galactic HII regions. Details of the Master Catalog and of the Synthetic Catalog are given. This vast data base provides the necessary information which so far has not been available for a systematic investigation of the thin-layer source-component. Chapter 4 discusses the reconstruction of the spatial distribution for 550 HII regions which was made possible thanks to the extensive kinematic information contained in the catalog. The analysis allows the estimate of the scale height of the HII region distribution. Other results include the confirmation of the presence of the warp and a characterization of its properties, the evidence of an increasing thickening of the z-distribution with galactocentric radius, the confirmation of the electron temperature gradient with distance from the Galactic centre, and the tracing of the spiral-arm shape, found to be consistent with the model proposed by Taylor & Cordes [311]. Chapter 5 outlines applications of the HII region catalog in fields other than the study of the warm ionized gas. Such applications range from calibration, straylight, beam-shape and pointing reconstruction for Cosmic Microwave Background experiments to studies of the Galactic foregrounds. In Chapter 6, we present a preliminary analysis of the diffuse component of the thin layer. In particular, we describe: the considered radio continuum data base; the procedure for adjusting the zero levels; the applied spectral component technique; the latitude distribution of the recovered free-free and a preliminary estimate of the contribution of HII regions to the total observed thermal bremsstrahlung emission. Finally, the main results of the Thesis and the future developments of the work are summarized in the Conclusions.

Chapter 1

The Interstellar Gas

1.1 General properties

The interstellar gas is one of the constituents of the Interstellar Medium (ISM), together with dust and cosmic rays. In high-density, low-temperatures regions, this gas is tightly coupled to cosmic dust. Roughly 10-15% of the total mass of the Galaxy is stored in the interstellar matter of which 70.4% is hydrogen, 28.1% is helium and 1.5% are heavier elements (Ferriere [104]). This matter appears to be extremely rarefied having an average density of 2.7×10^{-24} g cm^{-3} which, by comparison, is twenty orders of magnitudes smaller than the density in the Earth's lower atmosphere. The interstellar mass is mainly concentrated on the Galactic plane and, in particular, along the spiral arms where half of it is distributed in discrete cold atomic/molecular clouds. These clouds have typically a temperature between a few tens and a few hundreds of K. The remaining interstellar matter is present in three different phases: warm neutral atomic ($T < 10^4$ K), warm ionized ($T \sim 10^4$ K) and hot ionized ($T \sim 10^6$ K).
In the following sections (1.2.1, 1.2.2, 1.2.3 and 1.2.4) we present a brief overview of the main observational properties of the various phases of the interstellar gas while, for an extensive discussion on the ionized phase, we refer the reader to Chapter 2.

1.2 The thermal phases of the Interstellar Gas

1.2.1 The molecular phase

- **General properties.** Molecular clouds are characterized by relatively high densities ($\sim 10^{-18}$ g cm^{-3}) and low temperatures ($T \sim$ 10-20 K) and contain in their interior a significant amount of dust grains. The observed temperatures can be explained theoretically through the interplay of two simultaneous physical processes, that is: heating of the clouds due to cosmic rays and cooling by line emission (mainly CO) (de Jong et al. [82]; Goldsmith [127]; Hollenbach and Tielens [166]).

These clouds appear to be organized hierarchically from giant complexes (with a size of a few tens of parsecs and a mass of up to 10^6 $M_\odot$) down to small dense cores (with a size of a few parsecs and a mass $\sim$ 0.3-10^3 $M_\odot$) (Larson [193]; Goldsmith [127]). The most abundant molecules in the ISM are, respectively, H_2 and CO. H_2 molecules are believed to form by recombination of hydrogen atoms on the surface of interstellar dust grains (Hollenbach and Salpeter [165]) and once formed, they survive in the interior of dark clouds which provide, at the same time, a shield from the stellar UV radiation and a low enough temperature to avoid collisional dissociations (Shull and Beckwith [289]).

- **Observational techniques.** Due to dust extinction, optical and UV observations do not allow us to trace the spatial distribution of the molecular clouds on Galactic scale. Most of the information on interstellar clouds comes instead from observations at radio wavelengths of the next most abundant molecules in the ISM: CO. H_2 molecules, in fact, cannot be probed directly at radio frequencies since their electric dipole moment is not permanent, their moment of inertia is very small and all their permitted transitions lie outside the radio domain. On the contrary, the CO molecule is characterized by a rotational transition at millimetric wavelenghts (2.6 mm). This emission line represents the primary tracer of molecular gas in the ISM.

- **Radial distribution.** From CO observations we know that most of the molecular material resides in a well-defined ring extending radially between 3.5 and 7 kpc from the Galactic Center and that a strong molecular concentration is present within 0.4 kpc from the center[1] (Scoville and Solomon [280]; Burton et al. [48]). Moreover, CO concentrations tend to reproduce the spiral pattern (Fig 1.1) which is also suggested by other tracers (see section 1.2.2 and 1.2.3) (Dame et al. [75]). In the inner Galaxy $(R < R_0)$[2] interarm regions are not devoid of molecular gas and the space-averaged density is only a factor $\sim$ 3.6 lower than in the arms (Clemens et al. [60]). However, the ratio between the molecular surface density in the spiral arms and in the interarm regions is much greater in the outer Galaxy $(R > R_0)$ with a mean value of 13 (Grabelsky et al. [136]; Heyer [160]). As for the azimuthally averaged distribution, the most striking feature is that the molecular material appears to be almost entirely confined to the inner Galaxy: 77% of the $\sim 10^9$ $M_\odot$ of the Galactic molecular mass lies inside R_0 (see Fig 1.2, Binney & Merrifield [20]).

- **Vertical distribution.** As for the z-dependence[3], Bronfman et al. ([40]) and Clemens et al. ([60]) find a strong concentration of the molecular material along the Galactic plane. However, Bronfman et al. report for $R < R_0$ a full-width at half-maximum (FWHM) for the molecular z-distribution fitted by a Gaussian of

---

[1] The IAU recommended value $R_0 = 8.5$ (Kerr and Lynden-Bell [181]) has been assumed for the Galactocentric radius of the Sun.

[2] R denotes the Galactocentric distance.

[3] z denotes the distance from the Galactic plane.

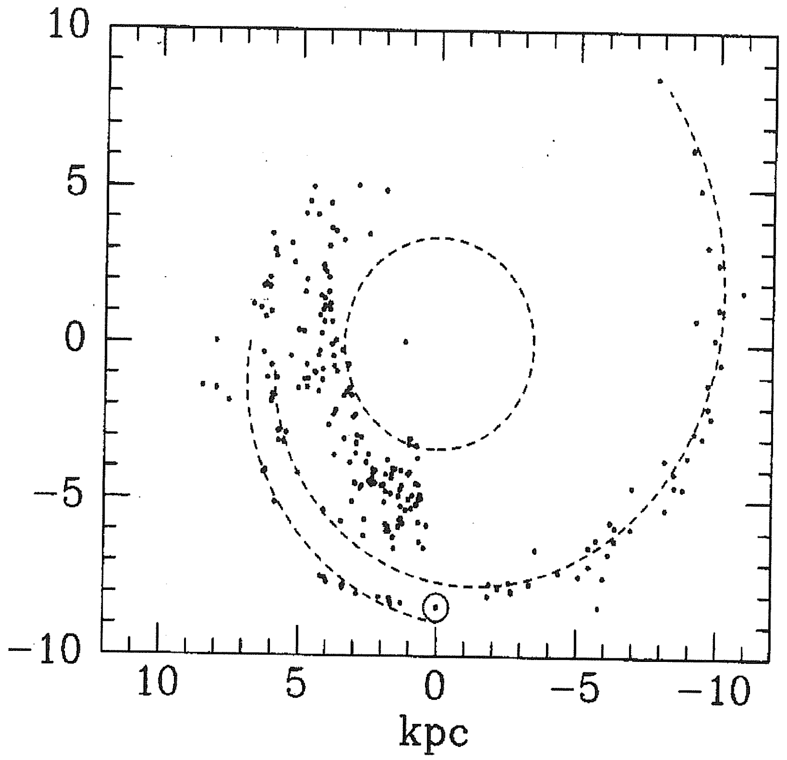

Figure 1.1: The diagram (dots) shows the estimated positions of giants molecular in the Galaxy. The figure is based on the assumption of perfectly circular orbits. The Galactic center is at the coordinate origin and the Sun's location is denoted with ⊙. The Sagittarius-Carina arm is drawn as a logarithmic spiral, together with a section of the Orion-Cygnus arm. A dotted circle of radius $0.4R_0$ illustrates the extended distribution of clouds in the molecular ring (Binney & Merrifield [20]).

120±18 pc, weakly increasing with R (Fig 1.3) and a space-averaged density of hydrogen in molecular form:

$$n_m(z) = (0.53\, cm^{-3})\, exp\left[-\left(\frac{z}{71}\right)^2\right] \tag{1.1}$$

Clemens et al. find a FWHM of 136±17 pc at the solar circle and a more pronounced thickening of the molecular layer towards the outer Galaxy. For the space-averaged density, they find:

$$n_m(z) = (0.58\, cm^{-3})\, exp\left[-\left(\frac{z}{81}\right)^2\right] \tag{1.2}$$

1.2.2 The atomic phase

- **General properties.** Two components can be distinguished in the interstellar neutral atomic hydrogen (HI) distribution: a cold component, whose temperature falls in the range 50-140 K and a warm component for which much higher temperatures ($\simeq$ 500-5000 K) are estimated (Heiles 2001 [158]). The cold HI is characterized by an average density $\sim$ 20-50 atom cm^{-3} which is two orders of magnitudes larger than the warm HI density (Kulkarni and Heiles [191]). The co-existence of these two HI phases can be explained theoretically (Field et al. [107]; Goldsmith et al. [126]): atomic interstellar gas heated by low-energy cosmic rays has two thermally stable phases, i.e. a cold dense phase, in which the primary cooling mechanism is the radiative de-excitation of collisionally excited states of metals, and a warm phase resulting from the onset of Lyman α cooling.

- **Observational techniques.** In order to trace the HI distribution in the ISM, two different radiative mechanisms can be exploited: on one side, since neutral hydrogen in the interstellar clouds is mainly in the ground state, all the electronic transitions between the ground level and an excited state result into emission of a Lyman series photon and, in particular, the transition between the ground level and the first excited state generates a Lyα photon at 1216 Å; at the same time, the ground state of atomic hydrogen is split into two hyperfine levels by the interaction between the spins of the electron and the proton; the atom energy is 6×10^{-6} eV lower when the two spins are antiparallel than when they are parallel and photons with frequency ν=1.4204 GHz (equivalent to λ=21.105 cm) are emitted or absorbed in the transitions between the two levels.
  Although Lyα surveys are useful to investigate the distribution of HI in the vicinity of the Sun (and have allowed the discovery of the so-called *Local Bubble*, an asymmetric region surrouding the Sun devoid of neutral hydrogen, with a radius of 60-100 pc and a vertical extent across the plane $\sim$ 120-180 pc (Breitschwerdt et al. [35]), they are limited by extinction and cannot be used to probe extensively the distribution of HI in the Galaxy. Our knowledge on the large scale distribution of interstellar HI is rather based on 21-cm line surveys.

- **Radial distribution.** From these observations, HI is found to extend radially up to 30 kpc from the Galactic center (Diplas and Savage [90]) and to be distributed, in the Galactic plane, in long-arc features which are organized in a spiral pattern (Oort et al. [232]; Mihalas and Binney [221]). Despite the fact that a better picture of this spiral structure is delineated by other tracers (such as molecular clouds and, especially, HII regions) which have a higher arm-interarm density gradient, are less ubiquitous and for which complementary information to the kinematic one is available[4], still important indications can be obtained from 21-cm observations. In the inner Galaxy ($R < R_0$), the spiral pattern appears in a very fuzzy way,

---

[4] For a detailed discussion on kinematic data and the problem of distance ambiguity, the reader is referred to Chapter 3.

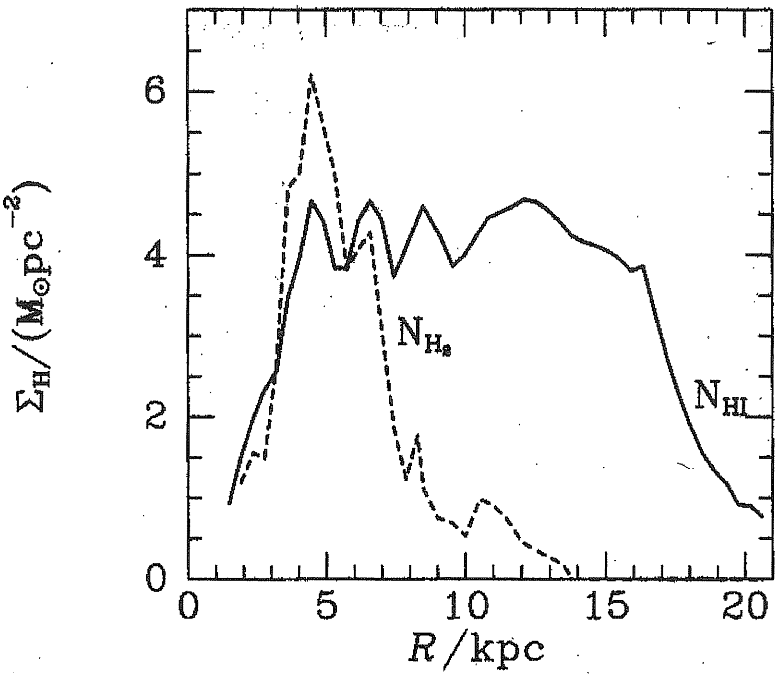

Figure 1.2: Solid curve: average density of HI in an annulus around the Galactic center, versus radius of the annulus. Dashed curve: corresponding surface density of molecular gas (Binney & Merrifield [20]).

mainly due to the uncertainties of distances (see Chapter 3). Outside the solar circle ($R > R_0$), this region is unaffected by distance ambiguities and the situation is more clear: three major arms stand out in addition to the local minor Orion arm (Kulkarni et al. [189]; Henderson et al. [159]) and these arms have a quite constant surface density which is about four times greater than in the interarm regions (Kulkarni et al. [189])
As for the azimuthally-averaged density, for $R < 4$ kpc, the density falls from a wide plateau to near zero inside 1.5 kpc. Beyond R_0, the density remains high up to $R \simeq 16$ kpc where it turns sharply downwards (Binney & Merrifield [20], Fig 1.2). This behaviour of the HI surface density implies that ~ 80 % of the $\sim 4.3 \times 10^9$ $M_\odot$ of Galactic neutral hydrogen lies beyond R_0.

- **Vertical distribution.** The vertical structure of the HI distribution is characterized by very interesting features. First of all, the central value of z, z_c, resulting from different tracers, as a function of both R and the azimuthal coordinate ϕ, defines a surface which is very close to a plane in the range 3 kpc $< R < R_0$, suggesting an extreme flatness of the distribution. However, some deviations are observed and these oscillations (also known as *corrugations*) appear to be coherent and are common to every Population-I object. The origin of this phenomenon is still matter of debate. As for the vertical scale height, this is approximately constant for 3.5 kpc $< R < R_0$ (Lockman [198], Fig 1.3) where the HI lies in a layer whose FWHM is $\sim$ 230 pc (Dickey & Lockman [87]) and its space-averaged density can be approximated by the sum of two Gaussians and an exponential tail:

$$n_e(z) = (0.57\,cm^{-3})\left\{0.70\,exp\left[-\left(\frac{z}{127\,pc}\right)^2\right]\right. \\ \left.+0.19\,exp\left[-\left(\frac{z}{318\,pc}\right)^2\right] + 0.11\,exp\left(-\frac{|z|}{403\,pc}\right)\right\} \tag{1.3}$$

(Dickey & Lockman [87]). In this expression, the first Gaussian term accounts for the cold neutral gas while the second term, which is the sum of a Gaussian plus an exponential tail, stands for the contribution given by the warm neutral gas. At $R > R_0$, the HI layer thickens more than linearly with R reaching a scale height of $\sim$ 1 kpc (Diplas and Savage [90]). This phenomenon is theoretically expected from the steep decrease in the gravitational potential toward the outer Galaxy (Fig 1.3). This flaring is accompanied, at $\sim 1.5R_0$, by a warp of the HI disk whose origin has not been clarified yet. The warp appears, in the first and second quadrants, as a positive displacement of the HI midplane with respect to the Galactic plane of $\sim$ 4 kpc; in the third and fourth quadrants, the effect is reversed and the displacement is negative with a maximum value of -1.5 kpc (Dickey & Lockman [87]; Diplas and Savage [90]). For $R > 11$ kpc, a reasonable approximation to the behaviour of the warp is given by:

$$z_c = \frac{R/kpc - 11}{6}\sin\phi + 0.3\left(\frac{R/kpc - 11}{6}\right)^2 (1 - \cos 2\phi)\ kpc \tag{1.4}$$

(Binney & Merrifield [20]).

- **Peculiar phenomena.** Despite most of the atomic interstellar gas obeys Galactic differential rotation, nevertheless a few anomalies are detected. These fall into two categories: on one side we find *shells*, on the other we have the so-called *high-velocity clouds*. Shells (and super shells) are expanding dynamical systems with diameters ranging from a few tens of parsecs to $\sim$ 2 kpc and with expansion velocities reaching a few tens of km s^{-1} (Heiles [153]; Heiles [154]). The majority of shells are thought to be created by stellar winds and supernova explosions acting either individually or within associations of up to a few thousands stellar objects (Tenorio-Tagle and Bodenheimer [315]). However, the most energetic supershells are presumably produced by the impact on the Galactic disk of high-velocity clouds (Tenorio-Tagle and Bodenheimer [315]). These clouds have been revealed by early 21-cm surveys and are observed both at low and high latitudes at velocities that differ by more than 50 km s^{-1} from those associated with normal differential motion

(Verschuur [333]). Their origin is not completely understood. It has been suggested that they can be the result of gravitational interaction between our own Galaxy and nearby systems as it might be the case for the Magellanic Stream Clouds (Murai and Fujimoto [226]). An alternative explanation is that these clouds may be connected with the observed Galactic warp (Lockman [202]).

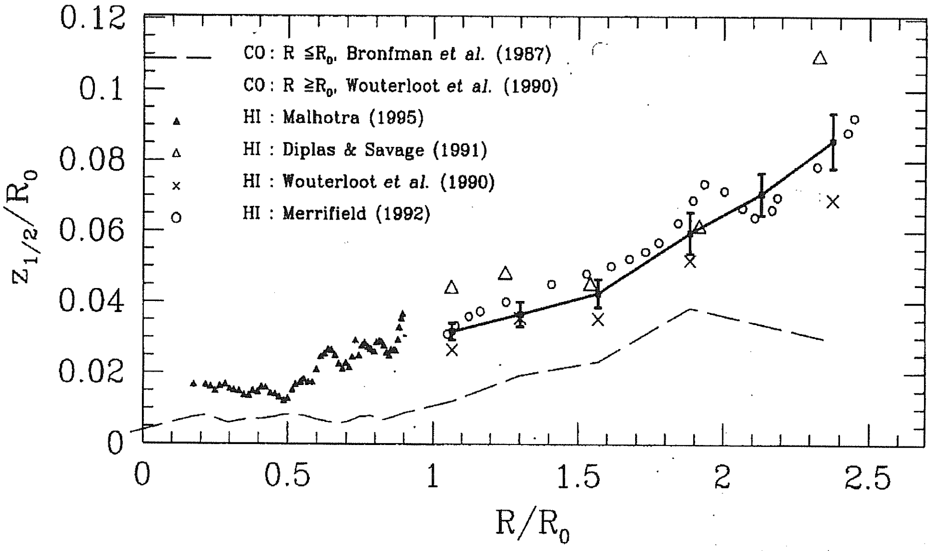

Figure 1.3: The half thickness at half-maximum intensity of the neutral and molecular gas as traced by HI and CO. The plot shows the increase in thickness with radius. Results from various data sets are plotted for HI; the solid line and error bars indicate the average and standard error of these values (Binney & Merrifield [20]).

1.2.3 The warm ionized phase

We outline here for completeness also the main observational properties of the warm ionized gas. However, each topic will be discussed extensively in Chapter 2.

- **General properties.** Below a wavelength of 912 Å (which corresponds to an energy of 13.6 eV), electromagnetic radiation is powerful enough to ionize interstellar hydrogen. Such ionizing radiation can be found in the ISM in correspondence to massive O and B stars which are completely surrounded by the so-called *HII regions* (where HII denotes the ionized hydrogen). However, HII is also largely detected outside regions of star formation and the origin of this phenomenon is still unclear. The typical temperature of ionized-hydrogen systems within the ISM is $\sim$ 8000 K and this value is common to both traditional HII regions and diffuse ionized gas. Electron densities span a wide range of values, from $10^5 - 10^6$ cm^{-3} for HII regions down to $0.2 - 0.5$ cm^{-3} for the diffuse gas.

- **Observational techniques.** The warm ionized gas can be probed by means of different tracers. All observational techniques are based on the assumption that helium is largely neutral in the warm ionized gas (Reynolds and Tufte [261]; Heiles [157]; Tufte [322]) and, as a consequence, we can derive the ionized-hydrogen space-averaged density from the free-electron space-averaged density.
  At radio wavelengths, HII emits brehmsstrahlung or *free-free* radiation which arises from the interaction between free electrons and the Coulomb field of the positive ions (H^+, He^+ and He^{2+}). Emission recombination lines are also detected at these wavelengths, as well as in the infrared and optical band. Particularly important are the optical lines of the Balmer series which are produced by electronic transitions between an excited state n $>$ 2 and the first excited state n=2. The integrated intensity of these lines is in fact a direct measure of the free-electron column density along the line of sight. The most used among the Balmer series lines is the $H\alpha$ which is due to transitions from n=3 and n=2 and has a wavelength of 6563 Å. However, $H\alpha$ surveys suffer from the problem of extinction and cannot probe regions of the Galaxy more distant than 2-3 kpc. An alternative technique to $H\alpha$, offering the advantage of not being limited by dust obscuration, is represented by the detection of signals from pulsars. This method is based on the very well-known fact that the variation of pulse arrival time with frequency is the result of dispersive propagation through the ionized medium. Complementary information is given by scattering measures: pulsar signals, in fact, not only experience dispersion but also scattering when they propagate in an ionized medium and the amount of scattering is proportional to the spatial fluctuations of the electron density along the line of sight.

- **Radial distribution.** Due to our fragmented knowledge on the sources of ionizing radiation, the reconstructed radial distribution of the warm ionized gas is quite model-dependent. The widely used model by Taylor & Cordes ([311]), which is built by considering dispersion and scattering measures data, as well as data on HII regions, includes three components: a spiral arm component; an annular ring centered at 3.5 kpc (which should correspond to the annular ring observed for molecular clouds) and a radially extended component with a Gaussian scale length $\geq$ 20 kpc.

- **Vertical distribution.** The z-distribution parallels the radial distribution. The best-fit models contain: a thin-disk component (annular ring-like), a thick-disk component, a spiral arm component plus localized regions of higher-than-average electron density (e.g. the Gum Nebula) (Taylor & Cordes [311], Cordes & Lazio [67], [68]). In the solar neighboroughood the space-averaged density of free electrons can be approximated by:

$$n_e(z) = (0.015\, cm^{-3})\; exp\left(-\frac{|z|}{70\, pc}\right) + (0.025\, cm^{-3})\; exp\left(-\frac{|z|}{900\, pc}\right) \qquad (1.5)$$

(Reynolds [260]) , where the first term roughly represents the contribution from HII regions obtained from an analytical calculation (Lyne et al. [204]) and the second term corresponds to the thick-disk (or *diffuse*) component (Weisberg et al. [339]) and it is derived from pulsar dispersion measures at intermediate/high z.

1.2.4 The hot ionized phase

- **General properties.** The existence of hot gas in the Galaxy was first postulated by Spitzer ([304]) for whom a Galactic corona, filled with hot gas, would have provided the necessary pressure to confine the observed high-altitude interstellar clouds. Moreover, hot ionized gas in the Galaxy is predicted by models of galaxy-formation according to which, following dark-matter haloes merging, the gas in the halo is first shock-reheated at the virial temperature and then it cools radiatively as to collapse onto rotationally supported disks. A useful expression for the virial temperature is given by (Peacock [240]):

  $$T_{virial}/K = 10^{5.1}\,(M/10^{12}M_{\odot})^{2/3}(f_c\Omega h^2)^{1/3}(1+z_c) \tag{1.6}$$

  where M denotes the total mass of the gas in solar mass units, f_c and z_c are, respectively, the collapse factor and the collapse redshift. Currently, the presence of interstellar gas inside our Galaxy with a temperature of $\simeq 10^6$ K (Mc Cammon and Sanders [215]) has been fully assessed and is explained as the result, mainly, of supernova explosions and, to a lesser extent, of winds from the progenitor stars (McCray and Snow [216]; Spitzer [306]).

- **Observational techniques.** The primary tracers of hot ionized gas are UV absorption lines and soft X-rays emission. The first are produced by high-excitation ions that form only at very high temperatures. The most common for detection are O VI (with a doublet at 1032 Å and 1038 Å) and N V (with a doublet at 1239 Å and 1243 Å). These lines are very useful to probe the spatial distribution of the hot ionized medium since their integrated intensity is directly proportional to the column density of the considered ion along the line of sight. Moreover, the simultaneous determination of the degree of ionization and the linewidth of O VI has allowed to probe a cooler component of the hot ionized gas, at a temperature of a few 10^5 K (York [351]). Complementary information can be achieved through the ob servation of soft X-rays. In this frequency-band, observations are limited due to the fact that radiation is significantly absorbed by the intervening interstellar medium and the mean free path is only a few tens of parsecs. However, soft-X ray observations have given a significant contribution to shed some light on the spatial distribution of hot gas in the Galaxy. In the 0.1-0.3 keV range, the intensity of the emitted radiation varies of a factor five according to the considered direction and appears to be anticorrelated with neutral hydrogen column density. Snowden et al. ([298]) have suggested that the observed radiation can be explained as thermal emission from hot gas at 10^6 K originating from the Local Bubble whose boundaries are located at varying distances from the Sun therefore producing the variation in the X-ray intensity which is detected (*displacement model*). However, the performance of *shadowing observations* by ROSAT (Burrows and Mendenhall [47], Snowden et al. [299], Snowden et al. [300]) have demostrated that at least a significant fraction of this emission is produced outside the local cavity. In these observations, Galactic clouds are used as screens, therefore the lack of *shadowing* suggests that the observed flux arises in front on the cloud, locally while the opposite case implies that the emission at least partly originates beyond the cloud. Sidher et al. [290] have proposed a two-component model according to which the observed X-ray radiation is given by the superposition of two contributions, i. e., emission from the Galactic halo with T = $10^{6.2}$ K and emission from the Local Bubble at T = $10^{5.9}$ K.

- **Radial distribution.** From X-ray observations, the Galactic halo emission appears to vary significantly over the sky. The northern halo exhibits strong intensity enhancements superimposed on a relatively uniform background, thereby suggesting that the emitting gas has a patchy distribution. On the contrary, the southern halo is characterized by intensity gradients toward low latitudes, roughly consistent with a plane parallel distribution (Snowden et al. [301]). As for the radial distribution of the hot ionized gas, only some qualitative indications can be drawn and these are based on the observation of other spiral galaxies. Cui et al. ([74]) have measured the soft X-ray intensity of several high-latitude face-on spirals and have derived radial profiles for the emission measure of their hot component. The reconstructed profiles unambiguously show that the amount of hot gas decreases radially outward.

- **Vertical distribution.** The scale height of the distribution of hot ionized gas in our Galaxy is largely uncertain. The estimates of this quantity are commonly based on O VI and N V column density measures. However, different measures seem to retrieve different, and quite inconsistent, results. For example, in the case of O VI observations, Jenkins ([172], [173]) by fitting O VI data with an exponential along z find a scale height $\sim$ 300 pc, while Hurwitz and Bowyer ([168]) obtain $\sim$ 600 pc and Savage et al. ([271]) derive a value in the range 2.7-3.6 kpc. On the other hand, from N V measurements, Sembach and Savage ([281]) report an exponential scale height $\sim$ 1.6 kpc but Savage et al. ([270]), employing a different set of data, compute a value of 3.9±0.6 kpc. The confusion among different estimates increases even more when these numbers are compared to the values obtained by using other high-stage ions like C IV and Si IV for which Savage et al. ([270]) quote, respectively, a scale height of 4.4±0.6 and 5.1±0.7 kpc.

1.3 The models for the multi-phase ISM

The general picture for the ISM. The ISM is tightly coupled to the star formation history of the Galaxy. In practice, we can think of a closed loop formed by the coordinated interplay between the stars of our Galaxy and the interstellar medium and this loop can be summarized with a few steps. In the first step, new stars form out of interstellar material. This material, far from being uniformly spread throughout the interstellar space, displays large density and temperature gradients such that only the densest, coldest molecular regions offer an environment favorable to star formation. In these high-density regions, the interstellar gas tends to become gravitationally unstable and collapse into stars. Once locked into the interior of stars, the Galactic matter goes through a series of thermonuclear reactions which enrich it in heavy elements. A fraction of this matter eventually returns to the ISM either through stellar winds, during the star lifetime, or in supernova explosions. In both cases, the injection of stellar material into the ISM is accompanied by a strong release of energy which, in addition to generating turbulent motion in the ISM, contributes to mantaining its highly heterogeneous structure and, above all, induces star formation in new, high-density molecular regions. This is the final step which closes the ISM-star cycle.

The multi-phase ISM. Within this scenario, how to account for the observed multi-phase ISM (i.e., simultaneous co-existence of molecular, neutral and ionized gas) ? The realization that expanding SNR shells contain hot gas (Jones [176]; Cox and Smith [69]; Heiles [152]) has led to the classical McKee and Ostriker three-phase model (McKee & Ostriker [217]; McCray and Snow [216]). They have proposed that about 70% of the ISM volume consists of hot gas with a temperature of $\sim 10^6$ K. This hot gas would be contained in shells blown by SNRs and in tunnels formed by the merging of SNRs (Cox and Smith [69]) while the warm gas phase would occur at the interface of the hot gas and cold, neutral material. All three phases are assumed to be in hydrostatic equilibrium. Because the hot gas would be buoyant, it would rise up to the Galactic halo (Jones [176]) where it would cool and fall back onto the Galactic disk. This is the so-called *galactic fountains* theory (Shapiro and Field [282]). However, our current knowledge of the ISM partly contradicts the hypothesis of this model. In fact, observations and simulations indicate that: the ISM pressure is much higher than assumed due to the role played by magnetic fields and high-z gas (Cox [72]); the ISM contains gas systems which are far from hydrostatic equilibrium (Bregman et al. [34]) and are characterized by large, disordered motions; supernovae are spatially and temporally connected (Norman and Ikeuchi [227]) instead of being randomly spread throughout the disk; predicted fluxes in the soft X-rays associated to strong galactic fountains are not consistent with detections in the Galactic halo (Cox [70]; Heiles [155]).
Therefore, taking into account these constraints, plausible models have to be built on the following assumptions: the filling factor of the hot gas cannot go beyond 20% (Slavin and Cox [295]; Bregman [33]; Elmergreen [100]); SNRs are not connected by a network of tunnels of hot gas formed by SNR mergers but the hot gas morphology is characterized,

instead, by isolated superbubbles created by multiple simultaneous supernovae (Norman and Ikeuchi [227]; Spitzer [306]; Tenorio-Tagle et al. [316]); due to the increased ISM pressure, the efficiency of galactic fountains is reduced and only superbubbles driven by multiple SNRs are capable of breaking out the Galactic disk into the halo (McKee [218]; Kamaya et al. [177]); the morphology of the neutral gas is better represented by a diffuse layer with holes and shells, rather than the previous model of discrete cool clouds (Bregman and Ashe [29]; Bregman et al. [32]); the distribution of the warm ionized gas phase is extensive as the cool atomic gas and extends to large z-heights.

1.4 The distribution of stars in the Galaxy

Before analyzing in detail the properties of the WIM in the next chapter, we outline in this section the main features of the spatial distribution of stars in our Galaxy. As we have seen (section 1.3), stars in our Galaxy and the multiphase interstellar gas are tightly causally connected. We will focuse, in particular, on the radial and vertical distributions of O and B stars which produce, partly or completely, the warm ionized gas which is observed in the Galactic interstellar medium (see section 1.2.3 and Chapter 2).

The global distribution of stars. Thre are three major components which one can possibly distinguish when sketching the spatial distribution of stars in the Galaxy: a *disk* component; a *bulge* component and a *halo* component.

- **The disk distribution.** The disk distribution of stars has a diameter ranging between 40 and 50 kpc and presents three sub-components: the *young thin disk* is believed to have a vertical scale height of only about 50 pc (Carroll and Ostlie [51]) and is the region of current star formation. The *old thin disk* has a greater vertical scale height of roughly $z_{thin} \simeq 325$ pc (Carrol and Ostlie [51]) and the *thick disk* has a scale height of approximately $z_{thick} \simeq 1.4$ kpc (Carroll and Ostlie [51]). The stellar number density (i.e., the total number of stars per unite volume) of the thick disk is only about 2% of the combined values of the thin and thin disks (both young and old) at the Galactic midplane. Moreover, the mass of the thick disk is probably about 2 to $4\times\,10^9$ $M_\odot$, that is about 3% of the thin disks mass. When the young and old thin disks are combined, empirical fits to the stellar number density that are derived from star-count data give:

$$n(z,R) = n_0\,(e^{-z/z_{thin}} + 0.02\,e^{-z/z_{thick}})\,e^{-R/h_R} \qquad (1.7)$$

(Carroll and Ostlie [51]), where h_R is the disk scale length and n_0 is $\sim$ 0.02 stars pc^{-3} in the absolute magnitude range 4.5 *le* M_V *le* 9.5. However, it has to be pointed out that n_0, z_{thin}, z_{thick} and h_R are all uncertain coefficients and other similar fits may also fit the present observations.

The luminosity density (i.e., the luminosity per unit volume) of the old thin disk is often modeled with an exponential decay as follows:

$$L(z, R) = L_0 \, e^{-R/h_R} \, sech^2(z/z_0) \tag{1.8}$$

(Carroll and Ostlie [51]) where $z_0 = 2z_{thin}$ and $L_0 \simeq 0.05 \, L_\odot$ pc^{-3}. At the same time, the luminosity surface density (i.e, the luminosity per unit area) is written in the form:

$$\mu(r) = \mu_0 + 1.09 \left(\frac{r}{h_R}\right) \tag{1.9}$$

where μ_r has units of mag arcsec^{-2} and h_R has the same meaning as in eq. (1.7) and (1.8). The value of μ_0 appears to fall in an incredibly small range for spiral galaxies of the same Hubble-type. In particular, μ_0=21.52±0.39 B-mag arcsec^{-2} for Sc and earlier spiral galaxies and μ_0=22.61±0.47 B-mag arcsec^{-2} for Sd and later dwarf galaxies[5].
The thin and thick disks are also identifiable according to the different chemical composition. In the thin disk, typical values for the iron-hydrogen metallicity [6] ratio are in the range -0.5 < [Fe/H] < 0.3, while for the majority of stars in the thick disk, -0.6 < [Fe/H] < -0.4. From these values, it appears that the stellar members of the thin disk are probably significantly younger than the thick-disk counterparts.

- **The bulge distribution.** The bulge is a central concentrantion of stars with a scale height, symmetric above and below the plane, of ~ 1.5 kpc (Braccesi [30]) and a mass roughly 10^{10} M$_\odot$ (Carroll and Ostlie [51]). Althought it was originally thought to resemble a spheroid, it has now been assessed that it is rather bar-shaped inclined at a substantial angle to our line of sight. The scale height of the bulge (along the minor axis) appears to be of the order of 400 pc while the ratio of the minor to major axis is about 0.6. The surface brightness, I, of the bulge (measured in units of $L_\odot$ pc^{-2}) exhibits an approximate radial dependence of the form:

$$log_{10}\left[\frac{I(r)}{I_e}\right] = -3.3307\left[\left(\frac{r}{r_e}\right)^{1/4} - 1\right] \tag{1.10}$$

(de Vaucouleurs [84]) where $r_e \simeq 0.7$ kpc (Carroll and Ostlie [51]) is a reference radius (the so-called *effective radius*[7]) and I_e is the surface brightness at r_e.
The chemical abundances of stars in the bulge vary significantly, ranging from quite

---

[5] The Milky Way is classified as an Sbc-type galaxy or, given the observation of a bar-like structure in the bulge, as an SBbc.

[6] $\left[\frac{Fe}{H}\right] = log_{10}\left(\frac{N_{Fe}}{N_H}\right) - log_{10}\left(\frac{N_{Fe}}{N_H}\right)_\odot$

[7] It is defined to be the radius within which one half of the bulge light is emitted.

metal poor to very metal rich, i.e. -1 < $[F_e/H]$ < 1, with a mean value close to +0.3 (Carroll and Ostlie [51]). This may suggest that at least part of the stars in the bulge is young, although the age of the stellar population in this region of the Galaxy is still matter of debate.

- **The halo distribution.** The stellar halo is composed of globular clusters and *field stars* (stars which are not members of clusters) of which the majority is located very far from the Galactic plane. Although most of the clusters are found within 33 kpc of the Galactic center, several have also been observed between $66 < R < 100$ kpc. In particular, older, metal-poor clusters with $[Fe/H] <$ -0.8 belong to an extended spherical halo of stars, while younger clusters with $[Fe/H] >$ -0.8 form a much flatter distribution and may be associated with the thick disk. The number density profile of the metal-poor globular clusters and the field stars can be approximated by:

  $$n_{halo}(r) = n_{0,halo}\, r^{-3.5} \tag{1.11}$$

  (Carroll and Ostlie [51]) where $n_{0,halo}$ is roughly 0.2% of the thin disk midplane value. Moreover, the halo surface density is described by the de Vaucouleurs law with $r_e \sim 2.7$ kpc. The total mass of stellar halo is $\sim 10^9$ $M_\odot$ of which roughly 1% is the combined mass of globular clusters and the remaining is locked up in field stars.

The case of OB stars.

As we have seen in the previous sections (1.2.1, 1.2.2, 1.2.3), the disk of the Galaxy is characterized by a large scale structure delineated by the spiral arms. Among the most important tracers of the Galactic spiral pattern are OB stars. These are relatively young ($\sim$ 10 Myr) , luminous ($\sim 2 < \log(M/M_\odot) < 6$) and massive ($\sim 3 < M/M_\odot < 100$) stars, born in the very dense cores of giant molecular clouds and emitting an intense ultraviolet radiation. A detailed study of recently formed OB stars in the Galaxy has been carried out by Bronfman et al. [41]. These very young objects can be more easily probed than older OB stars: since they are still completely embedded in the dusty molecular environment in which they originate, their UV radiation, as well as ionizing the surrounding gas and producing HII regions (in this case, UCHII), also heats up the closeby dust which, in turn, reradiates most of the energy in the far infrared (FIR) where the ISM is more transparent. Bronfman et al., using data of CS(2-1) rotational line emission, have investigated the spatial distribution of 748 young OB stars and have compared it with the distribution of H_2 as derived from CO surveys of the Milky Way. From their analysis, by assuming purely circular motion and a linear rotation curve with the standard IAU constants[8], they conclude that:

---

[8] In Chapter 3, the concepts of circular motion and rotation curve will be laid out in detail.

1. massive star formation is distributed in a layer with its centroid $Z_0(R)$ following that of molecular gas for all galactocentric radii, both in the Northern and Southern Galactic emisphere;
2. the thickness of this layer for $R \leq R_0$ is $\sim$ 73 pc (FWHM), 62% the thickness of the molecular gas disk;
3. the warping of the disk outside the solar circle, as traced by the centroid Z_0 of both the OB distribution and the H_2 layer, appears to be more pronounced in the Northern Galaxy;
4. the flaring in the outer Galaxy is evidenced by both the massive star formation and the molecular layer: however, while the thickness of the massive star layer in the Northern outer Galaxy grows like that in the South, the mean thickness of the molecular hydrogen layer in the Northern outer Galaxy is only about half that of its Southrn counterpart

In addition, Bronfman et al. derive some conclusions on the FIR luminosity distribution. In particular: the FIR luminosity produced by young OB stars has a well defined maximum at $R = 0.55\ R_0$, with a gaussian FWHM of 0.28 R_0 compared with o.51 R_0 for H_2; toward the outer Galaxy, the FIR luminosity decays exponetially with a scale length of $0.21 R_0$, compared with $0.34 R_0$ for H_2.

Chapter 2

The Warm Ionized Gas

2.1 Introduction

This chapter presents a detailed description of the warm ionized medium (WIM). In particular, in section 2.2 we will outline the scientific case for the WIM, underlying the intersectorial implications of its investigation. In section 2.3, an overview of the various observational techniques will be given, complemented by the WIM physical properties inferred from observations. Finally, in section 2.4, we will discuss how current theoretical models try to reconcile the scattered information provided by experiments.

2.2 Why studying the WIM ?

There are several reasons motivating the study of the warm ionized gas of our Galaxy. Here we summarize the main ones which we may group into two catergories: those which fall in the field of investigation of the Galactic structure and its constituents and those which are related to the Cosmic Microwave Background (CMB). We first discuss in detail why the WIM is important within the context of Galactic studies.

- The warm ionized gas is a major component of the interstellar medium of our Galaxy, extending from the midplane into the lower Galactic halo where it could be the dominant state of the interstellar gas. This has been shown (Dickey & Lockman [87]) by comparing the HI and H^+ column densities towards five globular clusters located at more then 3 kpc from the plane. The result retrieved by the comparison is that the amount of ionized gas ranges from 23% to 63% of the neutral hydrogen. The existence of this component appears then to have an important bearing upon the composition and topology of the interstellar medium and the principal processes of ionization and heating within the disk and the halo. Moreover, the diffuse ionized gas could contribute significantly to the total pressure at the midplane (Cox [73]) and have an important effect on the dynamics of the hot ($\sim 10^6$ K) gas above the plane (Heiles [156]). Furthermore, because the H^+ is a significant fraction of the interstellar matter, warm dust within it could be a non negligiable source of IR continuum (Reynolds [260]) and cosmic rays within it could produce a significant fraction of the diffuse γ-ray background, particularly at high Galactic latitudes (Bloemen [25]). The existence of the ionized gas clearly needs to be taken into consideration in models of the interstellar medeium and galactic halo and in the analysis of interstellar medium data.

- The distribution of Galactic free electrons provides estimates of the total number of ionizing photons emitted, hence on the number of massive, hot stars that produce them. In this way, it is possible to infer not only the star formation rate (SFR) but also the initial mass function (IMF) of massive stars. The total number of ionizing photons in a stellar population of age t, IMF $\phi(m)$ and SFR $\Psi(t)$ can be expressed by:

$$N_{Ly-c}(t) = \int_{m_{eff}}^{m_{up}} dm \int_0^{\tau(TAMS)} \Psi(t-\tau)\phi(m)N_{Ly-c}(m,\tau)d\tau \qquad (2.1)$$

(Valls-Gabaud [329]), where $N_{Ly-c}(m,\tau)$ is the number of Lyman continuum photons emitted by stars of mass m and time τ and the effective lifetime extends from the zero age main sequence (ZAMS) to the terminal age main sequence (TAMS). The effective cutoff mass m_{eff} is given by the IMF-weighted-Ly-c production rate and is $\sim$ 10 $M_\odot$. The reason for this is that the dependence of the number of emitted ionizing photons on temperature (mass) is extremely steep. As a consequence, eq. (2.1) gives an estimate of the IMF of stars above 10 $M_\odot$ but gives no information about the IMF below this limit. This fact has been taken into account by Schaerer & De Koter [272] who have built a model in which, adopting a Salpeter IMF, they make the assumption of continuity below 10 $M_\odot$. According to their model:

$$\left(\frac{N_{Ly-c}}{10^{56}\ s^{-1}}\right) = 3.1 \left(\frac{\Psi}{M_\odot yr^{-1}}\right)\left(\frac{0.1 - 1.5m_{up}^{-0.66} + 8.6m_{up}^{1.66}}{m_{low}^{-0.35} - m_{up}^{-0.35}}\right) \qquad (2.2)$$

being m_{low} the result of the continuity assumption. The above equation can be applied to derive, for instance, the SFR from $H\alpha$ measurements. In particular, under case B recombination conditions[1] (Valls-Gabaud [329]):

$$\frac{\Psi}{L(H\alpha)} = 2.2^{+2.5}_{-1.5}10^{-8}M_\odot yr^{-1}L_\odot^{-1} \qquad (2.3)$$

and this applies to a wide range of IMF slopes.

---

[1] The case A-case B distinction of recombination line theory will be discussed in section 2.3.1.

- A good knowledge of the distribution of free electrons in the Galaxy is also important to obtain information about the Galactic magnetic field. In fact, a linearly polarized electromagnetic wave propagating along the magnetic field of an ionized medium can be decomposed into two circularly polarized modes, i. e. a right-hand mode, whose **E** vector rotates about the magnetic field in the same sense as the free electrons do and a left-hand mode, whose **E** vector rotates in the opposite sense. As a result of the interaction between the **E** vector and the free electrons, the right-hand mode travels faster than the left-hand mode and, consequently, the plane of linear polarization experiences a rotation - known as *Faraday rotation* - as the wave propagates. The angle by which the polarization plane rotates is given by:

  $$\phi = \phi_0 + RM\lambda^2 \tag{2.4}$$

  where ϕ_0 is the initial polarization position angle of the radiation before it enters the plasma, λ is the wavelength and RM is the *Faraday rotation measure* defined as:

  $$RM = \mathcal{C} \int_0^D n_e B_{||} ds \tag{2.5}$$

  where the numerical constant $\mathcal{C}$ is 0.81 rad m^{-2} when n_e is expressed in cm^{-3}, the line-of-sight component of the magnetic field $B_{||}$ is in μG and the path length D is in pc (Gardner & Whiteoak [117]). Observationally, the rotation measure of a given source (pulsars or extragalactic radio continuum sources) can be determined by measuring the polarization position angle of the incoming radiation at two or more wavelengths.

  The sources of linearly polarized waves used to carry out Faraday-rotation measurements in our Galaxy are either pulsars or extragalactic radio continuum sources. Pulsars present a double advantage in this context: first, they lie within the Galaxy and their distance can be estimated; second, their rotation measure (eq. (2.5)) divided by their dispersion measure (see eq. (2.38)) yields the n_e-weighted average value of $B_{||}$ along the line of sight.

  Rand & Kulkarni [245] have analyzed 116 pulsars closer than 3 kpc from the Sun and have concluded that the local interstellar magnetic field has a uniform (or regular) component $\simeq 1.6$ μG and a random (irregular) component ~ 5 μG. By including more distant pulsars and making a more careful selection of the pulsar sample, Rand & Lyne [246] obtain, for the local uniform field strength, $\simeq 1.4$ μG. In addition, they find that the uniform field strength increases smoothly towards the Galactic center, reaching ~ 4.2 μG at $R = 4$ kpc which implies an exponential scale length ≤ 4.1 kpc. They also show that a concentric-ring model, in which the uniform magnetic field is purely azymuthal, results in field reversals at 0.4 kpc and at 3 kpc from the solar circle, with a maximum field strength between field reversals of 2.1 μG. Han & Qiao [141] have obtained the same value of $\simeq 1.4$ μG for the local uniform field strength but they also find that a bisymmetric magnetic field structure with a pitch angle of 8.2^0 and an amplitude of 1.8 μG gives a better fit to the pulsar data than the concentric-ring model. Han et al. [143] found evidence for at least one field reversal in the outer Galaxy and possibly a third reversal inside the solar circle. They claim that the observed field reversals, together with the measured pitch angle, support the hypothesis of a bisymmetric magnetic field. Yet, it can be shown that field reversals are also consistent with an axisymmetric magnetic configuration and this picture is supported by some observational (Vallee' [327]) and theoretical (Ferriere & Schmitt [103]) facts. More recently, Mitra et al. [225] find, for a set of 45 pulsars in the direction of the Perseus arm, a uniform magnetic field strength $\simeq 1.7$ μG and no evidence of field reversal up to a distance of 5-6 kpc.

Along the vertical direction, magnetic fields exist well beyong the *pulsar zone*. This is proved by the fact that the rotation measures of extragalactic sources have the same sign and are systematically larger, in absolute value, than the rotation measures of pulsars in nearby direction (Simard-Normandin & Kronberg [291]). An estimate of the scale height of the uniform field can be obtained from the observed rotation measures of high-latitude extragalactic objects combined with a model of the free electron density distribution. From a sample of more than 600 extragalactic sources, Inoue & Tabara [169] find a magnetic scale height ~ 1.4 kpc. This value is about one order of magnitude greater than the scale height deduced from pulsar rotation measures (Thomson & Nelson [319]; Han & Qiao [140]). This descrepancy could be explained by a structure with two magnetic field layers having very different scale height (Han & Qiao [141]).

Finally, as far as the magnectic field parity with respect to the Galactic midplane, there is not a clear picture yet. The RM vertical distribution for a combined set of extragalactic sources and pulsars at Galactic latitude $|b| > 8^0$ appears to be antisymmetric about the midplane in the first and fourth quadrants and roughly symmetric in the second and third quadrants (Oren & Wolfe [233]; Han et al. [142]). At the same time, rotation measures of low-latitude pulsars point to a symmetric distribution at all longitudes (Rand & Lyne [246]).

Despite its relevance, it is important to emphasize two caveats of this technique: rotation measures provide the line-of sight component of the Galactic magnetic field not its total strength; rotation measures only probe the warm ionized medium which occupies only a small fraction of the interstellar volume so the inferred magnetic field strengths are not necessarily representative of the ISM in general.

In section 2.3.5 we will come back on the Faraday rotation measure as one of the tools for investigating the structure (or better, the *substructures*) of the free electron density distribution.

- An accurate reconstruction of the free electrons distribution is important for deriving estimates of pulsar distance. This topic is discussed extensively in section 2.3.3.

- From the studies of the WIM in our Galaxy and in nearby galaxies, it appears likely that a substantial fraction of ionizing photons could escape from galaxies, due to the patchy, clumpy nature of the ISM, fractal (Elmergreen [100]) or otherwise. Domgörgen & Mathis [91] predicts that 19% percent of the ionizing radiation escapes O stars and, of this, between 2 and 4% leakes out of the Galaxy while the rest is absorbed by the diffuse interstellar gas. The detection of diffuse Hα in the Magellanic Stream (Weiner & Williams [338] implies that a large fraction of galactic ionizing photons reach that distance (Bland-Hawthorn & Maloney 1997 [21]). If many ionizing photons escape the galaxies, they contribute significantly to the ultraviolet background radiation (UVB) which is usually thought to be dominated by quasars. Consequently, galaxies may dominate the background, at least, locally. Recently, Ciardi, Bianchi & Ferrara [58] have investigated this contribution. In particular, they have studied the effects of gas density inhomogeneities on the escape of ionizing Lyman contininuum photons from Milky Way type galaxies through 3D simulations. At this purpose, they consider a comparison between a smooth Gaussian distribution and a fractal one. They find an escape fraction as high as nearly 60% in the case of a smooth, Gaussian distribution and an ionization rate $\sim 9\times 10^{50}$ s^{-1}, corresponding to a SFR of roughly 2 M$_\odot$ yr^{-1}. Therefore, if high-redshift galaxies have gas column densities similar to local ones and are characterized by such high SFRs and by a predominantly smooth interstellar medium, this result may indicate that they should considerably contribute to - and possibly dominate - the cosmic UVB.

We are now going to discuss why studies of the warm ionized gas are also relevant for the Cosmic Microwave Background and what, in particular, is the relation between these two fields of Astrophysics.

The WIM - CMB relation: Cosmology has now entered the era of precision Cosmic Microwave Background (CMB) measurements. Since the original detection of temperature perturbations on large angular scales (7^0) by the COBE satellite (Smoot et al. [297]), there have been plenty of new detections spanning roughly two orders of magnitude in angular scale – 10^0 - 10 arcmin – (de Bernardis et al. [81]; Hanany et al. [144]; Mason et al. [211]; Leitch et al. [196]; Scott et al. [279]; Bennett et al. [16]). The extraction of cosmological information requires careful control and understanding of all possible sources of signal contamination. Achieving a high precision of cosmological parameters requires a correspondingly accurate understanding of all *foregrounds*. In the context of CMB, the word *foregrounds* denotes the radio emission overlapping the cosmological one and which, consequently, contaminates the signal. In particular, the Galaxy, through synchrotron, dust and free-free emission contribute significantly to the overall foreground radiation. These three contaminating emissions define a *valley* in the brightness-frequency plane centered around 70 GHz (see Fig. 2.1) which is the region of smallest Galactic contamination. Although, clearly, CMB efforts are concentrated in this *valley*, Galactic signals must nonetheless be carefully removed to extract the purely cosmological fluctuations and to achieve the desired precision on cosmological parameters.

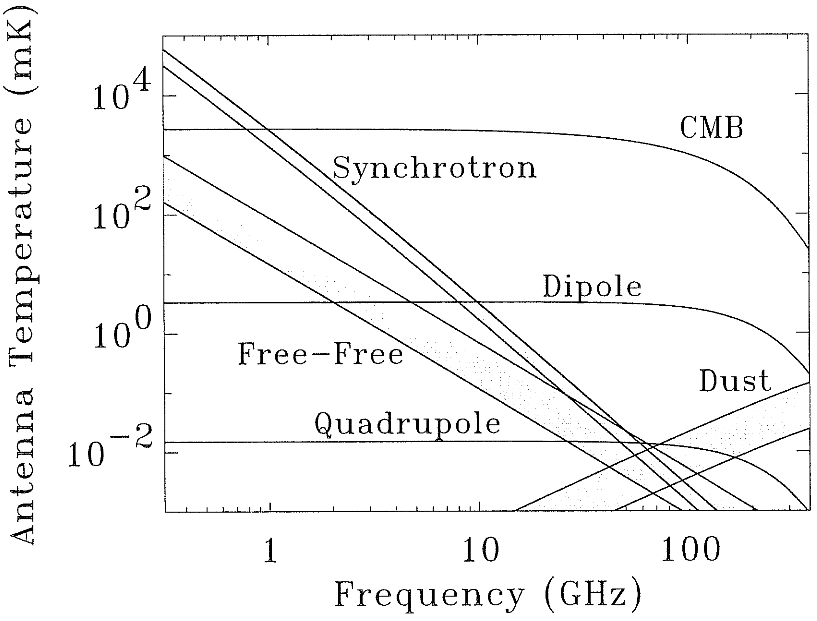

Figure 2.1: Frequency dependence and approximate relative strength of Galactic synchrotron, free-free and dust emission compared to CMB and CMB anisotropies.

The removal of these foregrounds is usually done in two ways:

1. with sufficient frequency coverage and a high signal-to-noise ratio, a spectral analysis of the CMB data alone can in principle distinguish the Galactic foregrounds from the CMB signal taking advantage of the different frequency dependence of each foreground component;
2. on the other side, it is possible to use maps obtained at frequencies other than the observing one, as templates and to extrapolate a given foreground emission into CMB bands according to its spectral dependence.

Usually, even when the quality of the CMB data allows the application of the former technique, the second approach provides an important, external check on the removal procedure. For synchrotron emission, since it dominates at frequencies below 1 GHz, templates have been obtained from low-frequency surveys (Haslam et al. [150]; Reich & Reich [250]; Jonas et al. [174]). The case of dust which is dominant at frequencies $>$ 100 GHz is similar: useful templates are the IRAS survey complemented by DIRBE maps (Finkbeiner et al. [108]). Free-free emission is instead more difficult to trace since (section 2.3.2) the only frequency range in which it may dominate over synchrotron and dust is in the CMB *valley*: in other words, one cannot extrapolate maps made at much lower or higher frequencies to the CMB bands in order to remove its contamination. Consequently, the common procedure consists in making use of a tracer of the WIM responsible for free-free emission. Given that at high Galactic latitudes there is minimal extinction from dust, one expects the Hα line to be a good tracer. We will see (eq. (2.28)) that a useful approximation for the free-free optical depth is that given by Altenhoff et al. [2]. For low frequencies ($\leq$ 1 GHz) the error in this expression is of the order a few percent but increases to 5-20 percent for frequencies above 10 GHz. An accurate formalism is that derived by Oster [234]:

$$\begin{aligned} \tau_\nu(Oster) &= 3.014 \times 10^{-2} T_e^{-1.5} \nu_{GHz}^{-2.0} (EM)_{cm^{-6}} \times \\ & \{ln[4.955 \times 10^{-2} \nu^{-1}] + 1.5 ln(T_e)\} \end{aligned} \tag{2.6}$$

Mezger & Henderson [220] define a factor $a(T, \nu)$, the ratio between the two formulae as:

$$\begin{aligned} a &= \frac{\tau_{nu}(Oster)}{\tau_\nu(Altenhoff)} = 0.366 \nu_{GHz}^{0.1} T_e^{-0.15} \times \\ & \{ln[4.995 \times 10^{-2} \nu_{GHz}^{-1}] + 1.5 ln(T_e)\} \end{aligned} \tag{2.7}$$

Accurate values of a for a range of temperatures and frequencies are given by Dickinson et al. [88]. With this expression, we can then rewrite eq. (2.30) as:

$$T_b^{ff} = 0.08235 a T_e^{-0.35} \nu_{GHz}^{-2.1} (EM)_{cm^{-6}\ pc} \left(1 + 0.08 \frac{\chi_{HeII}}{\chi_{He}} \frac{n_{He}}{0.08}\right) \tag{2.8}$$

where the factor in parenthesis accounts for the contribution from the fraction of He atoms, assumed to be singly ionized,n_{He} is the abundance of He by numbe, and a is given by eq. (2.7). By combining eq. (2.8) with eq. (2.14) (see section 2.3.1) which gives the Hα intensity under case B recombination conditions, we have (Dickinson et al. [88]):

$$\frac{T_b^{ff}}{I(H\alpha)} = 8.396 \times 10^3 a \nu_{GHz}^{-2.1} T_e^{0.667} 10^{0.029/T_e} \left(1 + 0.08 \frac{\chi_{HeII}}{\chi_{He}} \frac{n_{He}}{0.08}\right) \tag{2.9}$$

where T is in units of 10^4 K. Table 2.1 gives some values of the conversion factor obtained by applying this relation.

Table 2.1: Conversion factors for some relevant frequencies. T_e = 7000 K is assumed. Brightness temperatures are intended for I = 1 R where 1 R (Rayleigh) = $10^6/4\pi$ photons s^{-1} cm^{-2} sr^{-1} = 2.41$\times$ 10^{-7} erg cm^{-2} s^{-1} sr^{-1} = 2.25 cm^{-6} pc for T_e = 8000 K. Table values are from Dickinson et al. [88].

ν (GHz)	T_b^{ff}
0.408	51.2 mK
1.420	3.76 mK
2.326	1.33 mK
10	60.9 μK
30	5.83 μK
44	2.46 μK
70	0.94 μK
100	0.43 μK

However, there are a few caveats about eq. (2.9):

1. although the effect of extinction at high latitude is mitigated, yet it has to be considered;
2. uncertainty in the conversion from Hα intensity are introduced by the adopted value of electron temperature: T_e is, in fact, known to vary with Galactocentric radii[2] and, also, there are indications that it may be a function of $|z|$[3];
3. although all the calculations are done under the case B recombination assumption, in principle, case A[4] may also apply in the lower density regions: this adds some extra error in estimating the free-free brightness temperature from the observed Hα intensity.

Recently, two templates of the Galactic free-free emission have been made available by Dickinson et al. [88] and by Finkbeiner [109]. The Dickinson et al. map has been built combining the WHAM and SHASSA data [5]. It has an angular resolution of 1^0 and it has been corrected for dust using the 100 μm maps of Schlegel, Finkbeiner & Davis [274] (SFD98) and assuming that the Galactic absorption is 33% of the full extragalactic absorption. Particular care has been paid to the derivation of the relation between Hα intensity and free-free. The Finkbeiner map has instead an angular resolution of $6'$ and makes use of the WHAM, SHASSA and VTSS data [6]. The map is corrected for dust extinction again using the SFD98 model but assuming uniform mixing between dust and the ionized gas.

2.3 Observational properties

The warm ionized phase of the ISM gas can be probed in many ways. On one side, there are observational techniques which exploit the emission processes at work in the WIM

---

[2] We refer the reader to Chapter 4 for this discussion.

[3] See section 2.4.

[4] See discussion in section 2.3.1.

[5] For details about these surveys, see section 2.3.1.

[6] For details on the VTSS survey, see section 2.3.1.

at different wavelengths. Since $\sim$ 70% by mass of the ISM is H and we assume that He is basically neutral[7] at temperatures of the order of 10^4 K, then the warm ionized medium can be thought mainly as a mixture of free electrons and H positive ions. In this scenario, two fundamental emission mechanisms have to be considered: emission lines due to recombination processes (mostly Hα) and bremsstrahlung continuum emission produced by Coulomb interactions between the free electrons and the H ions. At the same time, we have observational methods based on the peculiar physical mechanisms produced by the presence of the WIM in our Galaxy. This is the case of pulsar dispersion (DM) and scattering (SM) measures.

In the following, we will consider each of these techniques and we will describe the properties of the ionized gas that, from their applications, can be inferred.

2.3.1 Hα emission

The emission mechanism

Two cases are usually distinguished in recombination line theory:

- Case A: recombination transitions occur in an optically thin medium, where emitted photons escape the region of emission without causing further transitions;
- Case B: recombination transitions occur in an optically thick medium so that emitted photons are reabsorbed and induce new transitions.

For typical HII regions, since $n_e \simeq 10^2 - 10^6$ cm^{-3} on scales of 1-10 pc, the optical thickness τ is $\sim 10^3$-10^{10} and case B applies. This appears to be adequate also for regions of ionized gas far from sites of star formation. In fact, with $n_e \sim$ 0.1-0.3 cm^{-3} on scale sizes of 10-100 pc, $\tau \sim$ 1-30 and the condition of optically thick regime is again satisfied. It is because case B applies to the physical conditions of the interstellar ionized gas that Hα traces the ionized gas in the Galactic ISM. In a steady-state, each photo-ionization of a H atom is associated with a H atom reaching its ground state by emission of a Lyman-series photon[8]. If the medium was not optically thick (case A), then Lyman-series photons would trace the ionized gas in the Galaxy. However, since the medium is on average dense (case B), it is very unluckily that emitted Lyman-series photons escape the emitting region: in fact, the ground state H atoms, being so abundant, offer a large cross-section for their absorption. Moreover, if the emitted photon is not a Lyα but a higher number of the series, then the excited H atom produced by its absorption has a finite chance of emitting two or more photons before returning to its ground state. In practise, each time a Lyman-series photon is absorbed, there is a non-negligible probability for the emission of a less energetic Lyman-series photon plus one or more photons of the Balmer, Paschen, etc..series. It follows that, after a sufficient number of

---

[7] We will come back on this point in section 2.3.1.

[8] For spectroscopic notation, the reader is referred to Fig. 2.2 .

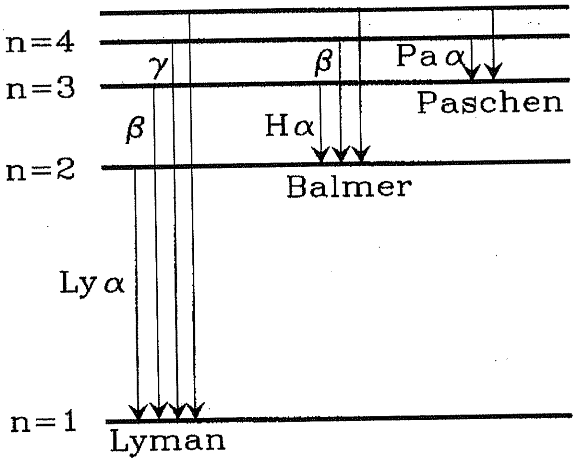

Figure 2.2: Schematic diamgram of the Lyman, Balmer and Paschen series of spectral lines in the spectrum of hydrogen (from Binney & Merrifield [20]).

absorptions, the energy of any Lyman-series photon will have been divided between a Lyα photon and some less energetic photons. Moreover, the creation of a Lyα photon is associated with the creation of a Balmer-series photon. Thus, the rate of creation of Balmer-series photons should equal the rate of ionization of H atoms, following the argument first introduced by Zanstra [353]. In particular, the Hα (6560 Å) is the most prominent among the Balmer-series lines. Also important are the Hβ (4860 Å) and the Hγ (4340 Å) lines.

An optically thin population of excited hydrogen atoms will radiate in the Hα spectral line a power (erg s^{-1} sr^{-1}):

$$j_\alpha = \frac{h\nu}{4\pi} A_{32} N_3 \tag{2.10}$$

where A$_{32}$ is the Einstein coefficient for spontaneous emission[9] and N$_3$ is the number density of hydrogen in the n = 3 excited level. Under the assumption of thermal equilibrium, by using Saha's equation[10] , we can relate the population density N$_3$ to the ion and electron densities, N$_i$ and N$_e$. If we take into account possible departures from thermal equilibrium, we can write the population density N_3 as:

---

[9] For case B recombination $A_{32}(H\alpha) = 1.29$ (Burbidge et al. [42]).

[10]

$$\frac{N_{j+1}N_e}{N_j} = \frac{2U_{j+1}}{g_j}\left(\frac{2\pi m_e kT}{h^2}\right)^{3/2} e^{-\chi_{j,j+1}/kT} \tag{2.11}$$

where N_{j+1} and N_j are, respectively, the ion population density of the $j+1$ and jth level, U_{j+1} is the partition function of the $j+1$ level, g_j is the statistical weight of the jth level and $\chi_{j,j+1}$ is the ionization potential between level j and $j+1$.

$$N_3 = b_3 \frac{g_3}{2U_0(T)} \left(\frac{h^2}{2\pi mkT_e}\right)^{3/2} e^{-\chi_3/kT_e} N_i N_e \tag{2.12}$$

being g_3 the statistical weight and χ_3 the ionization energy for n = 3, U_0 the partition function of atomic hydrogen and b_3 the departure coefficient reflecting the difference between the actual population of the level and the population that would occur in local thermodynamic equilibrium at the same temperature and for the same values of N_i and N_e (b_3=1 in thermodynamic equilibrium). In order to determine the departure coefficient b_3 ,it is possible to set up and solve a system of statistical balance equations[11] for the ionization equilibrium and bound level population densities. A useful expression for the Hα intensity, under case B approximation, derived by fitting the emission coefficients for Hβ computed by Brocklehurst [38] and Martin [209] following the lines now discussed and correcting for the Balmer decrement – Hα/Hβ – in the range of temperatures 5000 to 20000 K is:

$$I(H\alpha) = 9.41 \times 10^{-8} T_4^{-1.017} 10^{-0.029/T_4} \times EM \;\; erg\, cm^{-2}\, s^{-1}\, sr^{-1} \tag{2.14}$$

(Valls-Gabaud [329]) where the electron temperature, T_4, is expressed in units of 10^4 K and EM[12] is in cm^{-6} pc.

Observations

The first observations of Hα emission outside well-defined HII regions were reported in 1938 by Struve and Elvey [309]. Systematic studies in Hα only started thirty years later. An important photographic survey was carried out by Sivan [294] and Roesler et al. [267]. More recently, our knowledge of the WIM has been strongly improved by the successful realization, over the last five years, of high-resolution, high-sensitivity surveys. We summarize hereafter the most important of these surveys, given the sky-coverage and instrumental characteristics:

- WHAM: The Wisconsin H-Alpha Mapper Northern Sky Survey (Reynolds, Haffner & Madsen [264]) consists of 37.565 spectra obtained with a Fabry-Perot spectrometer placed on a 0.6m telescope at Kitt Peak, Arizona. The observations were made between January 1997 and September 1998. The angular resolution is 1^0 (comparable to the size of the field of view) and the sensitivity per pixel is $\sim$ 0.05 R;

---

[11] For statistical equilibrium, we can write a system of equations under the assumption that all the ways out of a level n are equated with all the ways into the level. The system of equation reads like:

$$N_n \sum_{n \neq m} P_{nm} = \sum_{n \neq m} N_m P_{mn} \tag{2.13}$$

where P_{ij} is the transition rate from i to j and N_i is the population of level i.

[12] The emission measure is defined as: EM = $\int N_i N_e ds \sim \int {n_e}^2 ds$ where the integral is taken over the line of sight.

- SHASSA: The Southern H-Alpha Sky Survey (Gaustad et al. [119]) consists of 542 fields, each 13.6^0 wide, obtained with a small camera at Cerro Tololo Inter-American Observatory (CTIO). The angular resolution of the survey is 0.8^0 and the sensitivity per pixel $\sim$ 2 R;
- The VTSS: The Virginia Tech Spectral line Survey (Dennison, Simonetti & Topsana [83] is a survey of the Northern emisphere carried out with the Spectral Line Imaging Camera (SLIC). 107 fields are currently available. Each field of view is 10^0 wide with an angular resolution of 1.6 arcmin and a sensitivity per pixel $\sim$ 1 R.

Derived physical properties

A number of properties are derived from observations of Hα:

1. the warm ionized gas is characterized by a complex morphology with filamentary structures (which appear to be long - $> 10^o$ - and narrow - $< 1^o$ -) and large, diffuse regions that occasionaly extend a kpc or more from the Galactic plane (Reynolds [253]);
2. this complex morphology displays a wide range of intensities: from thousands of Rayleighs near sites of star formation to $\sim$ 0.5 R in some of the fainter high latitude regions (Reynolds et al. [262];)
3. some filamentary structures appear to be associated with emission features at 21 cm and X-ray wavelengths; other filaments have no obvious correspondance to any previously known structures (Reynolds [262]);
4. most of the emission features are characterized by an electron density, $n_e \sim 0.2$ cm^{-3} (Reynolds [253]);
5. the overall Hα emission pattern, characterized by a decreasing intensity with increasing latitude, is consistent with a disk-like distribution and follows the empirical law:

$$< I(b) > \simeq 2.9 \times 10^{-7} cosc|b| \;\; erg\, cm^{-2}\, s^{-1}\, sr^{-1} \tag{2.15}$$

   at Galactic latitudes $|b| \simeq 15^o$ (Reynolds [253] [255] [303]);

6. by expressing the Hα intensity I as:

$$I(H\alpha) = \frac{1}{4\pi}\, e \times r\; cm^{-2}\, s^{-1}\, sr^{-1} \tag{2.16}$$

   where r is the hydrogen recombination rate per cm^2 along the line of sight and e is the average number of Hα photons produced per recombination (which ranges between 0.57 to 0.37 for temperatures between 1250 K and 80000 K (case B) respectively (Pangelly [237]), an estimate for r is derived and this is $\sim 4\times\ 10^6$ cm^{-2} s^{-1} (Reynolds [255]);

7. the diffuse warm ionized gas appears to contain a substantial fraction of the HII in the Galactic ISM as can be seen from a straightforward calculation: in a steady state, the total number N of HII ions is given by $N = r/\alpha n$ where r is the hydrogen ionization rate, α the effective hydrogen recombination coefficient and n the HII density within the ionized region. The ratio of the total amount of HII in the diffuse, ionized component to the amount in the brighter, discrete HII regions can then be estimated by evaluating the expression:

$$\frac{N_{diffuse}}{N_{discrete}} = \left(\frac{r_{diffuse}}{r_{discrete}}\right)\left(\frac{n_{discrete}}{n_{diffuse}}\right) \tag{2.17}$$

(Reynolds [258]). According to Abbott [1], the ionization rate within the diffuse component compared to that available from O stars suggests that $r_{diffuse}/r_{discrete} \simeq$ 12%. At the same time (see point 3)) the HII density within the diffuse regions of ionization is $\simeq 0.2$ cm^{-3} and the average densities associated with the discrete emission nebulae in the Galactic plane are greater than or ~ 1 cm^{-3}. Consequently, $N_{diffuse}/N_{discrete} \sim 0.6$;

8. by comparing [S$_{II}$] and [N$_{II}$] with Hα data, an [S$_{II}$]/Hα and [N$_{II}$]/Hα ratios increase with $|z|$ as absolute Hα intensities decrease has been found; this result, together with the fact that the [S$_{II}$]/[N$_{II}$] ratio remains constant over a large range of Hα intensities seems to suggest an increase in temperature of the WIM from 6000 to 10000 K, from bright to faint Hα emission regions, respectively (Haffner et al. [139]);

9. by assuming that the gas density is primarily a function of z and has the form:

$$n_e(z) = n_e^0 e^{-|z|/H}\ cm^{-3} \tag{2.18}$$

where n_e^0 is the midplane density and H is the scale height of the WIM, considering eq. (2.14) which relates the Hα intensity to the electron density and neglecting the z-dependence of electron temperature (as it would result from point 8)), the scale height H turns out to be $\sim 1.0\pm0.1$ kpc (Haffner et al. [139]).

Observational drawbacks

- **Ionization of Interstellar He:** The ionization state of helium in the WIM is most uncertain. Its first ionization potential is at 24.6 eV, quite above that of hydrogen (13.6 eV). According to observations of the He$_I$ λ5876 recombination line in two directions at low Galactic latitude, the He ionization fraction, $\chi_{He} = n_{He^+}/n_{He(total)}$, is found to be significantly less than unity: $\chi_{He} < 0.27$ (Reynolds & Tufte [261]). Radio recombination lines provide an even tighter constraint with $\chi_{He}/\chi H < 0.13$ (Heiles [157]). Consequently, ionized helium should not contribute more than a few percent to the derived physical parameters of the WIM.

- **Dust absorption:** At high Galactic latitude Hα is expected to be an excellent tracer of the warm ionized gas but at intermediate and low latitude, Galactic dust absorbs and scatters Hα photons therefore severly affecting the observations. Uncertainties in the correction for this effect are mainly introduced by the adopted dust model and by the assumed level of mixing of dust and ionized gas along the line of sight.

- **Geocoronal emission:** A source of contamination of Hα observations is the so-called *geocoronal* emission, i.e. the excitation of local interstellar hydrogen atoms by solar Lyβ photons. Maps of interstellar Hα are usually corrected for this effect by exploiting the spectral separation between the interstellar and the geocoronal lines which is due to the combination of the earth's orbital velocity, the sun's peculiar velocity and the intrinsic motion of the interstellar gas, including differential rotation.

2.3.2 Free-free emission

The emission mechanism

Free-free emission (thermal bremsstrahlung) is produced when fast charged particles (like electrons) are accelerated as a consequence of the encounter with an ion of charge Ze. This radiative mechanism is denoted *free-free* due to the fact that the electron is in a free (unbound) state both before and after the Coulomb scattering and the corresponding emission. This is opposed to the cases in which, for instance, the electron is captured into a bound state (free-bound emission) or makes a transition from one bound level to another (bound-bound emission). In addition, electrons are characterized by a *thermal* (or Maxwellian) distribution of velocities, i. e. the probability dP that a particle has velocity **v** in the velocity range d^3v is:

$$dP \propto e^{-E/kT}\, d^3v \propto v^2 exp\left(-\frac{mv^2}{2kT}\right)\, dv \tag{2.19}$$

where we have assumed an isotropic velocity distribution so that $d^3v = 4\pi v^2 dv$. With this assumption, the free-free emissivity (the total emission per unit time per unit volume per unit frequency) is:

$$e_\nu{}^{ff} = \frac{dW}{dVdtd\nu} = \frac{2^5\pi e^6}{3mc^3}\left(\frac{2\pi}{3km}\right)^{1/2} T^{-1/2}Z^2N_eN_ie^{-h\nu/kT}\overline{g}_{ff} \tag{2.20}$$

Evaluating this expression in CGS units, we have $e_\nu{}^{ff}$ in erg s^{-1} cm^{-3} Hz^{-1}:

$$e_\nu{}^{ff} = \frac{dW}{dVdtd\nu} = 6.8 \times 10^{-38} Z^2 N_e N_i T^{-1/2} e^{-h\nu/kT} \overline{g}_{ff} \tag{2.21}$$

In this expression, $\overline{g}_{ff}$ is the velocity averaged Gaunt factor which accounts for the quantuum mechanical scattering effects. Approximate analytic formulas for $\overline{g}_{ff}$ in the various regimes (in which, for instance, large-angle scatterings or small-angle scatterings are dominant) have been derived (see Novikov & Thorne [229]). In the classical, small-angle scatterings approximation:

$$\overline{g}_{ff} = \frac{\sqrt{3}}{\pi} \ln \left[\frac{4}{\psi^{5/2}} \left(\frac{kT}{h\nu} \right) \left(\frac{kT}{Z^2 Ry} \right)^{1/2} \right] = 0.5513 \ln(T^{1.5}/Z\nu) + 9.75 \tag{2.22}$$

where ψ is the Euler's constant and the energy unit Ry=13.6 eV. If we now consider Kirchhoff's law:

$$j_\nu^{ff} = \alpha_\nu^{ff} B_\nu(T) \tag{2.23}$$

it is possible to relate the emissivity e_ν^{ff} obtained above (eq. (2.21)) with the absorption coefficient α_ν^{ff}. We remind that the relation between e_ν^{ff} and j_ν^{ff} is:

$$e_\nu^{ff} = \frac{dW}{dVdtd\nu} = 4\pi j_\nu^{ff} \tag{2.24}$$

Therefore, by making use of the Planck function [13], we obtain:

$$\alpha_\nu^{ff} = \frac{4e^6}{3mhc} \left(\frac{2\pi}{3km} \right)^{1/2} T^{-1/2} Z^2 N_e N_i \nu^{-3} (1 - e^{-h\nu/kT-1}) \overline{g}_{ff} \tag{2.25}$$

In the Rayleigh-Jeans approximation, $h\nu \ll kT$, this expression becomes:

$$\alpha_\nu^{ff} = \frac{4e^6}{3mhc} \left(\frac{2\pi}{3km} \right)^{1/2} T^{-3/2} Z^2 N_e N_i \nu^{-2} \overline{g}_{ff} \tag{2.26}$$

Evaluating eq. (2.26) in CGS units, we have α_ν^{ff} in cm^{-1}:

$$\alpha_\nu^{ff} = 0.018 T^{-3/2} Z^2 N_e N_i \nu^{-2} \overline{g}_{ff} \tag{2.27}$$

Integration along the line of sight gives the optical depth τ_ν:

$$\tau_\nu = 0.018 T^{-3/2} \nu^{-2} \int N_e N_i dl \, \overline{g}_{ff} = 0.018 T^{-3/2} \nu^{-2} EM \, \overline{g}_{ff} \tag{2.28}$$

---

[13] $B_\nu(\mathrm{T}) = \frac{2h\nu^3}{c^2} \frac{1}{exp(h\nu/kT-1)}$

Here Z=1, EM is the emission measured defined in section 2.3.1 and $\overline{g}_{ff}$ is from eq. (2.212). In CGS units, τ_ν^{ff} becomes:

$$\tau_\nu^{ff} = 0.0543T^{-3/2}\,\nu_{GHz}^{-2}\,(EM/cm^{-6}pc)\,\overline{g}_{ff} \simeq 0.08235T^{-1.35}\,\nu_{GHz}^{-2.1}\,(EM/cm^{-6}pc) \quad (2.29)$$

The last approximation, which incorporates the dependence on ν and T of the Gaunt factor in eq. (2.22) is from Altenhoff et al. [2].

An estimate of the brightness temperature for free-free emission can be found from the radiative transport equation:

$$T_b^{ff} = T_e(1 - e^{-\tau}) \quad (2.30)$$

In the optically thin regime, $\tau_\nu \ll 1$, $(1 - e^{-\tau}) \sim \tau$ so that:

$$T_b^{ff} \simeq T_e\,\tau \sim 0.08235\mu K\,T_4^{-0.35}\,\nu_{GHz}^{-2.1}\,(EM/cm^{-6}pc) \quad (2.31)$$

where T_4 is T_e expressed in units of 10^4 K.

In the optically thick regime, $\tau \gg 1$, $(1 - e^{-\tau}) \sim 1$ and we have:

$$T_b^{ff} \simeq T_e \quad (2.32)$$

Observations

The radio continuum emission of the WIM is not a dominant component at any frequency of observation and this fact has so far substantially limited the number of its known physical properties (such as its large scale structure). We will come back on this topic in section 2.4 in which the relation between the free-free emission from the warm ionized gas and the other types of Galactic emission at radio frequencies (such as non-thermal synchrotron emission and thermal dust emission) will be discussed extensively. In particular, this relation will be analyzed in the light of CMB experiments for which, as we will see, a correct evaluation of the contribution of Galactic free-free to the detected signal turns out to be necessary. In this context, it will be shown how free-free estimates can be derived from Hα measurements, being both processes dependent on the same physical quantity, i. e., the emission measure.

Before moving to the next section, it is important to emphasize that the reconstruction of the spatial distribution of the radio continuum emission produced by the WIM is relevant not only for CMB studies but also for investigating the ionized gas as such. In fact, other tracers suffer from undersampling (i.e. pulsar dispersion measure[14]) or selection effects(i.e. Hα[15]) while a comprehensive mapping of free-free emission would provide a direct, unbiased picture of the distribution of the ionized gas in our Galaxy.

---

[14] See section 2.3.3

[15] See section 2.3.1

2.3.3 Pulsar dispersion and scattering measures

- **Dispersion Measure (DM)**

  In the paper announcing the discovery of the first pulsar, Hewish et al. [161] interpreted the variation of pulse arrival time with frequency to be the result of dispersive propagation through the partially ionized interstellar medium. In particular, if we consider a radio signal emitted by a pulsar at frequency ν_1, this propagates through the interstellar medium with group velocity:

$$c_g = c\sqrt{1 - \frac{\nu_p^2}{\nu_1^2}} \tag{2.33}$$

where:

$$n(\nu_1) = \sqrt{1 - \frac{\nu_p^2}{\nu_1^2}} \tag{2.34}$$

is the *refractive index* of plasma being:

$$\nu_p = \sqrt{\frac{n_e e^e}{4\pi e_0 m_e}} \tag{2.35}$$

the *plasma frequency*. If we now assume that the pulsar is at a distance D, the time t for the pulse to arrive is:

$$t(\nu_1) = \int_0^D ds/c_g(\nu_1) = \frac{D}{c}\sqrt{1 - \frac{\nu_p^2}{\nu^2}} \simeq \frac{D}{c}\left(1 + \frac{e^2}{8\pi^2 e_0 m_e D \nu_1^2}\int_0^D n_e ds\right) \tag{2.36}$$

In the previous expression, $\nu \gg \nu_p$ and $DM = \int_0^D n_e ds$ is the *dispersion measure.* By considering another signal emitted by the pulsar at frequency ν_2, we can then write the difference between the time of arrival of the two pulses at frequency ν_1 and ν_2 as:

$$\Delta t = t_1 - t_2 = \frac{e^2}{8\pi^2 e_0 m_e D}\frac{DM}{(\nu_1^2 - \nu_2^2)} \tag{2.37}$$

By evaluating the difference Δt in ms, the frequencies in MHz and DM in m^{-3} pc, we have:

$$DM = 0.241\,\Delta t\,(\nu_1^{-2} - \nu_2^{-2}) \tag{2.38}$$

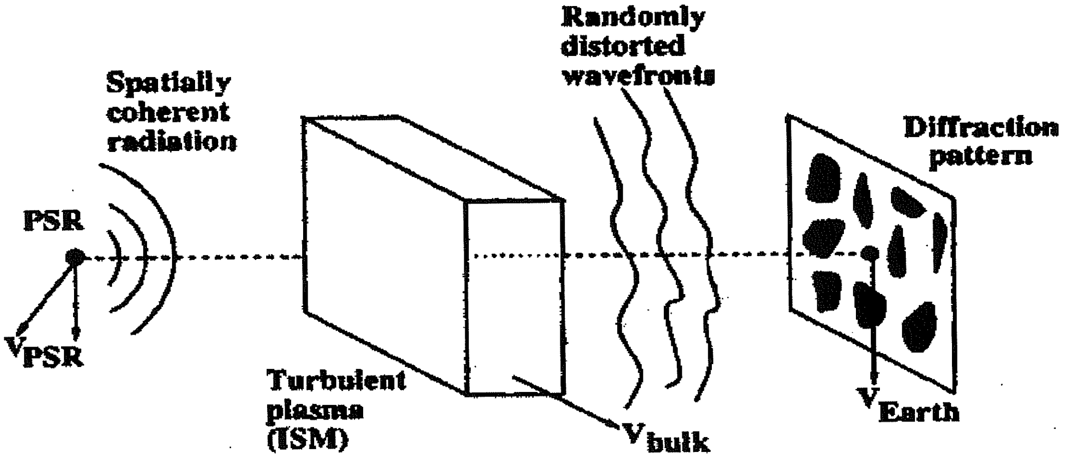

Figure 2.3: The geometry of scattering and scintillation. A pulsar emits radiation with high spatial coherence. Wavefronts are perturbed by electron density variations δn_e in the interstellar medium which cause refractive index fluctuations, δn (from Cordes [66]).

- **Scattering Measure (SM)**

  The physics of scattering phenomena is considerably more complicated. For a complete treatment we refer the reader to the review by Rickett [265]. The general idea is that the *scattering measure* gives an estimate of the small-scale fluctuations δn_e of the ISM electron density along the line of sight, i.e.: the turbulence which characterizes the Galactic ISM causes fluctuations in the electron density field; therefore when a highly spatially coherent wavefront (like the one emitted by pulsars) travels to the Earth, it is perturbed by the fluctuations in the refractive index fluctuations δn_r induced by the fluctuations in electron density (see Fig. 2.3). The scattering measure is defined as:

$$SM = \int_0^D C_n^2(s)\, ds \tag{2.39}$$

where C_n^2 is the spectral coefficient of the wavenumber spectrum for δn_e for which most of the data are consistent with a power-law of the form:

$$P_{\delta n_e}(k) = C_n^2 k^{-\alpha} \qquad \frac{2\pi}{l_0} \leq k \leq \frac{2\pi}{l_1} \tag{2.40}$$

In this expression, k is the wavenumber while l_0 and l_1 are, respectively, the outer and inner scales of the turbulence and the spectral index α is empirically determined to be 11/3±0.3 for many lines of sight (Lee & Jokipii [195]; Armstrong, Rickett & Spangler [6]), consistent with a Kolmogorov value of 11/3. It is common to quote SM in units of $kpc\, m^{-20/3}$.

The relevant observables for scattering measures are: the angular broadening of an image, θ_s, the temporal broadening of a pulse, τ_s and the characteristic bandwidth of diffractive scintillation, $\Delta\nu_s$. We describe briefly each of them:

1. **Angular broadening**: compact radio sources of many kinds, Galactic and extragalactic, show angular broadening by amounts ranging from < 1 mas to 1 arcsec at 1 GHz, depending on the distance and direction. The angular smearing scales approximately as ν^{-2}. Scattering theory yields the following expressions relating SM to θ_s (Taylor & Cordes [311]):

$$SM = \left(\frac{\theta_s}{128mas}\right)^{5/3} \nu_{GHz}^{11/3} \quad (extragalactic \quad sources) \tag{2.41}$$

$$SM = \left(\frac{\theta_s}{71mas}\right)^{5/3} \nu_{GHz}^{11/3} \quad (galactic \quad sources) \tag{2.42}$$

   where ν_{GHz} is the observing frequency in GHz.

2. **Pulse broadening**: Multipath propagation causes a multiplicity of arrival times, usually seen as an exponential-like tail to pulses from pulsars.Temporal broadening is related to SM by (Taylor & Cordes [311]):

$$SM = 292 \left(\frac{\tau_s}{D}\right)^{5/6} \nu_{GHz}^{11/3} \tag{2.43}$$

   where τ_s is in seconds and D is the distance in kpc.

3. **Diffractive intensity scintillation (DISS)**: Intensity variations in time and frequency on time scales ~ 100 sec and frequency scales ~ 1 MHz. These scales are very highly dependent on frequency, direction and source distance and velocity. The DISS is related to SM through (Cordes [66]):

$$SM = 0.23(\Delta\nu_s D)^{-5/6}\nu_{GHz}^{11/3} \tag{2.44}$$

   where the scintillation bandwidth $\Delta\nu_s$ is in kHz.

Eq. (2.40) through (2.43) hold in the strong scattering regime and will break down for nearby sources observed at high frequencies. Moreover, eq. (2.39) assumes isotropic density fluctuations, although evidence for anisotropies exist, at least for some directions (e.g Frail et al. [113]).

Observations

In the last two decades the observations of dispersion and scattering measures have undergone an unprecedented boost. In particular, the number of pulsars with an estimate of dispersion or scattering measures has nearly doubled as well as the amount of pulsar

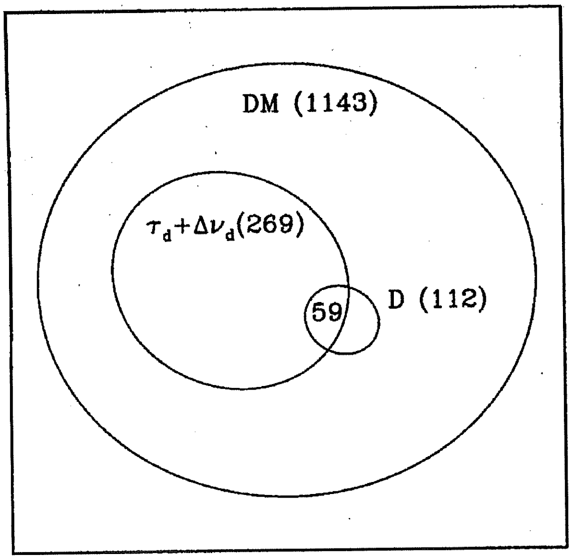

Figure 2.4: Venn diagram showing the number of DM measurements, independent distance measurements, (D), scattering measurements, (pulse broadening (τ_d) + scintillation bandwidth ($\Delta\nu_d$) measurements) and the overlap of pulsar distance and scattering measurements. In addition to pulsar data, there are 118 angular broadening measurements on non-pulsar Galactic sources and on 94 extragalactic sources (from Cordes & Lazio [67]).

with independent distance measurements (see Taylor, Manchester & Lyne [312]; Princeton Pulsar Catalog[16]; Parkes Multibeam Survey[17]). As we are going to see in detail in the forthcoming section, the combined information of dispersion or scattering measures plus and independent estimate of the pulsar distance allows us to map the 3D-distribution of the Galactic free electrons and, in turn, of the ionized gas. Distance estimates have been either derived by precise parallax measurements (Van Straten et al. [331]; Chatterjee et al. [54]; Brisken et al. [37]) or have been obtained from HI absorption measurements combined with a kinematic rotation model for the Galaxy. Alternatively, distances have been assigned through the association with a supernova remnants or a globular cluster. Noticeably, the reliability of these distance estimates have been substantially improved (Frail & Weisberg [111]; Ryba & Taylor [269]; Frail et al. [112]). Moreover, pulsars have been detected in a number of high-latitude globular clusters, well outside the Galactic disk and its layer of dispersing electrons and consequently the equivalent thickness of the dispersing layer is now known with more confidence (Reynolds [260]). The statistics have been improved especially in the inner Galaxy and in directions near and between the tangent points of the southern emisphere spiral arms where very little distance-related information had previously been available.

Observable scattering quantities give important information not otherwise available from dispersion measures only, especially on the innermost portions of the Galaxy, and provide a cross-check for regions where few, is any, independent pulsar distances have been obtained. However, these kind of measures are more difficult to determine than dispersion measures and have correspondingly lower precision. Most of the available scattering measures have accuracies of order 20%-50% (Taylor & Cordes [311]). Fig. 2.4 summarizes the pulsar dispersion and scattering measures currently available (Cordes & Lazio [67]).

Derived physical properties

Dispersion and scattering measures (complemented by emission measures) provide unique information on the 3D spatial distribution of the Galactic mean electron density and its fluctuations. Since free electrons are produced by ionization processes, their spatial reconstruction also tracks the location of the warm ionized gas in our Galaxy. Before describing models of the Galactic electron density distribution based on available observations of DM, SM and EM, we show, following Cordes & Lazio [67], the mutual relations existing among these physical quantities. For this purpose, we make the assumption that free electrons contributing to DM, SM and EM are the same and that the electron density at location s along the line of sight is represented by: $n_e(s) = \overline{n_e}(s) + \delta n_e(s)$. In addition, since along the line of sight there may be regions not fully ionized, we consider a filling factor η which accounts for this effect.

Taylor & Cordes [311] relate the SM to the square of the local, volume-averaged electron density by a dimensionless *fluctuation parameter* defined as:

---

[16] http://pulsar.princeton.edu/pulsar/catalog.shtml

[17] http://www.atnf.csiro.au/research/pulsar/pmsurv

$$F = \frac{\zeta \epsilon^2}{\eta} \left(\frac{l_0}{1pc} \right)^{-2/3} \tag{2.45}$$

where ζ is the clumping factor of large-scale electron density fluctuations, $\zeta = \langle \overline{n_e}^2 \rangle / \langle \overline{n_e} \rangle^2$, ϵ^2 the corresponding quantity for small-scale density variations, η the volume filling factor for ionized regions and l_0 the outer scale limit for an assumed Kolmogorov power-law of electron density turbulence. The value of F differs widely for the various Galactic components, increasing by nearly 100 times from the outer to the inner Galaxy. In terms of F, the differential contribution to SM from a particular electron density component reads:

$$dSM = C_{SM} F \langle n_e^2 \rangle_{los} ds \tag{2.46}$$

being C_{SM} a constant equal to $[3(2\pi)^{1/3}]^{-1} C_u$, where the scale factor $C_u = 10.2 m^{-20/3}$ yields the SM in the conventional units of $kpc\, m^{-20/3}$ for n_e in cm^{-3}, ds in kpc and l_0 in AU. If we now consider the differential contribution to DM from the same element of electron density:

$$dDM = \langle n_e \rangle_{los} ds \tag{2.47}$$

it follows that:

$$dSM/dDM = C_{SM} \langle n_e \rangle_{los} F \tag{2.48}$$

where $\langle n_e \rangle_{los}$ is the averaged-electron density along the line of sight. Finally, the differential contribution to EM is:

$$dEM = \langle n_e^2 \rangle_{los} ds \tag{2.49}$$

and this can be expressed in terms of dSM and dDM as:

$$dEM = \zeta \overline{n_e} dDM + C_{SM}^{-1} l_0^{2/3} dSM \tag{2.50}$$

With these relations at hand, we now detail two recent electron density distribution models: the Taylor & Cordes [311] model (hereafter TC93) and the Cordes & Lazio [67] model (hereafter NE2001).

- **TC93 model**

  Overview: The model worked out by Taylor & Cordes is a four-component model which includes: a thick disk, a thin disk, a four-arm spiral structure, the Gum Nebula. With respect to previous models (Manchester & Taylor [206]; Harding & Harding [146]; Vivekanand & Narayan [332]), the TC93 one is the first to depart from the assumption of an axisymmetric Galaxy and to incorporate explicitly the spiral arms[18]. The most striking evidence for a spiral arm structure come from the asymmetry resulting from the variation of pulsars DM with longitude (see Fig. 2.5): at low latitudes, the largest values of DM are in fact in the longitude range $-90^0 \leq l \leq 70^0$. Selection effects are unlikely to be the cause of the asymmetry as a number of deep searches at low latitudes near $l \sim 60^0$ have been carried out with the Arecibo Observatory, yet the number of pulsars around $l \sim -60^0$ is clearly much higher. In principle, contributions to the observed asymmetry of DM with respect to l may derive from regions near the solar system as well as from large-scale, spiral arm structure. However, a number of facts contradict the former possibility: individual regions such as the Gum Nebula have limited maximal contributions to the dispersion measures of pulsars seen behind them; the asymmetry extends over a range in longitude that is substantially larger than the Gum Nebula; the asymmetry shows the very narrow Galactic latitude confinement that one would expect for spiral arm structure while the Gum Nebula extends to at least 15^0 above and below the Galactic plane. At the same time, Fig. 2.5 also shows that the mean DM falls off monotonically with mean latitude b, almost independently of l at high latitude, therefore indicating the existence of a small scale-height (~ 0.15 kpc) disk-like distribution in the inner Galaxy. On the other side, the necessity of incorporating in the model a thick disk component comes from a diagram like the one of Fig. 2.6: here, the component of DM perpendicular to the Galactic plane, DM $\sin|b|$, is plotted against $|z|$ for pulsars with independent distant estimates.

The figure shows the extension of the dispersion layer up to $|z|$ exceeding 1 kpc. Finally, the model also explicitly incorporates the contribution of the Gum Nebula because of its large angular size (the angular diameter is $\sim 40^0$ with center at $l = 260^0$, $b = 0^0$) and close proximity (distance from the Sun ~ 0.5 kpc).

Functional form: The electron density at a specified Galactic location is the sum of contributions from each of the four components (*tkd*: thick disk, *tnd*: thin disk, *a*: spiral arms, *G*: Gum Nebula):

$$\begin{aligned} n_e(x,y,z) &= n_{tkd} g_{tkd}(r) sech^2(z/h_{tkd}) + n_{tnd} g_{tnd}(r) sech^2(z/h_{tnd}) + \quad (2.51) \\ &\quad + n_a sech^2(z/h_a) \sum_{j=1}^{4} f_j g_a(r, s_j) + n_G g_G(u) \end{aligned}$$

where:

$$\begin{aligned} g_{tkd}(r) &= sech^2(r/A_{tkd})/sech^2(8.5/A_{tkd}) \quad (2.52) \\ g_{tnd}(r) &= exp\{-[(r - A_{tnd})/1.8]^2\} \quad (2.53) \end{aligned}$$

---

[18] We will come back on the details of the TC93 model for the spiral arms in Chapter 4.

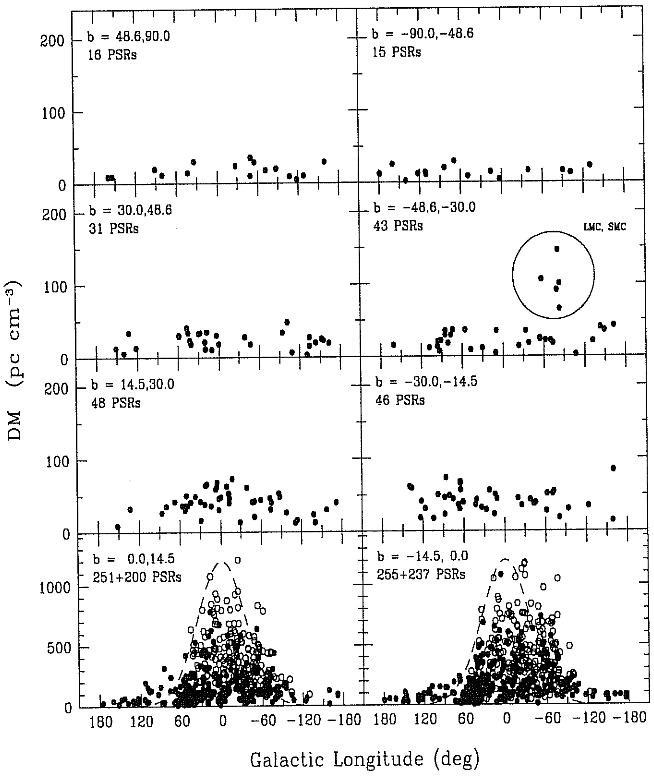

Figure 2.5: Scatter plots of DM vs. Galactic longitude for eight latitude ranges. Data represented with a filled circle are from the Princeton pulsar catalog while those represented with open circles are from the Parkes Multibeam survey. The circle in the right, second-from-top panel indicates pulsars whose DMs are contributed from LMC and SMC. The gaussian curve delineated by the dashed line in the two bottom panels helps to make the asymmetry more evident (from Cordes & Lazio [68]).

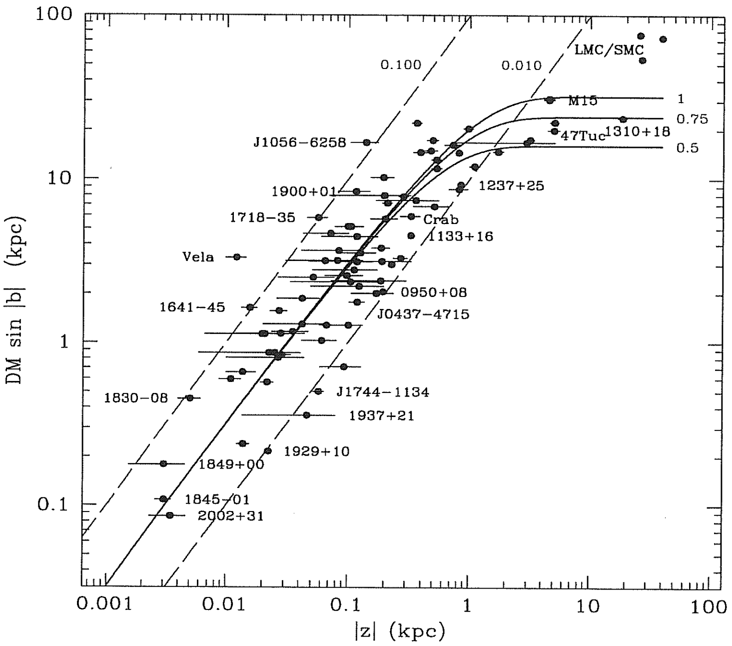

Figure 2.6: The component of DM perpendicular to the Galactic plane, DM sin$|b|$, is plotted against distance $|z|$ from the midplane for pulsars with independent distance constraints. The solid lines represent plane parallel models with exponential scale height of 0.5, 0.75 and 1 kpc (as labelled). For these models, the midplane density is held fized at 0.032 cm^{-3}. The dashed lines denote the electron density range: 0.01 - 0.1 cm^{-3} (from Cordes & Lazio [68]).

$$g_a(r, s_j) = \begin{cases} \exp[-(s_j/w_a)^2] sech^2[(r - A_a)/2.0] & : \; r > A_a \\ \exp[-(s_j/w_a)^2] & : \; r \leq A_a \end{cases} \tag{2.54}$$

$$g_G(u) = \begin{cases} \exp-[(u - 0.13)/0.05]^2 & : \; u > 0.13 \, kpc \\ 1.0 & : \; u \leq 0.13 \, kpc \end{cases} \tag{2.55}$$

In these expressions (eq. (2.51) through eq. (2.54)), $r = (x^2 + y^2)^{1/2}$ is the distance from the Galactic centre projected on the plane; z is the distance from the Galactic plane; n_x, h_x, A_x are, respectively, the constant density at the mid-plane, the scale height and the radial extent for each of the four components of the model (here x stands in turn for: *tkd*, thick disk; *tnd*, thin disk; *a*, spiral arms; *G*, Gum Nebula). Moreover, in eq. (2.52), the Galactocentric distance of the Sun is assumed to be 8.5 kpc; in eq. (2.53), the adopted scale length of the inner disk is 1.8 kpc; in eq. (2.54), $s_j = [(x - x_0)^2 + (y - y_0)^2]^{1/2}$ is the distance of a point (x, y,0) to the nearest point (x_0, y_0,0) of the j-spiral arm and the scale length of each arm is 2.0 kpc. In eq. (2.55), $u = [(x + 0.492)^2 + (y - 8.587)^2 + (z - 0)^2]^{1/2}$ is the distance of a point

(x,y,z) from the center of the Gum Nebula. Finally, the scale factors f_j implement a fine tuning for spiral arms: in general, aside from the radial cutoff for $r > A_a$, the arms are assumed to have constant densities along their axes. However, there are two exceptions: for the Carina-Sagittarius arm the density is doubled near the tangent point while for the Crux-Scutum arm it is reduced by $\sim$ 50%. This fine tuning accounts for the over-abundance of high-dispersion pulsars detected in that region of the Carina-Saggittarius arm and for the corresponding under-abundance in the Crux-Scutum arm.

Model parameters: Overall, the model comprises 13 parameters. These are, for each component, the electron density at the midplane, the scale lengths for the r and the z dependences plus a fluctuation term which accounts for the relation between the dispersion and the scattering contribution. For each of these parameters, the authors define a set of priors which are subsequently refined through a best-fit procedure. This procedure is based on a list of 74 pulsars with independent distance estimates. For each pulsar in the list, a model distance is computed by numerically integrating eq. (2.51) along the line of sight until the observed DM is reached. The parameters are then optimized by seeking the global minimum of an appropriate goodness-of-fit statistic which is defined to be:

$$\chi^2_{DM} = \sum_{i=1}^{74} \Delta_i^2 \tag{2.56}$$

where Δ_i is the residual difference for pulsar i expressed in logarithms:

$$\Delta = \begin{cases} log(d_l/d_m) & : \quad d_m < d_l \\ 0 & : \quad d_l < d_m < d_u \\ log(d_u/d_m) & : \quad d_m > d_u \end{cases} \tag{2.57}$$

d_m being the model distance and [d_l, d_u] the lower and upper limits to the allowed pulsar distance range. Additional constraints are obtained by defining, in a similar way, a second goodness-of-statistic, χ^2_{SM}, based on interstellar scattering data for 223 Galactic and extragalactic radio sources. The procedure yields estimates for the all 13 parameters as shown in Fig. 2.8.

Model discussion: The $r-$ amd $z-$ dipendences resulting from the model show that for $r \geq 12$ kpc or $z \geq 0.5$ kpc, the thick component always dominates. However, for locations at low z and close to a spiral arm or the inner annulus, the other components dominate. The uncertainty associated to distance estimates based on the model is of the order of 25%.

- **NE2001 model**

Overview: The NE2001 model (denoted in this way because it incorporates available data through the end of 2001) is built upon the TC93 model but largely supersedes it. A number of factors contribute to make the NE2001 model better suited to reconstruct the spatial distribution of free electrons. Among these:

1. a near doubling in the number of lines of sight with dispersion measure or scattering measurements[19];
2. a substantial increase in the number and quality of independent pulsar distance measurements;
3. improved information on scattering;
4. refinement of the definition of Galactic spiral arms[20];
5. better modeling of the local interstellar medium;
6. improved analysis for constraining the model parameters.

The model consists of five major components: a large scale distribution; the Galactic Center; the local ISM; individual clumps; individual voids. The large scale distribution, in turn, is the sum of two axisymmetric components, a thick and a thin disk, and of the spiral arms. The necessity of accounting for a large scale distribution has been already discussed in TC93. As for the other components a few comments are required. Scattering measurements indicate that a region of enhanced scattering is along the line of sight to the Galactic Center. To constrain the radial location of this region, scattering of extragalactic sources has been used. The local ISM (LISM) displays density enhacements and deficit which are associated with its particular star-formation history. As such, the LISM is not unique in the Galaxy. However, it needs to be explicitly modeled because the rest of the Galaxy is seen through it. In this attempt, a combined set of DM, SM, parallax and Hα observations (providing estimates of EM) has been exploited. In particular, four regions of low density have been considered: a local hot bubble (LHB) centered on the Sun's location; the Loop I (North Polar Spur) component; a local superbubble (LSB) in the third quadrant; a low density region (LDR) in the first quadrant. In addition, the contributions from Gum Nebula and from the Vela Supernova Remnants have been included. As well as local zones of enhanced densities, the model incorporates also the so-called *clumps*, i. e. regions of higher-than-ambient density which must exist spread throughout the Galaxy to explain the observed scattering in the direction of many Galactic and extragalactic sources.

At the same time, the model includes *ad hoc* regions of lower-than-ambient density, denoted *voids*, in order to account for some pulsar distance constraints.

Functional form: The functional form for the several components of the NE2001 model are shown in Fig. 2.7. For all the details about the functions, we refer the reader to Cordes & Lazio [67], [68].

---

[19] See Fig. 2.4 and compare with numbers given in discussion of the TC93 model.

[20] See Chapter 4.

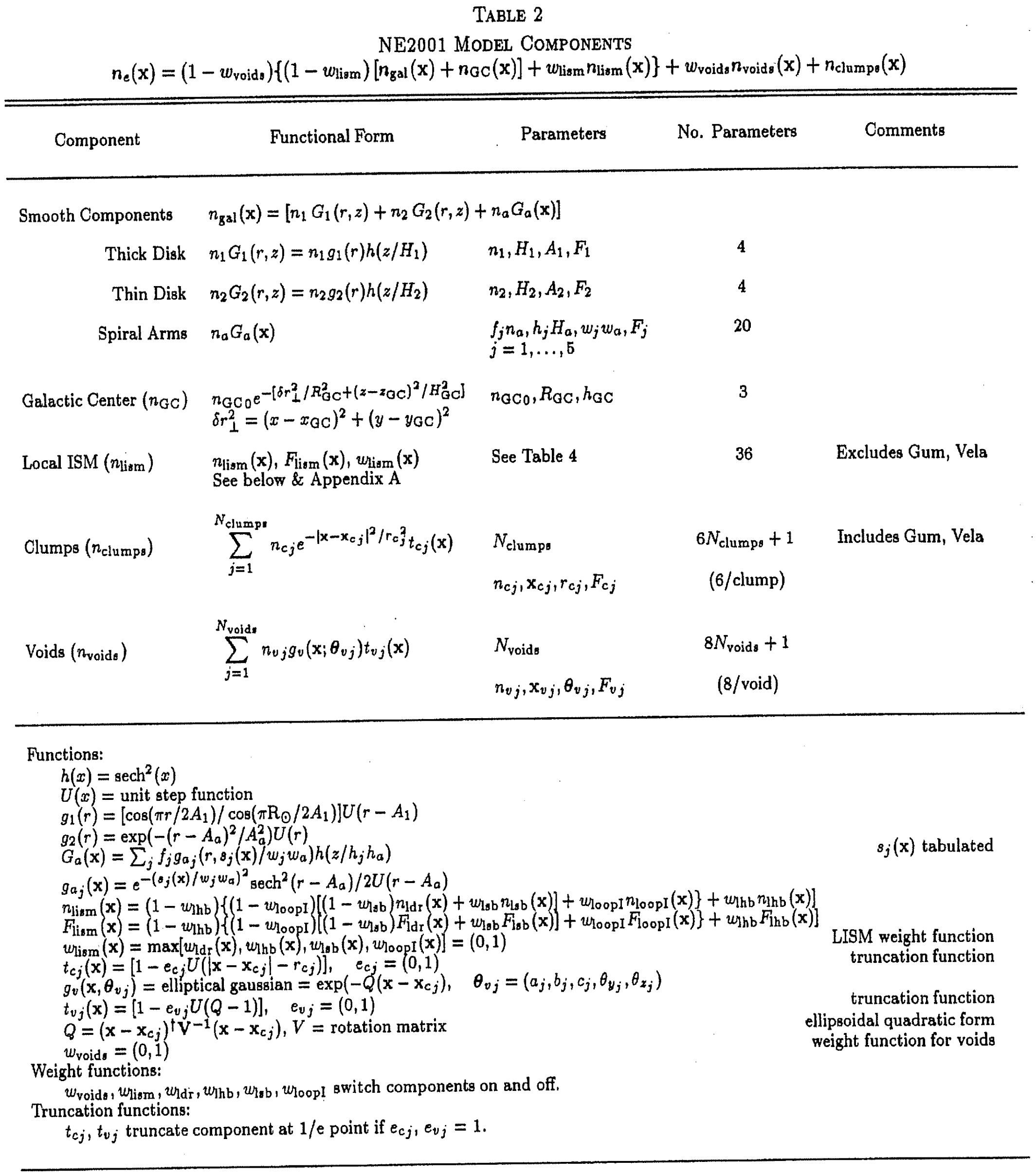

TABLE 2

NE2001 MODEL COMPONENTS

$$n_e(\mathbf{x}) = (1 - w_{\rm voids})\{(1 - w_{\rm lism})\,[n_{\rm gal}(\mathbf{x}) + n_{\rm GC}(\mathbf{x})] + w_{\rm lism}n_{\rm lism}(\mathbf{x})\} + w_{\rm voids}n_{\rm voids}(\mathbf{x}) + n_{\rm clumps}(\mathbf{x})$$

Component	Functional Form	Parameters	No. Parameters	Comments
Smooth Components	$n_{\rm gal}(\mathbf{x}) = [n_1\, G_1(r,z) + n_2\, G_2(r,z) + n_a G_a(\mathbf{x})]$			
Thick Disk	$n_1 G_1(r,z) = n_1 g_1(r) h(z/H_1)$	n_1, H_1, A_1, F_1	4	
Thin Disk	$n_2 G_2(r,z) = n_2 g_2(r) h(z/H_2)$	n_2, H_2, A_2, F_2	4	
Spiral Arms	$n_a G_a(\mathbf{x})$	$f_j n_a, h_j H_a, w_j w_a, F_j$ $j = 1, \ldots, 5$	20	
Galactic Center ($n_{\rm GC}$)	$n_{\rm GC0} e^{-[\delta r_\perp^2/R_{\rm GC}^2 + (z - z_{\rm GC})^2/H_{\rm GC}^2]}$ $\delta r_\perp^2 = (x - x_{\rm GC})^2 + (y - y_{\rm GC})^2$	$n_{\rm GC0}, R_{\rm GC}, h_{\rm GC}$	3	
Local ISM ($n_{\rm lism}$)	$n_{\rm lism}(\mathbf{x})$, $F_{\rm lism}(\mathbf{x})$, $w_{\rm lism}(\mathbf{x})$ See below & Appendix A	See Table 4	36	Excludes Gum, Vela
Clumps ($n_{\rm clumps}$)	$\sum_{j=1}^{N_{\rm clumps}} n_{cj} e^{-\lvert\mathbf{x}-\mathbf{x}_{cj}\rvert^2/r_{cj}^2} t_{cj}(\mathbf{x})$	$N_{\rm clumps}$ $n_{cj}, \mathbf{x}_{cj}, r_{cj}, F_{cj}$	$6N_{\rm clumps} + 1$ (6/clump)	Includes Gum, Vela
Voids ($n_{\rm voids}$)	$\sum_{j=1}^{N_{\rm voids}} n_{vj} g_v(\mathbf{x}; \theta_{vj}) t_{vj}(\mathbf{x})$	$N_{\rm voids}$ $n_{vj}, \mathbf{x}_{vj}, \theta_{vj}, F_{vj}$	$8N_{\rm voids} + 1$ (8/void)	

Functions:

$h(x) = \mathrm{sech}^2(x)$
$U(x) =$ unit step function
$g_1(r) = [\cos(\pi r/2A_1)/\cos(\pi \mathrm{R}_\odot/2A_1)]U(r - A_1)$
$g_2(r) = \exp(-(r - A_a)^2/A_a^2)U(r)$
$G_a(\mathbf{x}) = \sum_j f_j g_{a_j}(r, s_j(\mathbf{x})/w_j w_a) h(z/h_j h_a)$ — $s_j(\mathbf{x})$ tabulated
$g_{a_j}(\mathbf{x}) = e^{-(s_j(\mathbf{x})/w_j w_a)^2} \mathrm{sech}^2(r - A_a)/2U(r - A_a)$
$n_{\rm lism}(\mathbf{x}) = (1 - w_{\rm lhb})\{(1 - w_{\rm loopI})[(1 - w_{\rm lsb})n_{\rm ldr}(\mathbf{x}) + w_{\rm lsb}n_{\rm lsb}(\mathbf{x})] + w_{\rm loopI}n_{\rm loopI}(\mathbf{x})\} + w_{\rm lhb}n_{\rm lhb}(\mathbf{x})]$
$F_{\rm lism}(\mathbf{x}) = (1 - w_{\rm lhb})\{(1 - w_{\rm loopI})[(1 - w_{\rm lsb})F_{\rm ldr}(\mathbf{x}) + w_{\rm lsb}F_{\rm lsb}(\mathbf{x})] + w_{\rm loopI}F_{\rm loopI}(\mathbf{x})\} + w_{\rm lhb}F_{\rm lhb}(\mathbf{x})]$
$w_{\rm lism}(\mathbf{x}) = \max[w_{\rm ldr}(\mathbf{x}), w_{\rm lhb}(\mathbf{x}), w_{\rm lsb}(\mathbf{x}), w_{\rm loopI}(\mathbf{x})] = (0,1)$ — LISM weight function
$t_{cj}(\mathbf{x}) = [1 - e_{cj}U(\lvert\mathbf{x} - \mathbf{x}_{cj}\rvert - r_{cj})]$, $e_{cj} = (0,1)$ — truncation function
$g_v(\mathbf{x}, \theta_{vj}) =$ elliptical gaussian $= \exp(-Q(\mathbf{x} - \mathbf{x}_{cj})$, $\theta_{vj} = (a_j, b_j, c_j, \theta_{y_j}, \theta_{z_j})$
$t_{vj}(\mathbf{x}) = [1 - e_{vj}U(Q - 1)]$, $e_{vj} = (0,1)$ — truncation function
$Q = (\mathbf{x} - \mathbf{x}_{cj})^\dagger \mathrm{V}^{-1}(\mathbf{x} - \mathbf{x}_{cj})$, $V =$ rotation matrix — ellipsoidal quadratic form
$w_{\rm voids} = (0,1)$ — weight function for voids

Weight functions:

$w_{\rm voids}, w_{\rm lism}, w_{\rm ldr}, w_{\rm lhb}, w_{\rm lsb}, w_{\rm loopI}$ switch components on and off.

Truncation functions:

t_{cj}, t_{vj} truncate component at 1/e point if $e_{cj}, e_{vj} = 1$.

Figure 2.7: Mathematical form for each component of the Cordes & Lazio model (from Cordes & Lazio [67]).

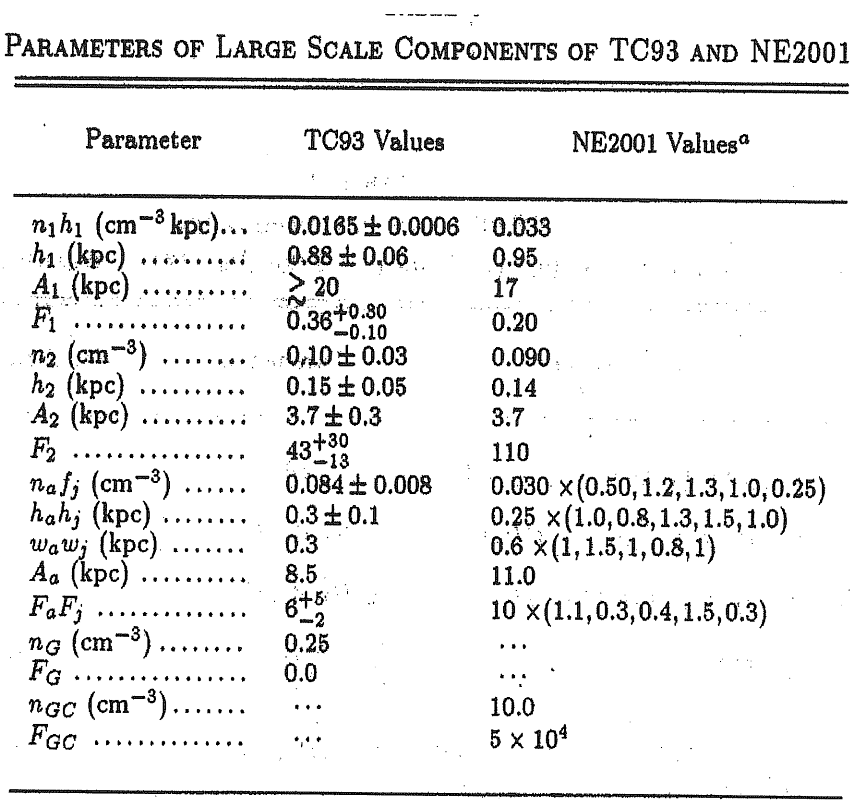

PARAMETERS OF LARGE SCALE COMPONENTS OF TC93 AND NE2001

Parameter	TC93 Values	NE2001 Values^a
$n_1 h_1$ (cm^{-3} kpc)...	0.0165 ± 0.0006	0.033
h_1 (kpc)	0.88 ± 0.06	0.95
A_1 (kpc)	$\gtrsim 20$	17
F_1	$0.36^{+0.30}_{-0.10}$	0.20
n_2 (cm^{-3})	0.10 ± 0.03	0.090
h_2 (kpc)	0.15 ± 0.05	0.14
A_2 (kpc)	3.7 ± 0.3	3.7
F_2	43^{+30}_{-13}	110
$n_a f_j$ (cm^{-3})	0.084 ± 0.008	$0.030 \times (0.50, 1.2, 1.3, 1.0, 0.25)$
$h_a h_j$ (kpc)	0.3 ± 0.1	$0.25 \times (1.0, 0.8, 1.3, 1.5, 1.0)$
$w_a w_j$ (kpc)	0.3	$0.6 \times (1, 1.5, 1, 0.8, 1)$
A_a (kpc)	8.5	11.0
$F_a F_j$	6^{+5}_{-2}	$10 \times (1.1, 0.3, 0.4, 1.5, 0.3)$
n_G (cm^{-3})	0.25	...
F_G	0.0	...
n_{GC} (cm^{-3}).......	...	10.0
F_{GC}	...	5×10^4

Figure 2.8: Comparison of the best-fit parameters for the large-scale component of the TC93 model with the values retrieved by NE2001 (the table is drawn from Cordes & Lazio [68]).

Model parameters: The parameters for the main components (the large-scale component and the Galactic Center) of the NE2001 model are the same as for the TC93 case, that is: the electron density at the midplane, the scale lenghts for the r and z dependences and a fluctuation term. The general fitting philosophy is to account for the dispersion and scattering of as many lines of sight as possible. This goal is achieved by the maximization of a likelihood function.

This is factorable according to the statistical independence of four kinds of measurements: pulsar with independent distance constraints; scattering measurements of pulsars; scattering measurements of other Galactic sources and scattering measurements of extragalactic sources. Therefore, the likelihood function can be written as:

$$\mathcal{L} = \mathcal{L}_d \mathcal{L}_s \tag{2.58}$$

where:

$$\mathcal{L}_s = \mathcal{L}_{psr,s} \mathcal{L}_{gal,s} \mathcal{L}_{xgal,s} \tag{2.59}$$

In eq. (2.58), $\mathcal{L}_d$ is assumed to be constant within the allowed range of values for the pulsar distance, $[d_l,\ d_u]$, while it has an exponential decay outside this interval. $\mathcal{L}_s$, instead, has a gaussian behaviour with respect to the scale length r_{scatt} which is a ratio of the model prediction with the observation for each of the scattering observable (i. e., the scattering broadening, the pulse broadening and the scintillation bandwidth). Having defined the likelihood function, priors for all the fitting parameters are set. These are subsequently constrained by maximization of the likelihood function. A comparison of the best-fit parameters obtained, for the large-scale component, by NE2001 and by TC93 is shown in Fig. 2.8.

Model discussion: The major conclusion resulting from the NE2001 analysis is that smooth, large-scale components are insufficient to produce a realistic description of the electron density distribution. The structure of the local ISM, as well as clumps and voids of electrons spread throughout the Galaxy have to be taken into account to produce reasonable agreement with observations. Distance estimates based on the model turn out to be uncertain by less than 20%.

2.3.4 Radio recombination lines

The emission mechanism

In an ionized gas, an electron and ion may pass close enough to each other that, with suitable release of energy, they become bound, with the electron in an energy level having a large principal quantum number. Most of these newly bound electrons immediately jump to the ground state. In a few cases the electron cascade downwards from level to level releasing their energy in a series of lines known as *recombination lines.* Since the paper of Kardashev [178] which predicted that the lines could be observed at radio wavelengths, a number of hydrogen transitions have been detected over a wide range of frequencies: from 36.5 GHz (n = 56 → n=55) to 404 MHz (n = 254 → n = 253). Many of these transitions have also been observed for helium. Line frequencies can be derived from the well-known Rydberg formula:

$$\nu = RcZ^2 \left[\frac{1}{n^2} - \frac{1}{(n+\Delta n)^2}\right] \tag{2.60}$$

where R is the Rydberg constant[21] for the hydrogen atom, c is the speed of light, Z the effective charge of the nucleus in units of the electron charge e, n the lower principal

---

[21] The Rydberg constant is a function of mass according to:

$$R = R_{\rm inf}\left(1 - \frac{m}{M}\right) \tag{2.61}$$

where $R_{\rm inf}$ is the constant for infinite mass, m the electronic mass and M the total mass, including electrons, of the atomic species involved.

quantum number and Δn the change in n. In the radio domain, where $\Delta n \ll n$, eq. (2.60) can be rewritten as:

$$\nu(n) \simeq 2RcZ^2\frac{\Delta n}{n^3} \tag{2.62}$$

and the approximate frequency separation between adjacent lines is:

$$\Delta\nu = \nu(n) - \nu(n+1) \ \simeq \ 6RcZ^2\frac{\Delta n}{n^4} \ \simeq \ \frac{3\nu}{n} \tag{2.63}$$

Shaver [285] has derived the expression for the highest quantum level, n_q beyond which no bound levels exist:

$$n_q \simeq \left[\frac{10^{20}T_e^{1.5}}{N_e} exp\left(\frac{26}{T_e^{1/3}}\right)\right]^{1/8.2} \tag{2.64}$$

Each transition is identified by its lower principal quantum number n and its change Δn. At a given frequency, the most intense transitions are those of the H$n\alpha$ type because of the great abundance of hydrogen.
To evaluate the intensity of the line, we proceed in a much similar way to the case of the Balmer Hα line. The emissivity per unit volume for the line $n' \to n$ is:

$$j_\nu^L = \frac{h\nu}{4\pi}A_{n'n}N_{n'} \tag{2.65}$$

where $A_{n'n}$ is the Einstein spontaneous emission coefficient and $N_{n'}$ is the number of atoms in level n'. In condition of thermal equilibrium, it is possible to determine the population density $N_{n'}$ through Saha's equation. Taking into account departures from this condition, the population density can be written as:

$$N_{n'} = b_{n'}\frac{g_{n'}}{2U_0}\left(\frac{h^2}{2\pi m_e kT}\right)^{3/2} \exp(-\chi_{n'}/kT)N_iN_e \tag{2.66}$$

where $b_{n'}$ is the departure coefficient[22] which can be determined through a set of statistical balance equations as in the case of Hα [23], $g_{n'}$ is the statistical weight of level n', U_0 the partition function and $\chi_{n'}$ the ionization energy for n'. From eq. (2.65) the absorption coefficient α_ν^L can be obtained by applying Kirchhoff's law and correcting for stimulated emission.[24] A useful expression for the absorption coefficient is given by Gordon [129]:

---

[22] For the definition of the departure coefficient, see section 2.3.1.

[23] See section 2.3.1.

[24] Stimulated emission is proportional to $e^{-h\nu/kT}$ so, since in the radio $h\nu \ll kT$, it follows that this effect is relevant at these frequencies.

$$\alpha_\nu^L = 1.070 \times 10^7 \Delta n \frac{f_{n'n}}{n} N_e N_i T_e^{-2.5} \exp(-\chi_{n'}/kT) m K(m) \tag{2.67}$$

where $f_{n'n}$ is the *oscillator strength* and, according to Menzel [219]:

$$f_{n'n} \simeq nM \left(1 + 1.5\frac{\Delta n}{n}\right) \tag{2.68}$$

with M = 0.190775, 0.26332, 0.0081056 and 0.0034918 for Δn = 1,2,3 and 4 respectively. The final step to derive the line intensity consists in writing the transfer equation. As we have seen in section 2.3.2, the free-free continuum is a dominant emission at radio frequencies and this contribution cannot be neglected when considering the intensity within the recombination line (compared to the optical case in which the continuum emission is instead negligiable). Consequently, such intensity will be the sum of that in the underlying continuum, I_c, and that from the line, I_L:

$$I = I_c + I_L \tag{2.69}$$

Under the assumption of thermal equilibrium, I is:

$$I = B_\nu(T)[1 - e^{-(\tau_c - \tau_L)}] \tag{2.70}$$

where τ_c and τ_L are, respectively, the continuum and line optical thicknesses, obtained by integrating along the line of sight eq. (2.26) and eq. (2.67). The intensity contributed by the line alone is then:

$$I_L = I - I_c = B_\nu(T_e) e^{-\tau_c(1-e^{-\tau_L})} \simeq B_\nu(T_e)\tau_L \qquad \tau_L, \tau_c < 1 \tag{2.71}$$

At the same time, in thermal equilibrium, $I_c \simeq B_\nu(T_e)\tau_c$ when $\tau_c < 1$. Consequently, the ratio of the total energy emitted in the line to that emitted in the underlying continuum is:

$$\int_{line} \frac{I_L}{I_c} d\nu = \int \frac{\tau_L}{\tau_c} d\nu \simeq \int \frac{\alpha_\nu^L}{\alpha_\nu^c} d\nu \tag{2.72}$$

A useful approximation to α_ν^{ff} (α_ν^c in this case) in eq. (2.26) is:

$$\alpha_\nu^{ff} \simeq \frac{0.08235 N_e N_i}{\nu^{2.1} T_e^{1.35}} \tag{2.73}$$

(Altenhoff et al. [2]) where ν is in GHz, N_e, N_i in units of cm^{-3} and α_ν^{ff} is in pc^{-1}. This approximation holds in the range of densities and temperatures typical of discrete HII regions and is accurate to 5%. By using eq. (2.73), eq. (2.72) becomes:

$$\int \frac{I_L}{I_c} d\nu = 1.299 \times 10^5 \Delta n \frac{f_{n'n}}{n} \nu^{2.1} T_e^{-1.15} F exp\left[\frac{1.579 \times 10^5}{n^2 T_e}\right] \tag{2.74}$$

The factor F accounts for the fraction of the free-free emission due to interactions of He^+ with electrons:

$$F = \left(1 - \frac{N_{He}}{N_H}\right) \tag{2.75}$$

where N_{He} and N_H are the relative number densities of helium and hydrogen ions, respectively. Observations of radio recombination lines in HII regions have established that N_{He}/N_H is ~ 0.08 so that F $\sim$ 0.92. In principle, eq. (2.74) is a very powerful tool: the electron density of optically thin ionized gas can be computed if the population of energy levels are in thermodynamic equilibrium and we ignore the effect of thermal and density gradients within the emitting medium. However, we will now see how, in the case of the diffuse ionized gas, eq. (2.74) cannot be easily applied.

Observations

The first observation of radio recombination lines in regions of the Galactic plane free of bright HII regions were made, almost simultaneously, by Gottesman & Gordon [133] and Jackson & Kerr [171]. However, the most important surveys so far carried out are those by Hart & Pedlar [148] and by Lockman [197] (cfr. Table 2.2). With respect to observations of discrete HII regions, surveys of the diffuse ionized gas are usually made at lower frequencies ($\sim$ 1.4-1.6 GHz) where the compact, high density sources are optically thick and hence do not contribute very much to the line emission. The major characteristics distinguishing the recombination lines emitted by the diffuse ionized gas from those of HII regions are the broad velocity extents and the weak intensities. Table 2.2 lists surveys of the diffuse component to date.

Table 2.2: Published hydrogen recombination line surveys of extensive regions of the Galactic plane.

Coverage	*Transition*	$\nu(MHz)$	*beam*	*Ref.*
$9.4^0 < l < 130^0$	$158 \rightarrow 157$	1683.2	$33'$	Gordon & Cato [134]
$358^0 < l < 50.5^0$	$167 \rightarrow 166$	1424.734	$21'$	Lockman [197]
$5^0 < l < 60^0$	$167 \rightarrow 166$	1424.734	$31' \times 33'$	Hart & Pedlar [148]

Clearly, there is a paucity of available data. This fact can be explained by considering the instrumental difficulty to date to detect such faint lines: for purpose of illustration, emission measures of 400 cm^{-6} pc can be detected in the H142α radio recombination line after an integration time of 20 hr (Gaylord [120]) while an emission sensitivity of 2 cm^{-6} pc for Hα can be reached with an integration time of 37 min (Reynolds [255]). Table 2.2 also shows that not only the entire range of longitude has not been fully explored (i. e. the third and fourth quadrants have not been observed at all) but all these surveys have been conducted at $b \simeq 0^0$ so that the recombination line emission of the ionized gas at low, intermediate and high latitudes is basically totally unknown. In addition, these surveys are characterized by very coarse sampling (tipically $\sim 1^0$ in l) due to the very long integration time required at each position.

Derived physical properties

Derivation of the diffuse ionized gas electron temperature from direct application of eq. (2.74) can be problematic. In fact, unlike HII regions, the continuum emission underlying these diffuse lines at the typical frequencies of observations ($\sim$ 1.4 GHz) is not only extremely weak but is a mixture of thermal (free-free) and nonthermal (synchrotron radiation) components in unknown proportions. A useful observable quantity, in terms of the brightness temperature T_L of the line excess over the continuum background, is then:

$$\int T_L dl = 1.070 \times 10^4 \Delta \frac{f_{nn'}}{n} \int N_e N_i b_n T_e^{-1.5} exp\left(\frac{1.579 \times 10^5}{n^2 T_e}\right) dl \qquad \tau_L, \tau_c < 1 \qquad (2.76)$$

where T_L is in K, ν is in kHz, the densities N_e and N_i are in cm^{-3} and the path length is in pc.

For most circumnstances in the ISM, the exponential term is close to unity for values of n appropriate for the centimeter wavelength range. Moreover, the path length l can be determined from the velocity information encoded in the line combined with a model of Galactic differential rotation. This topic will be discussed extensively in Chapter 4. For the time being it is important only to keep in mind that an element of ionized gas moving at radial velocity v_r will emit photons whose frequency is ν_0 in the rest frame of the gas, while, in the rest frame of the observer, this is given by the well-known *Doppler shift* relation:

$$\nu = \nu_0 \left(1 - \frac{v_r}{c}\right) \qquad (2.77)$$

With an estimate of the path length l, from eq. (2.76) it is then possible to derive the quantity $\langle N_i \cdot N_e \cdot b_n \cdot T_e^{-1.5} \rangle$ averaged over the path l. Unfortunately, the ionization factors (N_e, N_i) cannot be easily separated from the electron temperature. Nevertheless, studies of $\int T_L dl$ provide unique information about the spatial distribution of the ionized gas: at radio wavelengths, recombination lines are not affected by extinction (as in the case of Hα[25]) therefore allowing distant regions of the Galaxy to be probed. Fig. 2.9

---

[25] See section 2.3.1.

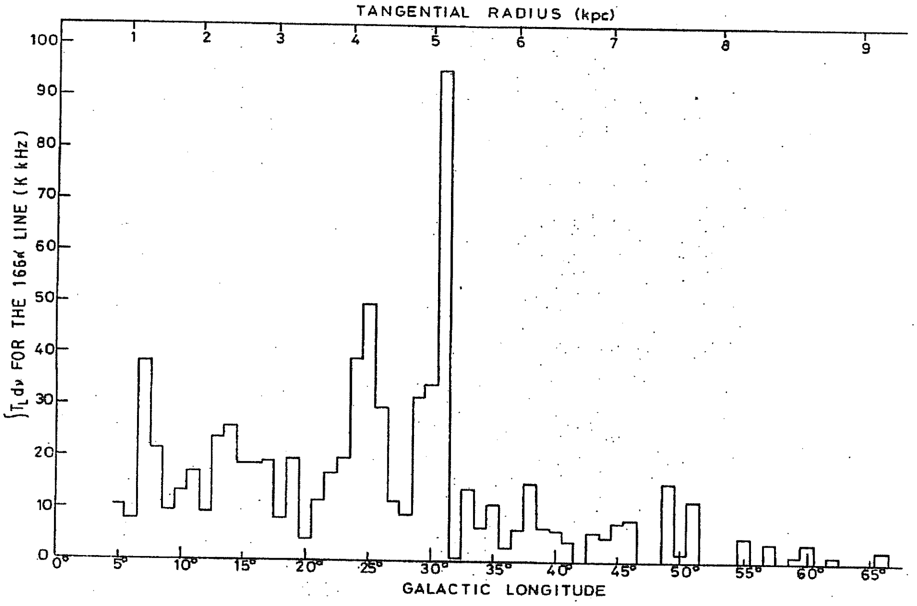

Figure 2.9: The intensity of the H166α line as a function of galactic longitude (from Hart & Pedlar [148]).

shows the longitude distribution of the H166α line intensity as it results from the Hart & Pedlar [148] survey. The most intense peaks ($l \simeq 25^0$ and $l \simeq 31^0$) in the line intensity may be associated with bright HII regions. Weaker recombination lines are also observed from directions which have low continuum-brightness at 5 GHz where HII regions are supposed to be clearly detected. The emission from these directions represent roughly 30% of the total emission. Beyond $l = 31^0$, the mean intensity of the weaker emission drops by about a factor 3 or more and has virtually disappeared by $l = 50^0$. These two longitudes correspond to directions tangential to the Scutum and Sagittarius arms respectively. Hart & Pedlar [148] report that, based on the longitude distribution they find, the bulk of the ionized hydrogen seems to be confined within 7 kpc of the Galactic centre and presents a deficiency within 4 kpc of the centre. Such conclusion is confirmed by Lockman [197] for the same frequency of observation (see Fig. 2.10). In addition, Lockman's analysis is characterized by the comparison between the radial distribution resulting from the H166α emission with that for the H109α line (Fig. 2.11). Clearly, the H109α distribution appears to be more extended in Galactocentric radius and significant power is detected over a wide range of R ($4 < R < 10$ kpc). This is due to the fact that, in general, high-frequency recombination spectra will be dominated by emission from the most dense components of a hetereogeneous medium while lower-frequency lines by less dense components (Brocklehurst & Seaton [39]). In particular, two effects ensure that the H166α spectra will largely reflect conditions in low-density gas:

1. the optical depth in the continuum for ionized gas is, at 1.4 GHz, greater than unity when the emission measure EM $\geq 25 T_e^{1.35}$ cm^{-6} pc (see eq. (2.28)) so that, if $T_e \sim 10^4$ K and we consider a path length of a few parsecs, this condition is met

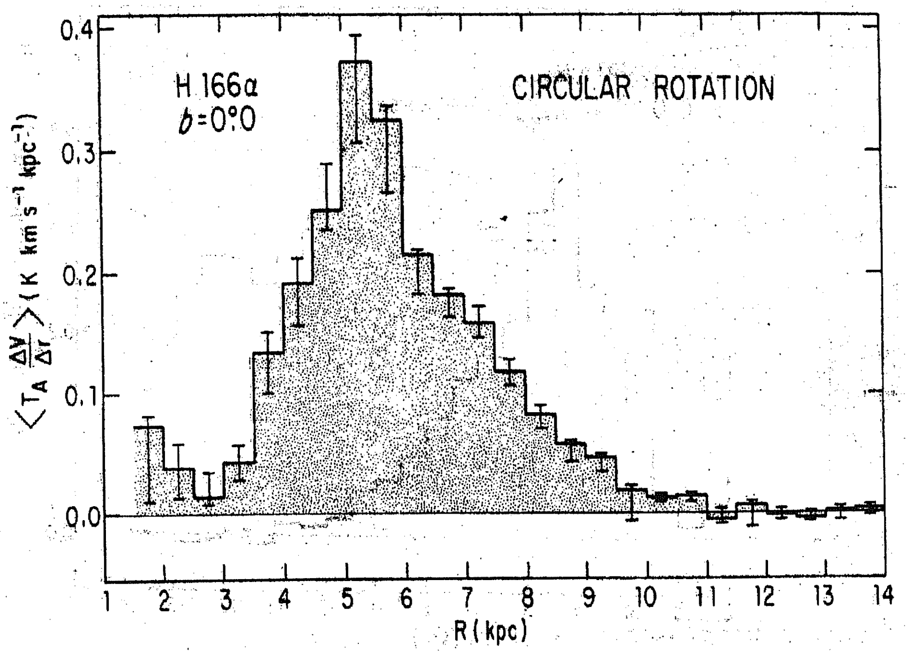

Figure 2.10: Average radial power in the H166α line as a function of galactocentric distance. In order to account for the projection of the galactic velocity field along the line of sight, the emission is weighted by the quantity $(\Delta V)/(\Delta r)$ where ΔV is the velocity channel width and Δr is the distance through the Galaxy which will contribute emission in the velocity range $V \pm \Delta V/2$ (from Lockman [197]).

when the electron density $N_e \geq 10^3$ cm^{-3};

2. impact broadening of the lines is significant in dense regions: at H166α this broadening significantly decreases the peak line temperatures when $N_e \geq 1500$ cm^{-3}.

On the contrary, none of these effects is important at high frequencies. This means in practise that the H109α line probes mainly bright, dense HII regions while with the H166α we trace the distribution of the more diffuse, low-density regions.

2.3.5 Faraday rotation measures

We have seen in section 2.2 how rotation measures, combined with a free electron density model, can probe the Galactic magnectic field. We now want to discuss how, in turn, rotation measures provide useful indications on the free electron distribution (and, ultimately, on the structure of the warm ionized gas) once assumptions on the uniform magnectic field strength are made. The information derived from rotation measures is particularly valuable when associated to analogous information obtained through scattering measures. Diffractive phenomena, such as angular broadening and pulse broadening (see section 2.3.3), provide measurements of the density irregularities on scales of 10^8-10^{10}

cm but are relatively insensitive to irregularities on much larger scales (e.g. $\sim 10^{12}$ cm or larger on which the outer scale of the interstellar turbulence could be probed). At the same time, there is a need to know the relationship between the density perturbations which produce scattering phenomena and the (presumably) associated magnetic field variation. These kind of indications can be retrieved by means of the so-called *structure function*, $D_{RM}(\Delta\theta)$. The structure function contains information on the statistics of the RM variations and it is determined by the nature of the plasma turbulence in the interstellar medium. The structure function is defined as:

$$D_{RM}(\Delta\theta) =< [RM(\theta) - RM(\theta + \Delta\theta)]^2 > \qquad (2.78)$$

where angle brackets indicate an expectation value. In writing this equation, it is assumed that the statistics of the RM fluctuations are stationary, i. e. not dependent on θ, and isotropic, or dependent only on the magnitude of $\Delta\theta$ and not on its orientation.

2.4 Modelling the Warm Ionized Gas

The achievement of a full comprehension of the origin and topology of the warm ionized gas is complicated by this being a typical *inversion problem*: i.e., although its boundary conditions (the distribution of free electrons, temperature, filling factor, etc..) are (sort of) known, it is still matter of debate what its initial conditions (the source of ionization) are.

We have seen (Chapter 1) that in the McKee & Ostriker [217] model of the ISM it is proposed that the warm ionized gas is located in transition regions between the cold HI clouds and the hot, very low density *coronal* gas, and that is photoionized by a very dilute Lyman continuum flux originating from luminous stars and supernova remnants. However, this picture appears to be incompatible with the fact that most of the H^+ is located well above the thin layer of young stars and HI clouds that define the traditional disk of the Galaxy. The presence of the H^+ at high $|z|$ and along lines of sight that are far from ionizing stars (Reynolds [260]), coupled with the existence of an opaque layer of HI that extends to high $|z|$ (Lockman [198]; Lockman, Hobbs & Shull [199]) seem to require either the existence of some as yet unidentified source of ionization at high $|z|$ or a special morphology of the HI that allows the ionizing photons originating near the Galactic plane to travel a kiloparsec or more up into the lower halo. In order to answer the first question, it is important to estimate the power input which is required to mantain the large-scale ionization which is observed. This kind of calculation has been made based on Hα measurements (see section 2.3.1) and confirmed by pulsar dispersion measurements (Reynolds [259]). The analysis yields and estimate for the hydrogen recombinatio rate $r \sim 4 \times 10^6$ cm^{-2} s^{-1} (Reynolds [255]) which, considering 13.6 eV per ionization, corresponds to a power consumption of 1×10^{-4} erg cm^{-2} s^{-1}, equal to 9.5×10^{38} erg kpc^{-2} s^{-1}. This value severely constrains the possible ionization source. Several candidates have been suggested: Wolf-Rayet stars (Panagia & Terzian [236]),

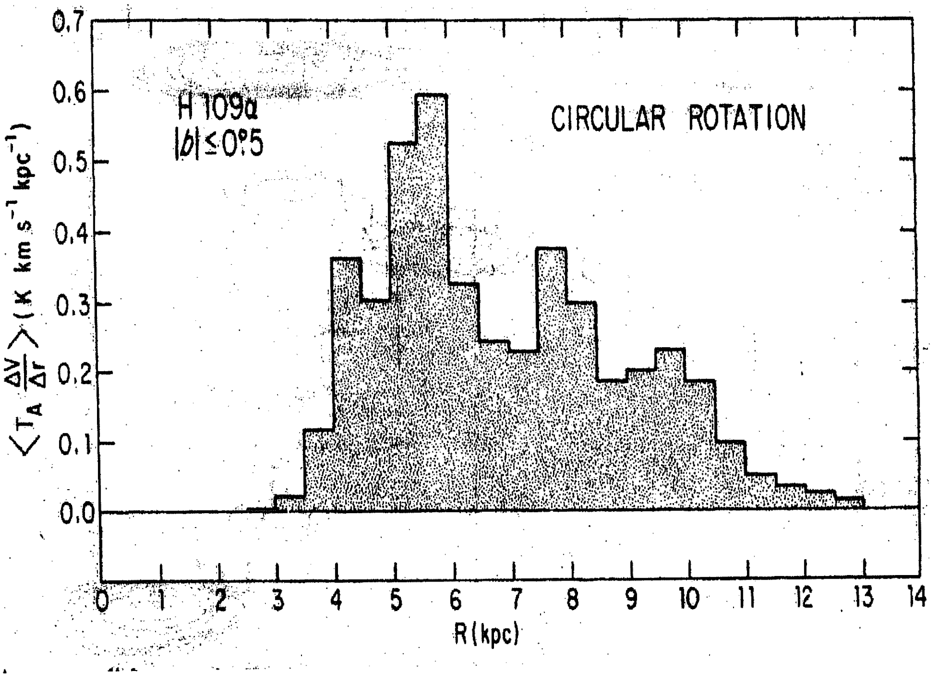

Figure 2.11: Average radial power in H109α line as a function of galactocentric distance. The meaning of the ordinate axis is the same as in Fig. 2.9 (from Lockman [197]).

cosmic rays (van Dishoeck & Black [330]), the diffuse X-ray background (McCammon et al. [214]), neutrino decay (Sciama [277][278]) as well as supernovae and OB stars. Apart for the *exotic* neutrino model, cosmic rays and X-rays fail to produce the required ionization rate by factors ranging from 20 to more than 100. On the other side, the case of Wolf-Rayet stars, supernovae and OB stars has been investigated in detail by Abbott [1]. He considers a complete sample of stars (B and A supergiants, O stars and Wolf-Rayet) within 3 kpc from the Sun and, based on this set of sources, studies which, among these spectral types, contribute more to the ionization of the interstellar gas. Now, there are three ways in which stars transfer energy to the interstellar medium: through their wind, their radiation field and, at their death, by supernovae. In terms of the total stellar output of energy, radiation is the dominant mode. In particular, O stars contribute 66% of the total radiative luminosity (about 2.2×10^{40} erg kpc^{-2} s^{-1}). However, all the three modes are of comparable importance for the transfer of stellar energy to the ISM: winds and supernovae are in fact much more efficient at transferring or dissipating energy to the interstellar gas. The energy conversion efficiency is roughly 10% for stellar radiation, 50% for stellar winds and 70% for SNs. Yet, each phase of the ISM has its own efficiency for converting the energy from radiation, winds and supernovae. From Abbott's analysis, it turns out that stellar radiation completely dominates the heating of the ionized gas while supernovae appear to be the major source of energy for the coronal gas and the kinetic energy of cloud motions. This result has been also confirmed by Cox [73] who has shown that, although supernovae (which provide 9.9×10^{38} erg kpc^{-2} s^{-1}) could in principle produce enough diffuse electrons to explain the pulsar dispersion measures, they fall short of providing the Galactic Hα brightness by a factor of 7. Therefore, Galactic OB stars appear to be the only viable candidates to photoionize the interstellar gas although two major problems arise:

1. the ionizing radiation must be able to reach the diffuse interstellar gas from the stars which tend to be near the plane; these stars are possibly surrounded by HI clouds that prevent any ionizing radiation from penetrating through them; from the solar system we detect HI in emission in all directions and also in absorption against all extragalactic sources with sufficient brightness;
2. the spectrum of the warm ionized gas is unlike ordinary HII regions: for instance, the normally very strong $[O_{III}]$ λ5007 is weak while low stages of ionization (N^+, S^+) are strong.

The photons penetration problem: despite several authours (Torres-Peimbert, Lazcano-Araujo & Peimbert [321]; Thuan [320], Lynds [203], Mathis [212], Bregman & Harrington [31]) have explored the possibility that O stars can ionize regions in the Galaxy far away from the plane, the first detailed study along this line has been made by Miller & Cox [223]. Miller & Cox constructed a model of the diffuse interstellar gas that accounts for enough penetration of the ionizing radiation to the diffuse gas. In their model, they consider a random distribution of neutral HI clouds[26] and a very smooth extracloud medium whose density depends only on z and they show that, despite the attenuation produced by these clouds against the ionizing flux generated by O stars, the Strömgren volume which are obtained are large enough to explain the ionization at high $|z|$. In addition, the Miller & Cox model seems to reproduce quite well the observed emission and the dispersion data even taking into account its oversamplified picture of the diffuse interstellar medium: in fact, various effects are not included such as the overlapping of nearby Strömgren spheres; stellar winds; superbubbles; density concentration along the spiral arms. Dust has been instead considered by assuming the clouds to be opaque. The Miller & Cox calculations have been subsequently revised by Elmergreen [100]. A large number of observations has shown that the ISM in the Galaxy and nearby galaxies has a hierarchical, very likely fractal structure (Elmergreen & Falgarone [99]). Theoretical works (see for example Norman & Ferrara [228]) also predict a fractal behaviour over a large dynamical range. The fractal structure arises from turbulent pressure which plays a crucial role in the various phases of the ISM (Kulkarni & Fich [190], Reynolds [256]) and is pumped into it primarily by multi-supernova explosions. Fractal clouds (which are not randomly distributed but are highly clumped and clustered) produce fractal ionization zones through which O-star radiation can travel at least twice as far as in a standard Strömgren sphere and contain extensive holes covering $\sim 50\%$ of the sky through which this radiation can reach the Galactic halo.

The spectral problem: The primary optical emission lines used to characterize the WIM are Hα λ6563, $[S_{II}]$ λ6716, $[N_{II}]$ λ6583, $[O_I]$ λ6300, $[O_{III}]$ λ5007 and HeI λ5876.

---

[26] Clouds parameters are those described by Spitzer [305].

Compared to classical HII regions, the warm ionized gas has high $[\mathrm{N}_{II}]/\mathrm{H}\alpha$ and $[\mathrm{S}_{II}]/\mathrm{H}\alpha$ and low $[\mathrm{O}_{III}]/\mathrm{H}\alpha$ (Reynolds [257], Osterbrock [235]). Domgörgen & Mathis [91] are able to match the observed spectrum through a low-density, low-excitation model which corresponds to a dilute stellar radiation leaking through the ISM. This view is also supported by models of the radiative transfer of ionizing photons through the Galaxy subject to the presence of interstellar clouds (Miller & Cox [223], Dove & Shull [92]; Bland-Hawthorn & Maloney [22]). However, with this pure photoionization models it is not possible to explain two phenomena: the rise in the $[\mathrm{O}_{III}]/\mathrm{H}\beta$ ratio with increasing distance from the plane and the constant $[\mathrm{S}_{II}]/[\mathrm{N}_{II}]$ line ratio (Haffner, Reynolds & Tufte Haffner et al. 1999). In order to circumvent the first problem, one can consider an additional ionization process (Martin [210], Collins & Rand [62]). Yet, this does not help to explain the second effect for which it has been suggested that it could be due to an increase of the electron temperature with $|z|$ (Haffner, Reynolds & Tufte [139]). Such a variation in temperature would seem to require the existence also of a non-ionizing heating mechanism such as dissipation of interstellar plasma turbulence or magnetic reconnection.

Chapter 3

A radio catalog of Galactic HII regions

3.1 Introduction

In the previous chapter we have discussed models (see Miller & Cox [223]; Elmergreen [100]; Domgörgen & Mathis [91]) of the Warm Ionized Medium which aim at understanding the source of the large-scale ionization observed in the Galaxy. We have also seen that such *theoretical models* are associated to another kind of models (see Taylor & Cordes [311]; Cordes & Lazio [67]) whose purpose is mainly the reconstruction of the Galactic free electron distribution which is useful not only to track the WIM spatial distribution but also to help suggesting the source of ionization of the diffuse ISM. We denote the latter class of models as *descriptive models* to distinguish them from the ones belonging to the first category. According to the descriptive models, it is necessary to consider, in addition to an axisymmetric component, a spiral arm component. One of the most reliable tracers of the latter are the large concentrations of free electrons, namely the HII regions. As a first step towards a comprehensive analysis of the properties of these sources and of their spatial distribution, we have compiled a large catalog containing all the relevant information we could find in the literature. Such catalog is presented in this chapter.

The chapter is organized as follows: section 3.2 provides a brief description of the pre-existing optical and radio catalogs of HII regions; section 3.3.1 presents the procedure adopted for the compilation of the Master Catalog and summarizes its content, while a full description is given in Appendix I. Section 3.3.2 describes the Synthetic Catalog at 2.7 GHz and discusses its completeness and the distribution of sources. The conclusions of the chapter are drawn in section 3.4.

3.2 Pre-existing catalogs of Galactic HII regions

The first major attempts to put together existing data have been made at optical wavelengths. This is mainly due to historical reasons since optical studies of HII regions started about half a century before the birth of radio-astronomy.
In the following two subsections we give a brief description of the main optical (by Sharpless [284] and Mársalková [208]) and radio (COBE-HII [348], [349] and Kuchar & Clark [188]) catalogs.

3.2.1 Optical catalogs

- **The Sharpless Catalog**
  The catalog contains 313 HII regions north of declination -27^0. It was obtained by combining early observations (see Sharpless[283]) in the longitude region 315^0 - 105^0, extending for several degrees on either side of the Galactic plane, with data from the National Geographic-Palomar Sky Atlas which have allowed the full coverage of the sky north of declination -27^0. The catalog provides valuable information on the early-type stars associated with the listed sources. It also reports, in addition to coordinates (Galactic – based on the Lund pole – and Equatorial for the year 1900), information on the shape (circular, elliptical or irregular), on the structure (amorphous or filamentary) and on the brightness.

- **The Mársalková Catalog**
  The catalog contains 698 sources and was produced combining 13 lists and small catalogs, notably those by Sharpless [284] for the northern sky, and by Rodgers et al. [266] and by Gum [138] for the southern sky. As the majority of listed sources lie within ±15^0 in Galactic latitude, the catalog has been divided into two sections, the first containing the objects (667) within this region and the second containing the HII regions outside it (31). An attempt was made to identify sources erroneously included in the original lists. This task was performed by using the POSS plates together with the Downes [93] SNR catalog and the Perek-Kohoutek [242] planetary nebulae catalog. The catalog provides coordinates (Galactic and Equatorial for the year 1950), angular dimensions, and a classification, similar to Sharpless', of shape, structure, and brightness.

3.2.2 Radio catalogs

- **The COBE-HII Catalog**
  As a part of the preparatory work for the COBE space mission and, in particular, of Galactic foregrounds studies[1], between 1977 and 1978, Witebsky [348], [349] compiled a list of Galactic HII regions by collecting all the information available

---

[1] See Chapter 2, section 2.2 for more details.

at the time. A first version of the catalog (the so-called *Master List*) includes data from Reifenstein et al. [252], Wilson et al. [343], Westerhout [341] and from observations of the California Institute of Technology - list B. The Master List has been subsequently revised and enlarged. The updated version (*New Master List*) contains additional data from the 1966 Australian Parkes Survey, which explored a substantial fraction of the Galactic plane, as well as from a vast number of other small lists and small catalogs. Overall, the New Master List is a combination of data from 19 papers, three of which (Berkhuijsen & Wielebinski [17], Israel et al. [170] and Mills & Aller [224]) report observations of HII regions in external galaxies, namely M31, M33 and the Small and Large Magellanic Clouds. The compilation, which contains 909 sources, has been realized by means of a hierarchical method based on the following criteria: degree of sky coverage, completeness of the survey, year of observation, availability of multi-frequency data. Flux densities are given at the reference frequency of 2.7 GHz, adopting the spectral index of -0.1 ($S_\nu \propto \nu^{-0.1}$) to extrapolate flux densities measured at other frequencies. Errors are not provided for any of the quoted physical quantities (i.e. flux density and angular diameter). Coordinates are Galactic.

- **The Kuchar & Clark Catalog**
  The catalog contains 760 HII regions with angular sizes of up to $10'$ at 4.8 GHz. The data have been obtained in a self-consistent manner from images of the Green Bank (Condon et al. [64]) – northern hemisphere – and Parkes-MIT-NRAO (Condon et al. [65]; Tasker et al. [310]) – southern hemisphere – 4.85 GHz radio continuum surveys. Nearly 35% of the sources have fluxes measured by these surveys for the first time. The catalog provides the following information for each source: coordinates (Galactic and Equatorial for the year 1950); peak flux; observed angular diameter; recombination line velocity (data are taken from the literature and refer to observations at various frequencies); comments on the source environment. Errors on flux density, angular size and line velocity are also reported.

3.3 The new catalog

A large amount of data on HII regions has become available after completion of the catalogs described in the previous section. This has motivated the construction of a new, up-to-date catalog.

The reason for producing a radio catalog of HII regions rather than an optical one resides in the fact that optical catalogs are severely limited by dust obscuration effects. Consequently, radio data more lickely succed in tracking the actual distribution of HII regions in the Galaxy. At the same time, as mentioned in section 2.2 of Chapter 2, we are interested in the ionized gas, both diffuse and localized, because of its implications as a foreground for CMB experiments and these are operated at radio frequencies. This subject will be discussed extensively in Chapter 5.

3.3.1 The Master Catalog

The construction of the full catalog (referred to as *Master Catalog*) involved several steps.

Selection of the original catalogs

The Master Catalog was compiled combining data given by the 24 papers listed in Table 3.1. In order to clarify our selection criterion, we briefly summarize the classification of HII regions by Lockman et al. [201]:

- **Ultra-compact HII regions (UCHII)**, characterized by very high EM[2], ($\sim 10^7$ cm^{-6} pc), angular sizes of the order of a few arcsec, and flux densities at radio wavelengths, of the order of tenths of Jy.
- **Compact HII regions**, having smaller EM ($\sim 10^{4-5}$ cm^{-6} pc), typical angular sizes of a few arcmin, and radio flux densities between a few Jy and a few hundreds Jy. An example is the Orion Nebula.
- **Diffuse HII regions**, with typical EM $\sim 10^3$ cm^{-6} pc, angular size between a few and tens of arcmin, and flux density at radio frequencies of a few Jy. A typical example is the Rosetta nebula.
- **Extended HII envelopes**, characterized by very low EM ($\sim$ 30-50 cm^{-6} pc). Not easily identified with structures with well defined boundaries, they have very low flux densities at GHz frequencies. Although the EHEs appear as a sort of *diffuse background*, they differ from the warm ionized gas for two reasons: the WIM has a typical EM orders of magnitudes smaller than the EHEs and is distributed throughout the Galaxy while these sources are confined to the plane.

We have included in the catalog only compact and diffuse HII regions, which however account for the bulk of the free electron condensations along the Galactic plane. We have considered single-dish medium-resolution observations, typically with beam-widths of a few arcmin, rather than interferometric or synthesis telescope surveys (Becker et al. [13]; Taylor et al. [313]) which usually achieve a resolution of a few arcsec. Also, we have not considered single-dish low-resolution observations (Westerhout [341]; Wilson & Bolton [342]), whose typical angular resolution is $\sim 1°$. Likewise we have disregarded surveys simply oriented to the study of the morphology and of the spectral behaviour of the diffuse Galactic radiation at centimeter wavelengths (Reich et al. [248]; Reich et al. [251]; Fürst et al. [115]; Fürst et al. [116]; Duncan et al. [96]).

---

[2] For a definition of the emission measure, EM, see Chapter 2.

Table 3.1: List of the references (in alphabetical order) for the catalog. l_{min} and l_{max} limit the longitude interval spanned by each survey. The range in latitude is $|b| \leq 2° - 4°$. † Number of sources after subtraction of non-thermal objects.
Notes: (a) the list of HII regions is obtained by cross-checking the continuum survey data with the radio recombination line survey by Lockman [200]; (b) early Parkes survey at 2.7 GHz; (c) Effelberg 100-m survey at 2.7 GHz; (d) Cygnus X; (e) nonuniform sky coverage; (f) Green Bank and Parkes-MIT-NRAO surveys cover almost the whole sky: HII regions have been identified from either optical or radio recombination line surveys along the disk.

Reference	l_{min}	l_{max}	ν (GHz)	HPBW (′)	Number† of sources
Altenhoff et al. [3]	335°	75°	1.4/2.7/5	10	325
Altenhoff et al.$^{(a)}$ [4]	2°	60°	5	2.6	265
Beard$^{(b)}$ [9]	331°	333°	2.7	7.4	13
Beard & Kerr$^{(b)}$ [10]	27°	38°	2.7	7.4	34
Beard et al.$^{(b)}$ [11]	345°	5°	2.7	7.4	72
Berlin et al. [18]	4°	10°	3.9	0.8×18.3	45
Caswell & Haynes [53]	190°	40°	5	4.2	308
Day et al.$^{(b)}$ [78]	307°	330°	2.7	8.2	109
Day et al.$^{(b)}$ [79]	37°	47°	2.7	8.2	48
Downes et al. [94]	357°	60°	5	2.6	169
Felli & Churchwell [102]	(*e*)	(*e*)	1.4	10	80
Fürst et al.$^{(c)}$ [114]	(*e*)	(*e*)	2.7	4.27	7
Goss & Day$^{(b)}$ [132]	6°	26°	2.7	8	85
Kuchar & Clark [188]	(*f*)	(*f*)	4.8	3.1/4.2	760
Mezger & Henderson [220]	(*e*)	(*e*)	5	6.3	17
Reich et al.$^{(c)}$ [249]	(*e*)	(*e*)	2.7	4.27	5
Reifenstein et al. [252]	348°	80°	5	6.5	105
Thomas & Day$^{(b)}$ [317]	288°	307°	2.7	8.2	39
Thomas & Day$^{(b)}$ [318]	334°	345°	2.7	8.2	29
Wendker$^{(d)}$ [340]	76°	84°	2.7	11	77
Wilson et al. [343]	282°	346°	5	4	132
Wink et al. [346]	(*e*)	(*e*)	5/15/86	2.6/1/1.3	112
Wink et al. [347]	359°	50°	14.7	1	84

Identification and removal of SNRs

The selected catalogs may contain in principle also some Galactic sources, different from HII regions, that we need to exclude from our Master Catalog. In particular, *filled-center* SNRs may easily be mistaken for HII regions: this type of SNR presents in fact an almost flat spectrum and a very bright central region. A typical source belonging to this class is the Crab Nebula, the remnant of a supernova exploded in 1054. Supernova remnants (SNRs) have been identified by cross-correlating the positions of catalogued sources with those of Galactic supernova remnants listed by Green [137]. The Green Catalog contains 215 objects. The identification has been performed taking into account the average position uncertainty of HII regions and of SNRs ($\sim 1'$ in both cases).

Flux densities and angular diameters

We provide the flux densities integrated over each source, S, and the source angular diameter, Θ_{HII}. In a few references (Wink et al. [346] at 86 GHz; Wink et al. [347]) only the peak value of the flux density is given. We have corrected this to a true value by assuming that the source has a Gaussian profile and using the observed diameter (see Rohlfs [268]).

The source angular diameter is given, by some authors (Altenhoff et al. [4], Downes et al. [94]; Wink et al. [347]), in terms of observed diameter, i.e. the true diameter convolved with the instrument beam. We derived a true diameter again assuming a Gaussian source profile. For source dimensions significantly smaller than the beam-width, only upper limits to the diameters could be derived. These values are also included in the Master Catalog, for completeness.

Other relevant data

In addition to the basic data on flux density and diameter, the Catalog includes additional information on source properties, such as: i) the notes by Kuchar & Clark [188] on the environment of each source, indicating whether the source is complex or if it has a strong source nearby; ii) radio measurements provided by surveys different from those listed in Table 3.1; iii) optical counterparts of the unobscured sources, obtained from the identification given in the Catalog by Társalková [208]; iv) radio recombination line data, given by Downes et al. [94], Caswell & Haynes [53], Kuchar & Clark [188], Reifenstein et al. [252], Wilson et al. [343], Wink et al. [346], Wink et al. [347], and Lockman [200].

Summary of the Master Catalog content

The catalog lists 1442 sources, observed by at least one of the surveys of Table 3.1 and recognized as Galactic HII regions. All relevant information from each of the references is retained. Measurements of individual HII regions are available at one or more of the following 8 frequencies: 1.4, 2.7, 3.9, 4.8, 5., 14.7, 15, and 86 GHz. This large data base is presented in the form of 11 *sub-catalogs*:

sub-catalog	1	coordinates (epoch 2000) and remarks
sub-catalog	2 / 3	flux density (Jy) / 1-σ (%) error
sub-catalog	4 / 5	diameter (arcmin) / 1-σ (%) error
sub-catalog	6 / 7	line velocity (km/sec) / 1-σ error (km/sec)

sub-catalog	8 / 9	line width (km/sec) / 1–σ error (km/sec)
sub-catalog	10 / 11	line temperature (K) / 1–σ error (K).

The sub-catalogs give, for each source, an identification number along with the position in Galactic and celestial coordinates. Apart from sub-catalog 1, each sub-catalog has 37 columns. The columns are in order of increasing frequency of observation; at each frequency different columns report the data from the references in Table 3.1, in alphabetical order. We note that for sub-catalog 6-11 (the radio recombination line data) the observations may refer to frequencies other than those in the main continuum catalog (in this case, the line frequency is reported). Appendix I gives a detailed description of the content of each sub-catalog.

3.3.2 The Synthetic Catalog at 2.7 GHz

The final task in bringing together the wide-spread radio data on HII regions is to construct a readily accessible catalog summarizing the basic information on each of the 1442 sources covered in the comprehensive data base of the Master Catalog. This Synthetic Catalog gives the best available data on flux density, angular diameter and, where available, the line velocity.

We have adopted, for the Synthetic Catalog, a reference frequency of 2.7 GHz because it lies in the middle of the frequency range of catalogs containing most of the data, namely 1.4, 2.7 and 5 GHz. We now describe our procedure to get the best-estimate values of the flux density at 2.7 GHz, diameter and velocity with corresponding error estimates.

Estimates of flux densities at 2.7 GHz

If direct flux density measurements at 2.7 GHz were not available, we adopted the following procedure:

1. if measurements are available only at one frequency, we extrapolated the flux density to 2.7 GHz using a spectral index of -0.1;
2. whenever measurements at 1.4 and 5 GHz are available, the 2.7 GHz flux density was obtained by interpolation between these two frequencies if we have both, or by extrapolation with a spectral index of -0.1 if we have just one; measurements at other frequencies, if any, are ignored;
3. if measurements are not available at either of the above frequencies, we extrapolated with the usual spectral index the flux density at the frequency nearest to 2.7 GHz;
4. for the purpose of extrapolating to 2.7 GHz, measurements at frequencies very close to each other, such as 4.8 and 5 GHz, or 14.7 and 15 GHz were considered to be at the same frequency and their weighted average was adopted.

We consider the data at 3.9, 14.7, 15 and 86 GHz to be less reliable than those at 1.4 and 4.8/5 GHz for the following reasons: the 3.9 GHz measurements come from observations of the RATAN-600 telescope and they may be significantly affected by the ellipticity of the antenna pattern (see Table 3.1); at 14.7 and 15 GHz our HII regions are frequently resolved and the determination of their total flux density is correspondingly difficult; at 86 GHz, in addition to the higher resolution, dust emission may contribute substantially to the observed flux. Moreover, we prefer to interpolate between 1.4 and 5 GHz rather than extrapolate to 2.7 GHz directly from only one of these two frequencies because we have no information on the free-free self-absorption frequency. When multiple observations are available at the same frequency, a weighted mean flux density was computed, using the errors discussed below.

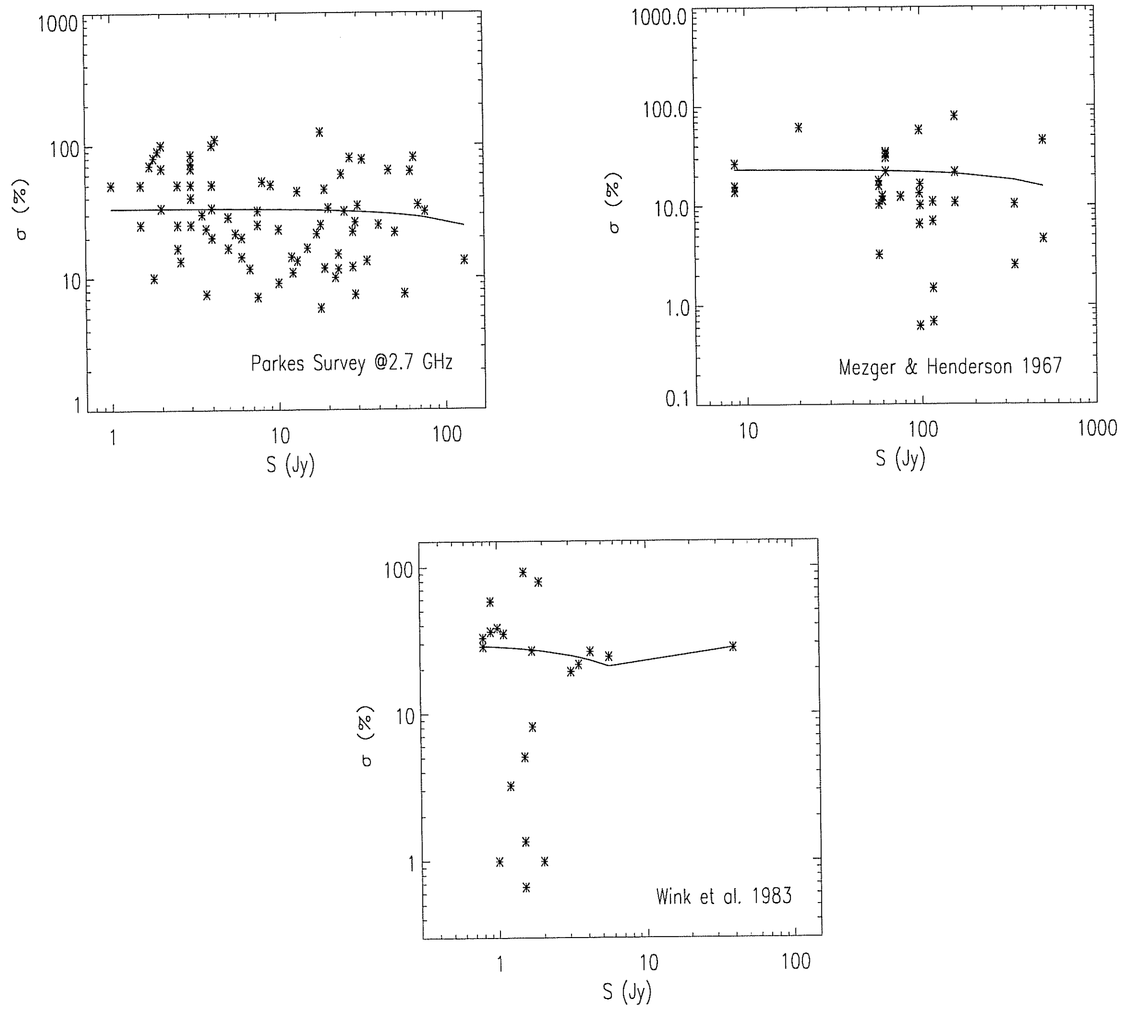

Figure 3.1: Results of the flux error estimate for: earlier Parkes survey at 2.7 GHz (top left); Mezger & Henderson [220] (top right); Wink et al. [347] (bottom center). $\sigma(S_*)$ is defined as $100(S_* - S)/S$. Overlaid – solid line – is the best fit function.

For the majority of the sources flux density errors are quoted in the original papers. Whenever errors are not given, an estimate was made by looking for sources with additional flux density measurements and computing the percentage difference $\sigma = 100(S_* - S)/S$, S_* being the flux density in the catalog without errors. The mean value of σ as a function of S was fitted (after having removed the relatively small number of points with a dispersion $\gtrsim 130\%$) with a constant, $\sigma = a$, with a linear relation, $\sigma = a + bS_*$, and with a quadratic expression, $\sigma = a + bS_* + cS_*^2$. We have considered also fits with a constant, linear, and quadratic dependence of $\log \sigma$ on $\log S_*$, but we have chosen to use the larger, and thus more conservative, values of $\sigma(S_*)$ estimated using natural (not logarithmic) quantities.
Fig. 3.1 illustrates the results of the procedure we have described. For example, to estimate the errors for the early Parkes 2.7 GHz catalogs we have looked for sources in common with other catalogs at the same frequency, namely, Altenhoff et al. [3], Fürst et al. [114], Reich et al. [249], Wendker [340]). In particular, there are 105 sources in common with Altenhoff et al. [3]. The mean σ is quite well fitted by the law $\sigma \simeq 33.5 - 0.1 \times S$ (with S in Jy), consistent with the 10–30 % errors quoted by Altenhoff et al. [3].
Similar comparisons have been carried out for the Mezger & Henderson [220] data and for the Wink et al. [347] data. Since the number of coincidences of Mezger & Henderson sources with sources in each individual sample at the same frequency is too small, we have brought together sources common to any other catalog at the same frequency (5 GHz), reaching a total of 38 sources. In the case of the Wink et al. [347] catalog, the error estimate is based on the 21 sources in common with the Wink et al. [346] catalog.
The errors on the derived flux densities at 2.7 GHz were estimated applying the standard rules for the propagation of errors, neglecting the uncertainty in the spectral index.
Table 3.2 summarizes the errors quoted in the original papers and those estimated in this work.

Angular diameter

The published diameter data are not as comprehensive as the flux density data. Nevertheless we have been able to assign a value of the diameter, with its error, to each source. For 42 % of the sources (from the Parkes catalogs and from Mezger & Henderson [220], Wendker [340], Wink et al. [346], Wink et al. [347], Berlin et al. [18]) errors on diameters are not given. For 14 % of the sources no diameter is given; for these we derive an indicative value.
The diameters given in the Synthetic Catalog are:

1. values measured at 2.7 GHz, if available;
2. failing that, measurements at 4.8/5 GHz;
3. in the absence of measurements at 2.7 and 4.8/5 GHz, the weighted average of available data, excluding those at 14.7/15 GHz (no diameter data are available at 86 GHz);

4. values measured at 14.7/15 GHz for lack of data at other frequencies.

Values at 14.7/15 GHz are preferably excluded because, as noted above, sources are easily resolved at these frequencies. In each case, when multiple observations are available at the same frequency, a weighted mean is computed, using the errors discussed below.
For the 14% of HII regions lacking direct measurements, an indicative diameter was estimated exploiting the (weak) correlation between diameter and flux density, illustrated in Fig 3.2. A linear fit yields $\theta(\text{arcmin}) = 2.25 \times S(\text{Jy})$ with a typical error of a factor of 2–3. In the Synthetic Catalog a label marks diameter estimates based on the above relation.

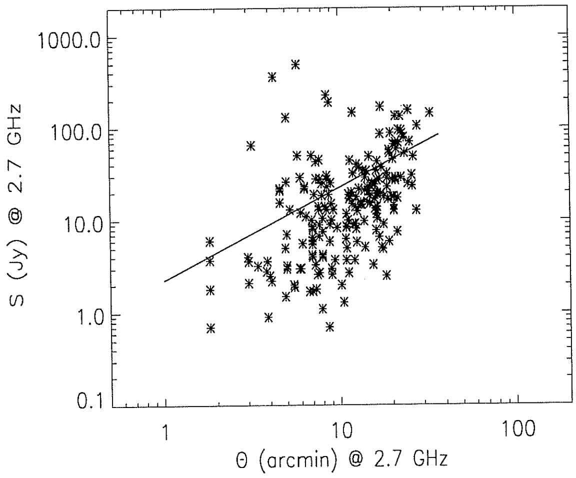

Figure 3.2: Correlation between flux densities at 2.7 GHz and angular diameters observed at the same frequency. The solid line represents the linear best-fit relation.

Whenever errors on diameters were not provided, they were estimated following a strategy similar to that used for errors on flux densities. The main difference is that, for diameters, we relax the requirement of comparing data at the same frequency. As shown in Fig. 3.4, there is no significant difference in the diameters measured at 2.7 GHz (the Parkes survey) and at 5 GHz (Altenhoff et al. [3], Mezger & Henderson [220] and Reifenstein et al. [252]). On the other hand, provided that an adequate number of sources in common is retrieved, we prefer to use surveys at the same frequency and with similar angular resolution.

We computed the percentage differences, σ, between the angular diameters, Θ_*, given in catalogs without error estimates and independent measurements, Θ, of the same objects: $\sigma = 100(\Theta_* - \Theta)/\Theta$. Again, we derived the global average of the σ/Θ_* ratio and the best fit linear and quadratic dependence of the mean value of σ on Θ_* (and of $\log\sigma$ on $\log\Theta_*$). Again we adopted the larger (hence, more conservative) error estimates obtained from the fits in terms of natural (i.e., non-logarithmic) quantities.

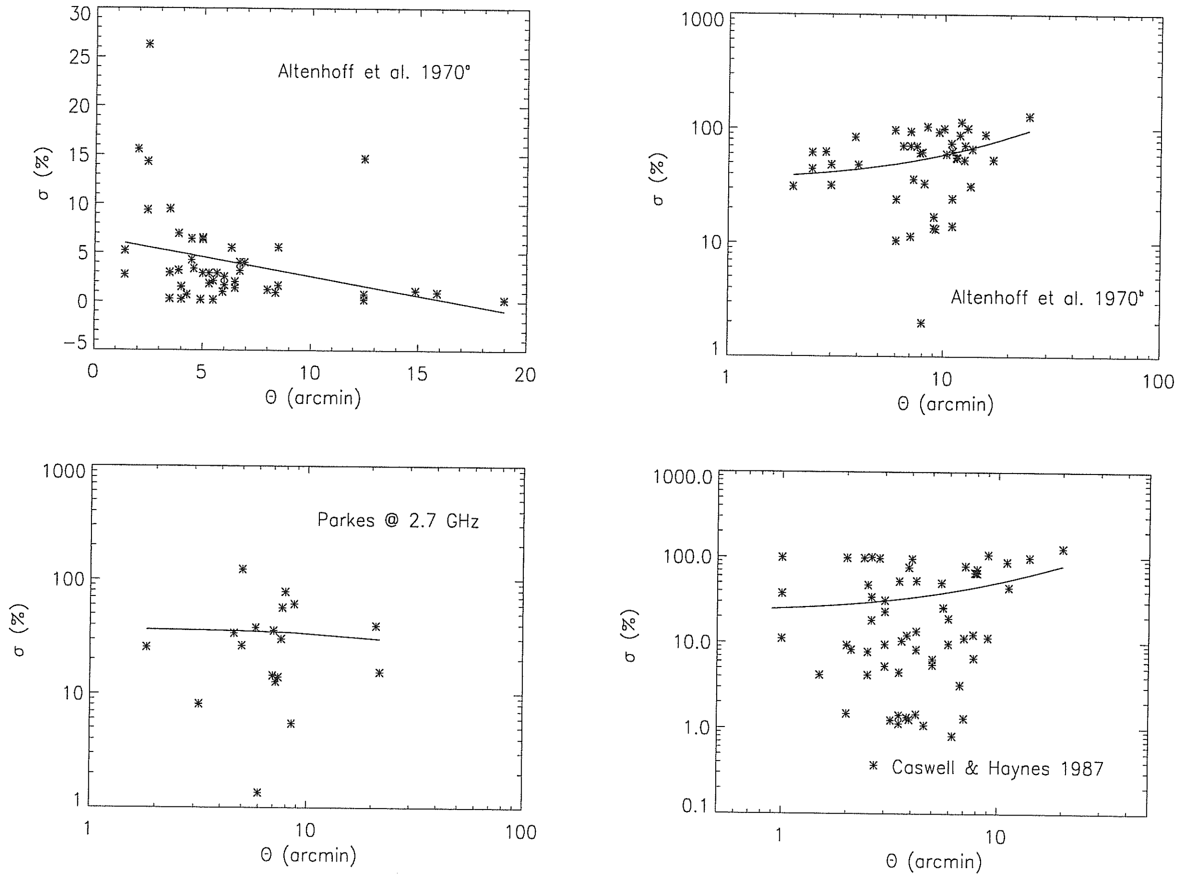

Figure 3.3: Estimates of percentage errors, $\sigma(\Theta_*) = 100(\Theta_* - \Theta)/\Theta$, on angular diameters for the samples of: Altenhoff et al. 1970^a (top left); Altenhoff et al.^{b} [3] (top right); earlier Parkes survey at 2.7 GHz (left, second row); Caswell & Haynes [53] (right, second row). Overlaid – solid line – is the best fit function.

Figures 3.3 and 3.5 show the results of the error estimates. In particular, we consider the comparison between the following data-sets (the first one is that for which we are estimating the errors): Altenhoff et al.^{a} [3] vs. Reifenstein et al. [252] (48 common sources); Altenhoff et al.^{b} [3] vs. Kuchar & Clark [188] (63 common sources); Caswell & Haynes [53] vs. Wilson et al. [343] (79 common sources); early Parkes 2.7 GHz Survey vs. Reifenstein et al. [252] (31 common sources); Felli & Churchwell [102] vs. Kuchar & Clark [188] (21 common sources); Wendker [340] vs. Reifenstein et al. [252] (8 common sources); Wink et al. [347] vs. Downes et al. [94] (59 common sources); Wink et al. [346] vs. Altenhoff et al. [4] (53 common sources).
The data in the Altenhoff et al. (1970) catalog have been split because the diameters have been measured in two different ways: they were partly obtained from a survey of Galactic sources made at 5 GHz with the 140-ft antenna - beamwidth 6′ (W.J. Altenhoff, P.G. Mezger and J. Schraml, private communication), and partly were measured directly from contour maps. The set of sources for which the size was measured in the 5 GHz

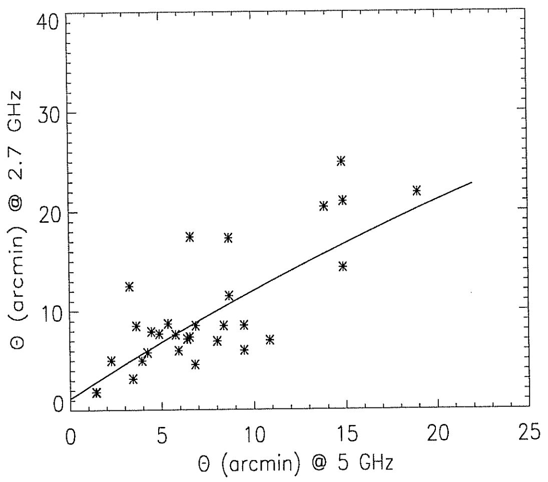

Figure 3.4: Comparison of diameter measurements at 2.7 GHz (y-axis) and at 5 GHz (x-axis). The best fit function is: $\Theta_{2.7\mathrm{GHz}} = 1.17 + 1.17 \times \Theta_{5\mathrm{GHz}}$. Data are from: earlier Parkes survey (2.7 GHz data); Altenhoff et al.[a] [3], Mezger & Henderson [220]; Reifenstein et al. [252] (5 GHz data).

survey is denoted as Altenhoff et al.[a] [3] while the remaining sources are denoted by Altenhoff et al.[b] [3]. In the case of the Berlin et al. (1985) catalog, which has a small number of matches with other catalogs, the error has been estimated as the average value of σ. Table 3.2 summarizes the estimated and quoted errors on diameters in the Synthetic Catalog.

Summary of the content of the Synthetic Catalog

The Synthetic Catalog summarizes the radio frequency information on 1442 Galactic HII regions. It contains the position, flux density, diameter data for each HII region, supplemented by velocity data where available. To those HII region with no published diameter data, an indicative diameter is given (marked by $**$) on the basis of the flux-size correlation in Fig 3.2. For sake of illustration, the first ten lines of the Synthetic Catalog are reported in Table 3.3. The line velocity value that we quote in Col. 9 is the weighted average of the available data (see Sect. 3.3.1 for details). Although the original measurements can be, for the same source, at different frequencies, the weighted average of these data is a meaningful quantity and provides a useful kinematic indication. Since the line velocity is predominantly an effect of the Galactic rotation motion, it does not strongly depend on the frequency of observation.

Table 3.2: Summary of percentage errors on flux densities and angular diameters. Errors marked by $*$ have been estimated by the authors of the Synthetic Catalog. Errors marked by $**$ correspond to the indicative diameters estimated by means of the flux density-angular size correlation in Fig 3.2.
In the linear relationships between error and flux-density or angular size, flux densities are in Jy and angular sizes in arcmin.

Reference	% flux error	% size error
Altenhoff et al.[a] [3]	10/30	$6.5-0.4\times\Theta$ ($*$)
Altenhoff et al.[b] [3]	10/30	$33.9+2.5\times\Theta$ ($*$)
Altenhoff et al. [4]	5	10
Beard [9]	$33.5-0.1\times S$ ($*$)	300 ($**$)
Beard & Kerr [10]	$33.5-0.1\times S$ ($*$)	$37-0.3\times\Theta$ ($*$)
Beard et al. [11]	$33.5-0.1\times S$ ($*$)	$37-0.3\times\Theta$ ($*$)
Berlin et al. [18]	10	72.5 ($*$)
Caswell & Haynes [53]	10	$22.1+2.8\times\Theta$ ($*$)
Day et al. [78]	$33.5-0.1\times S$ ($*$)	300 ($**$)
Day et al. [79]	$33.5-0.1\times S$ ($*$)	300 ($**$)
Downes et al. [94]	5	10
Felli & Churchwell [102]	15/35	77.4 ($*$)
Fürst et al. [114]	10	300 ($**$)
Goss & Day [132]	$33.5-0.1\times S$ ($*$)	$37-0.3\times\Theta$ ($*$)
Kuchar & Clark [188]	10/20	16/25
Mezger & Henderson [220]	23.3($*$)	20/50
Reich et al. [249]	10	300 ($**$)
Reifenstein et al. [252]	15	3
Thomas & Day [317]	$33.5-0.1\times S$ ($*$)	300 ($**$)
Thomas & Day [318]	$33.5-0.1\times S$ ($*$)	300 ($**$)
Wendker [340]	6	$-73.6+17.6\times\Theta-0.5\times\Theta^2$
Wilson et al. [343]	15	5
Wink et al. [346]	5/15	$73.5-52.1\times\Theta+11.1\times\Theta^2$ ($*$)
Wink et al. [347]	$30.3-1.9\times S+0.1\times S^2$ ($*$)	$85.8-38.1\times\Theta+5.2\times\Theta^2$ ($*$)

3.3.3 Statistical properties of the Synthetic Catalog

The Synthetic Catalog combines the observational data from 24 catalogs with various flux density limits and different angular resolutions. The Kuchar & Clark 1997 catalog, for example, reaches a sensitivity of 30 mJy but is not sensitive to sources with diameters greater than $\sim 10'$ due to its beam-switching strategy. Other surveys (e.g. Altenhoff et al. [3]) are sensitive to a wide range of angular scales but include only sources stronger than 1 Jy. We now consider the properties of the sources listed in the Synthetic Catalog in the light of these selection criteria.

Table 3.3: A selection of sources from the Synthetic Catalog is shown. The arrangement of column is as follows:
- Col. 1: source-numbering (records from 1 to 1442)
- Col. 2-3: galactic coordinates, l and b
- Col. 3-4: celestial coordinates (epoch 2000)
- Col. 5-6: derived 2.7 GHz flux density and 1–σ error (Jy)
- Col. 7-8: derived angular diameter and 1–σ error (arcmin)
- Col. 9-10: velocity relative to the LSR and 1–σ error (km/sec)
- Col. 11: notes on individual sources (see Sect. 3.3.2 and Appendix I for details)

N	l	b	RA	DEC	S	σ_S	θ	σ_θ	V_{LSR}	$\sigma_{V_{LSR}}$	Notes
1	0.1	0.0	17 45 51.3	-28 51 08	230.0	24.1	5.9	0.5	-27.4	4.0	W24
2	0.2	-0.1	17 46 29.0	-28 49 07	209.4	10.5	10.7	0.5	24.5	3.5	
3	0.2	-0.0	17 46 05.6	-28 46 00	177.6	38.1	9.2	0.5	-12.7	3.5	W24
4	0.3	-0.5	17 48 17.0	-28 56 25	2.5	0.7	2.7	1.7	20.0	4.9	C,S
5	0.4	-0.8	17 49 41.7	-29 00 33	8.0	2.6	7.0	2.3	20.0	4.9	C,S
6	0.4	-0.5	17 48 31.1	-28 51 17	4.1	1.0	3.9	1.8	24.0	4.9	C,S
7	0.5	-0.7	17 49 32.2	-28 52 19	2.9	0.9	2.3	1.4	17.5	4.9	C
8	0.5	-0.1	17 47 11.6	-28 33 44	28.3	4.0	3.3	1.4	45.8	5.0	S,X
9	0.5	0.0	17 46 48.2	-28 30 37	40.3	8.6	4.8	0.3	47.1	2.0	
10	0.6	-0.9	17 50 33.3	-28 53 19	2.5	0.8	2.4	1.3	15.0	4.9	S,S21,RCW1

Completeness and flux density limit

A useful way of investigating the completeness of a catalog is to plot the integral count N($> S$) as a function of flux density S. As shown by Fig. 3.6, the bright tail (300 Jy $\geq S_{2.7\mathrm{GHz}} \geq 70$ Jy) of the integral counts, $N(> S)$, of the catalogued HII regions exhibits the Euclidean slope [$N(> S) \propto S^{-3/2}$] as expected for the nearest sources (within a distance not exceeding the thickness of the HII layer). At fainter fluxes the counts flatten to $N(> S) \propto S^{-1}$, consistent with the 2-D (disk-like) distribution of more distant sources. Below $\simeq 7$ Jy the counts become still flatter, suggesting the onset of a substantial incompleteness.

The completeness limit is to a large extent determined by source confusion. The surface density of catalogued sources reaches values of one source per few beams in the region $\pm 60°$ around $l = 0°$, $b \sim 0°$, for a typical $10'$ beam. As extensively discussed in the literature (e.g., Scheuer [273]; Condon [63]; Hogg [164]) confusion becomes important at flux levels at which there are more than 1/30 sources per beam. Correspondingly, it is very difficult to resolve into individual sources the structure seen right in the Galactic plane, particularly towards the Galactic center. Thus, the majority of weak HII regions are actually found in less crowded areas, such as the anti-center region or regions at $|b| > 1°$.

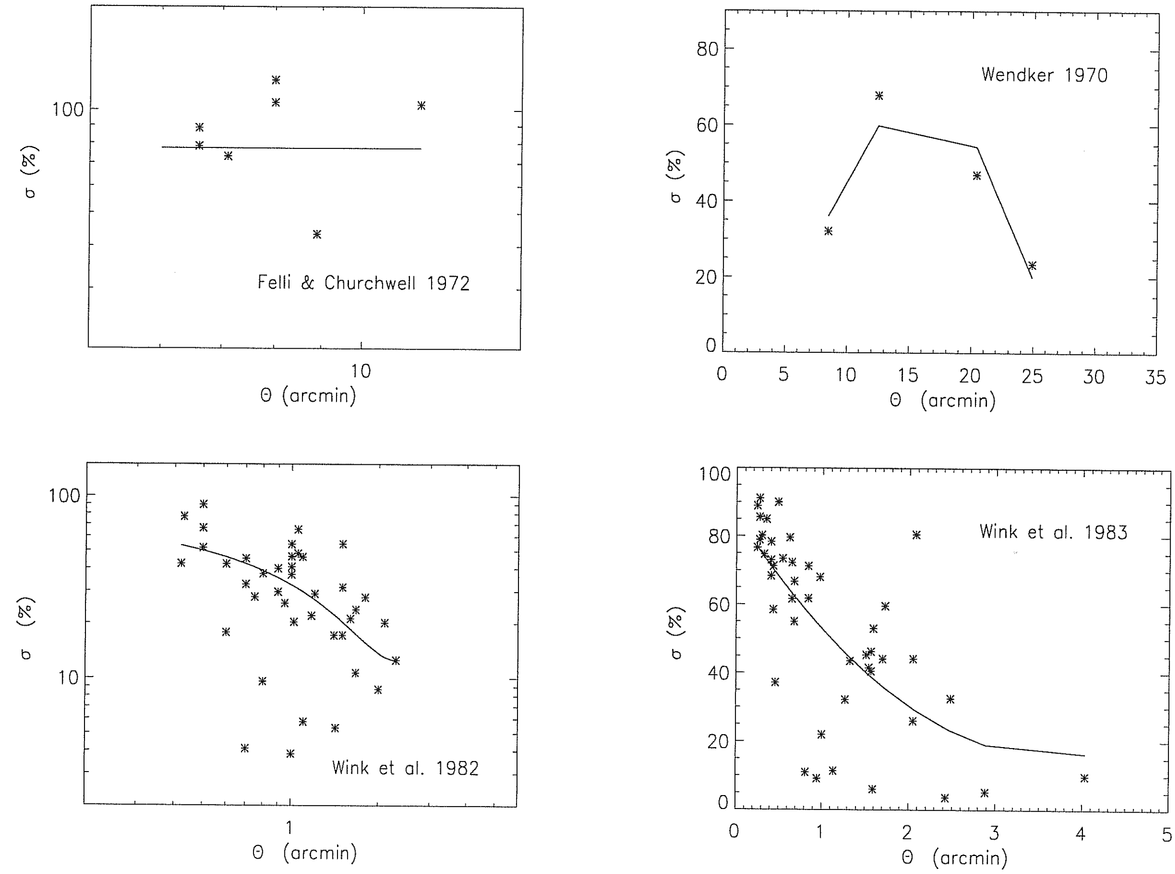

Figure 3.5: Results of the percentage error estimate, $\sigma(\Theta_*) = 100(\Theta_* - \Theta)/\Theta)$, for: Felli & Churchwell [102] (left, third row); Wendker [340] (right, third row); Wink et al. [346] (bottom left); Wink et al. [347] (bottom left). Overlaid – solid line – is the best fit function.

Spatial distribution

The Galactic latitude and longitude distribution of the HII regions in the Synthetic Catalog are shown in Fig 3.7. A striking feature is the narrow distribution in Galactic latitude where the full width at half power is 0.95° when averaged over all longitudes; the mean Galactic latitude is b=0.05°. This narrow distribution reflects the distribution of the O and B stars responsible for the ionization.

The main concentration in longitude is at $|l| < 60°$ where the line of sight cuts the spiral arms internal to the local spiral arm in which the Sun lies. There are also discernable peaks at $l \sim \pm 80°$ associated with the local arm; the peak at $l \sim 80°$ is the Cygnus X region where Wendker [340] identified 77 HII regions. There is a clear deficit of sources in the anticentre region of the Galaxy (l=90°–270°). Although there is a less complete coverage in this sector of the Galactic plane as indicated in Table 3.1, the large deficit of sources is real. The optical study of the distribution of HII regions in the outer Galaxy

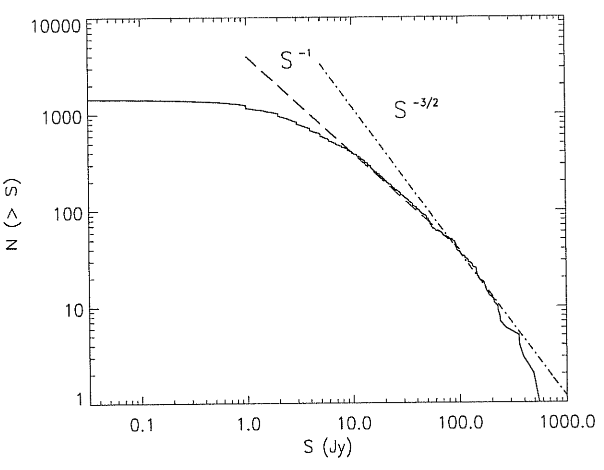

Figure 3.6: Cumulative counts N(> S) of HII regions in the catalog by Paladini et al. (2003).

by Fich & Blitz [105] indicate that they are limited to R < 20 kpc.

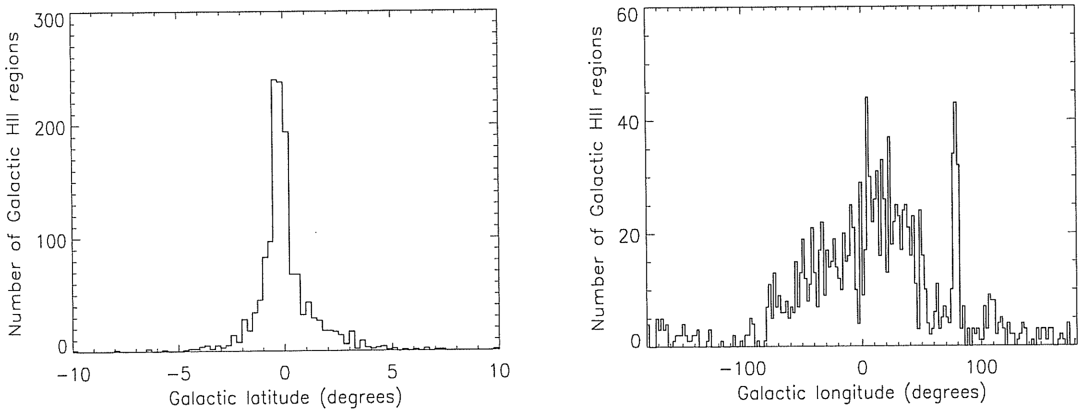

Figure 3.7: Left panel: Galactic latitude distribution of the HII regions of the Synthetic catalog. The mean Galactic latitude is b=0.05°. Right panel: Galactic longitude distribution.

3.4 Conclusions

We have collected multifrequency radio data of Galactic HII regions from 24 published works and built a self-consistent database of 1442 sources. This work has resulted in the construction of what we have called Master Catalog which consists of 11 sub-catalogs storing the original information from the source references. In particular, the sub-catalogs list flux densities and diameters as well as radio line velocities, line widths and line temperatures with their respective errors.

From this large data set, we have produced a readily accessible Synthetic Catalog giving the flux density, diameter and velocity (where available) at 2.7 GHz, the frequency where most data are given. Errors on these observed parameters are derived using the procedures discussed in Sect. 3.3.2.

It should be emphasized that the Catalog is a compilation of published radio data on HII regions; it is not a complete survey down to the faintest flux density level listed. We argue in Sect. 3.3.2 that it is probably complete to a flux density of 7 Jy. Nevertheless, the Catalog provides an up-to-date list of the brightest HII regions available for further study at microwave and sub-millimeter wavelengths. The Master Catalog and the Synthetic Catalog are available via ftp at: cdsarc.u-strasbg.fr.

Chapter 4

Spatial distribution of Galactic HII regions

4.1 Introduction

We have seen (Chapter 2, section 2.3.3) that a spiral arm structure appears to be mandatory in any electron density model that aspires to realism. The major argument supporting this statement is (see Fig. 2.5) the asymmetry of the distribution of DM vs Galactic longitude. Another direct demonstration of the validity of this picture is also provided, as reported by Cordes & Lazio [68], by the calculation of the DM deficit for individual pulsars for various density models, defined as the difference between the model DM integrated to infinite distance and the pulsar DM: ΔDM = DM - $\mathrm{DM_{inf}}$ (model). When the spiral arm structure is not included in the considered model the number of DM deficits is quite large, especially in the direction of the Carina-Sagittarius arm ($l \sim 65^0 \pm 10^0$) and up to $l \sim +10^0$. This broad longitude range encompasses all of the spiral arms interior to the solar circle.
As it is well known, HII regions are among the most reliable tracers of the Galactic spiral structure (Vallèe [326]). Consequently, a good knowledge of the spiral pattern requires an accurate reconstruction of their spatial distribution. Recovering such a distribution, however, is complicated by the distance degeneracy problem. While the galactocentric distances can be derived from the Galactic rotation curve if velocity data are available, there are in general two solutions ("near" and "far") for the distance from the Sun of regions within the solar circle.

In this chapter, we address this problem by exploiting the rich information content of the extensive radio catalog of Galactic HII regions presented in Chapter 3. The chapter is organized as follows. In section 4.2 we recall the basic features of the spiral arm component which have been included in recent models of the electron density distribution (namely, the TC93 [311] and the NE2001 [67], [68] models). In section 4.3, we describe, for our sample, the derivation of galactocentric distances and investigate the radial gradient of the electron temperature, discovered in previously published works. In section 4.4 we discuss distances from the Sun and methods to overcome the degeneracy; the thickness of the HII layer is also estimated. The main conclusions are summarized in section 4.5.

4.2 The spiral arm component in electron density models

- **TC93 model**
  The TC93 model has been the first to take into account an asymmetric component by including the contribution of spiral arms. The skeleton model of the arm shapes (e.g. the arm centroids) is the HII region map published by Georgelin & Georgelin [125]. Additional information on the shape and relative arm densities is taken from the surveys of HII regions by Downes et al. [94] and Caswell & Haynes [53]. While keeping the locations of the spiral arms fixed, some particular features of the spiral arms near the tangent point have been determined by using the dependence of pulsar dispersion measures on Galactic longitude. Finally, a least-squares grid-search procedure has been applied to evaluate the remaining free parameters of the model (the half-width w_a, the scale height h_a, the Galactic radial cutoff distance, A_a and the fluctuation parameter F_a[1]). The resulting four-arm pattern (see Fig. 4.1) is basically identical to that proposed by Georgelin & Georgelin [125]. However, the axis of arm 3 has been moved slightly inward in regions just inside the solar circle to correspond better with the measurements by Downes et al. [94] in the northern hemisphere. Also, arm 4 has been extended at its outer end as suggested by the data by Caswell & Haynes [53].

- **NE2001 model**
  The definition of the spiral arms given in the TC93 model has been revised due to the following reasons:

  1. recently discovered pulsars seem to require thicker arms since the TC93 model provides too few electrons for measured DMs;
  2. there is evidence for the influence of a local (Orion-Cygnus) arm on the scattering of some pulsars;
  3. the spiral arms in TC93 have been truncated arbitrarily in their arc lengths and there is evidence suggesting that they need to be extrapolated further;
  4. it is worthwhile to consider mathematically defined forms of the spiral arms, such as the logarithmic spiral forms, which are also used to describe to magnetic field in our Galaxy and in external galaxies (Vallèe [328]; Beck et al. [12]; Wainscoat et al. [334]).

  The adopted functional form of the spiral arm density is[2]:

---

[1] See Chapter 2, section 2.3.3, eq. (2.51), (2.54).

[2] See also Fig. 2.7 in Chapter 2.

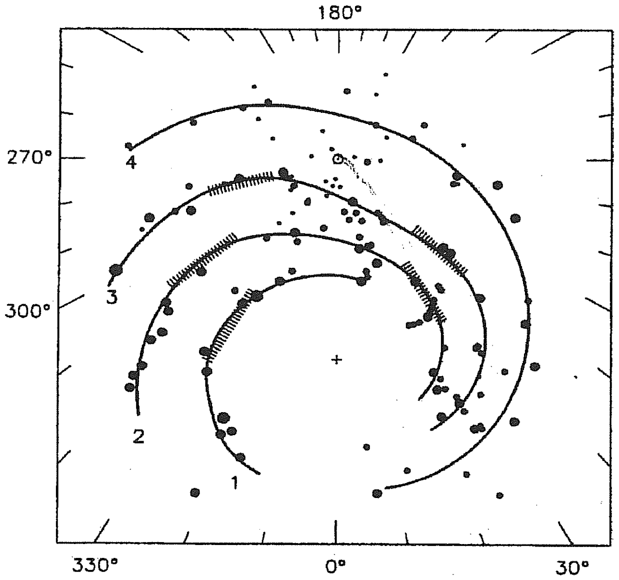

Figure 4.1: TC93 spiral arm model. Circles correspond to HII regions and hatched areas correspond to the directions of intensity maxima in the thermal radio continuum and neutral hydrogen emission (from Taylor & Cordes [311].)

$$n_{arms} = n_a G_a(\mathrm{x}) \tag{4.1}$$

with:

$$G_a(x, y, z) = \sum_{j=1}^{N_{arms}} f_j g_{a_j}(r, s_j/w_j) h(z/h_j h_a) \tag{4.2}$$

where the summation ranges over N_{arms}=5: the canonical 4 spiral arms, plus the local Orion-Cygnus arm. The factors f_j, w_j and h_j allow the control of the electron density, width and scale height of each spiral arm. Each arm has also a separate F parameter, F_{a_j}, $j = 1, 5^3$.

It is important to note that the shapes of the arms have been perturbed in the vicinity of the Sun to match the shapes defined in TC93. These perturbations have been guided by the detailed distribution of DM in Galactic longitude and by the locations of spiral arm tangents according to a number of tracers such as HII regions. The resulting spiral arm pattern is shown in Fig. 4.2.

---

[3] For the definition of the fluctuation parameter F see Chapter 2, section 2.3.3.

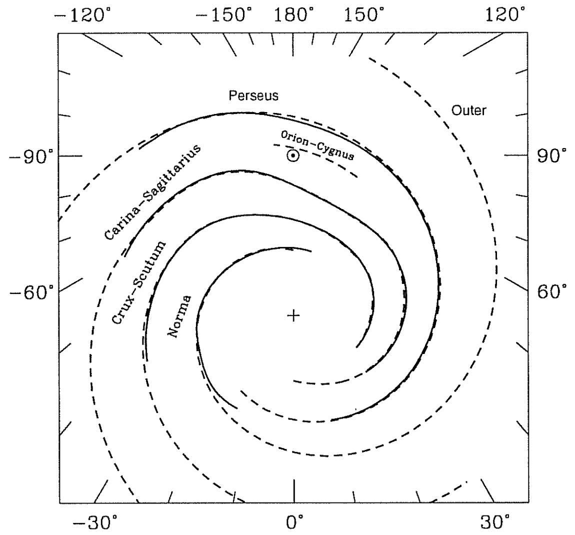

Figure 4.2: NE2001 spiral arm model (dashed lines): four-arm logarithmic spiral model combined with a local arm (Orion-Cygnus). The shape of the logarithmic arms is modified to match some of the features of the TC93 model (shown with solid lines) (from Cordes & Lazio [67]).

4.3 Galactocentric distances of HII regions

4.3.1 Distance estimates

In the previous chapter we have described the construction of an extensive catalog of Galactic HII regions. The catalog contains radio recombination line velocities for $\simeq 800$ of the listed HII regions. The references for the velocity data and the lines used are listed in Table 4.1. This is, by far, the largest sample used to derive distances. The present analysis also improves on the earlier ones because of the adoption of an updated Galaxy rotation curve. Previous studies (Caswell & Haynes [53]; Downes et al. [94]) were based on $\simeq 300$ sources and used Schmidt's [275] rotation curve or slightly modified versions of it.

The rotation velocity Θ around the Galactic centre of an object at galactocentric distance R, Galactic longitude l, and with radial velocity V_r in the local standard of rest, is given by:

$$\Theta = (R/R_0)(\Theta_0 + V_r/\sin l) \tag{4.3}$$

where Θ_0 and R_0 denote, respectively, the rotation velocity and the galactocentric

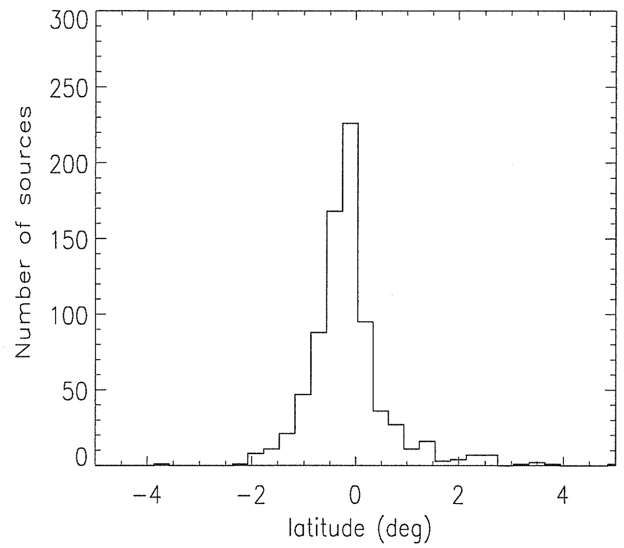

Figure 4.3: Galactic latitude distribution of $\simeq$ 800 sources with recombination line velocities.

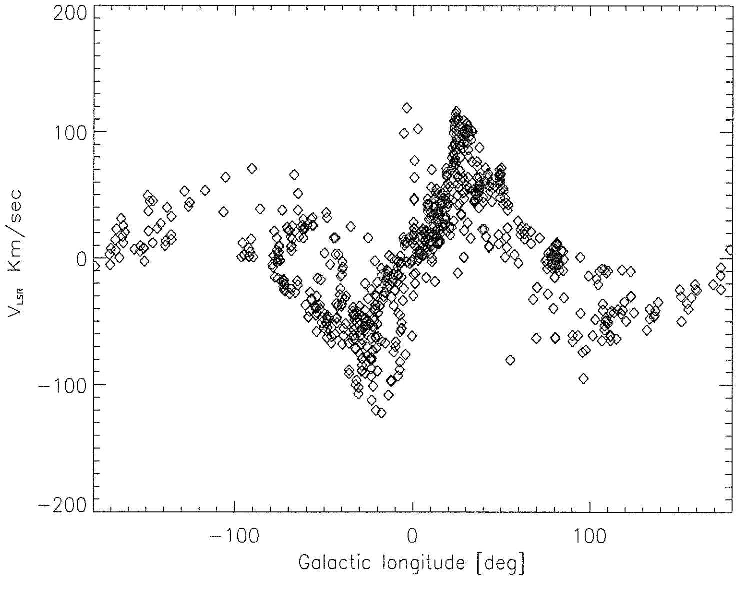

Figure 4.4: (l,v) diagram of the recombination line velocities of the catalogued HII regions used in the analysis.

Table 4.1: References for velocity data.

Reference	*Line*
Caswell & Haynes [53]	H109α/H110α
Downes et al. [94]	H110α
Lockman [200]	H85α/H87α/H88α
Reifenstein et al. [252]	H109α
Wilson et al. [343]	H109α
Wink et al. [346]	H76α/H90α
Wink et al. [347]	H76α

distance of the Sun. We adopt the IAU-recommended values of $R_0 = 8.5\,\mathrm{kpc}$[4] and $\Theta_0 = 220\,\mathrm{km\,s^{-1}}$ (Kerr & Lynden-Bell [181]). From eq. (4.1) we can derive R from radial velocity measurements, if the rotation curve $\Theta(R)$ is known. We have used the linear expression derived by Fich, Blitz and Stark [106] (hereafter FBS89), holding for galactocentric distances between 3 and 17 kpc:

$$\Theta = (221.64 - 0.44R)\,\mathrm{km\,s^{-1}} \tag{4.4}$$

where R is in kpc (see Fig. 4.5).

The outer part of the FBS89 rotation curve was constructed using spectrophotometric distances and velocities of HII regions. Our sample has some sources in common with theirs, namely those with CO velocity measurements. To avoid circularity we have excluded such sources from further analysis. Thus the velocity measurements we have used are fully independent of those used by FBS89. As discussed by Blitz [23] and FBS89, the use of HII regions to derive a rotation curve yields relatively small absolute errors compared with methods relying on other classes of objects such as star clusters, planetary nebulae, carbon stars, and diffuse atomic hydrogen. On the other hand, the good agreement of the FBS89 rotation curve with determinations using other methods indicates that systematic errors specific to HII regions cannot be large except, perhaps, in special regions where systematic, non-circular, velocity components (e.g. streaming motions) are present. One such region is the Perseus arm where a mean streaming velocity $\simeq$ 12 km sec^{-1} has been found by Brand & Blitz [28]. As a consequence, the distances of 36 sources in that region may be affected by a substantial systematic error.

The mean measurement error on V_r is $\simeq 1\,\mathrm{km\,s^{-1}}$, although with a large scatter (the minimum error is $0.02\,\mathrm{km\,s^{-1}}$; the maximum $10.7\,\mathrm{km\,s^{-1}}$). The corresponding error on the derived values of R are typically of order 1%. On the other hand, random motions can add a significant uncertainty to the computed values of R. The average local peculiar velocities reported by Stark & Brand [308] and Clemens [59] are $\simeq 5\,\mathrm{km\,s^{-1}}$. To curtail

---

[4] We use the IAU recommended value although recent works favor a smaller distance, $\sim 7.1 \pm 0.4$ kpc (e.g. Olling & Merrifield [230]).

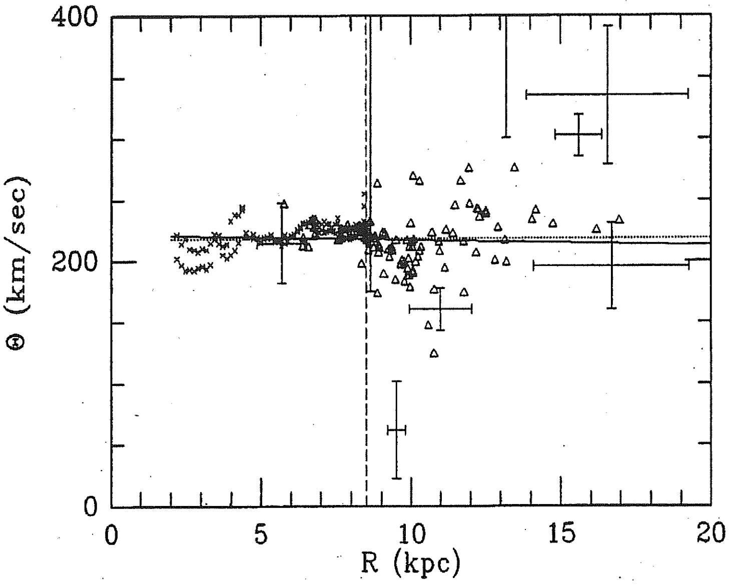

Figure 4.5: Data used for the FBS89 rotation curve determination. Crosses denote HI tangent point data and triangles CO data. Error bars are shown for a few outlying HII regions. Also shown are the best-fit linear (solid line) and power-law (dashed line) FBS89 rotation curves for the IAU standard values $R_0 = 8.5$ kpc and $\theta_0 = 220$ km sec^{-1} (the figure is from Fich et al. [106]).

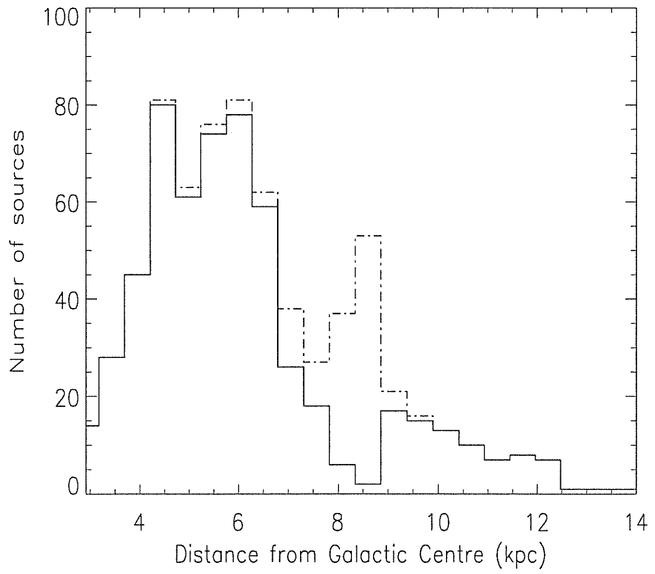

Figure 4.6: Distribution of galactocentric distances of all $\simeq$ 800 sources with velocity data (solid line). The dot-dashed line shows the distribution of 575 sources with radial velocities, $|V_r| > 10\mathrm{km\,s}^{-1}$.

this effect, we consider only objects with $|V_r| \geq 10\,\mathrm{km\,s^{-1}}$. As a consequence, we are left with 575 sources.

The distribution of the derived galactocentric distances is shown in Fig. 4.6, where the peaks corresponding to the spiral arms at $R = 4$, 6 and 8 kpc are visible. The latter peak, due to sources on or near the solar circle, however disappears if we consider only sources with $|V_r| \geq 10\,\mathrm{km\,s^{-1}}$.

4.3.2 The Electron temperature data and the Galactocentric distance gradient

Determinations of the electron temperatures are, for HII regions, particularly important. In fact, this physical quantity is used to compute the abundances of heavy elements and these, in turn, enable us to trace the Galactic chemical evolution. In particular, the electron temperature needs to be estimated with high accuracy: as pointed out by Shaver et al. [288], a 40% change in the electron temperature can change the estimated abundances by an order of magnitude. In the optical band the electron temperature is usually obtained by measuring the intensities of $[O_{III}]$ 4353 or $[N_{II}]$ 5755, both very weak lines which are detectable only in relatively hot ($\geq$ 7000 K) and bright HII regions. The number of HII regions for which reliable abundances can be obtained is therefore severely limited. However in our Galaxy, electron temperatures can also be determined from radio recombination line data and this method allows us to achieve accuracies of a few percent (Shaver [286]). Moreover, recombination lines can be detected for a large number of sources thus widely complementing the optical estimates. A useful relation for computing the electron temperature, T_e, is:

$$\frac{\Delta V}{T_L} T_C = \frac{1.908 \times 10^4 \nu e^{\chi_n} N_+/N_e}{T_e[1.5 \ln T_e - \ln(20.18\nu)]} km sec^{-1} K^{-1} \tag{4.5}$$

(Shaver et al. [288]). In this expression, ΔV is the linewidth to half intensity in km sec^{-1}; T_L the line temperature in K; T_C the temperature of the underlying continuum in K; $\chi_n = 1.58{\times}10^5/n^2T_e$ in K^{-1} ; N_+ the number density of hydrogen ions[5]. Eq. (4.5) shows that, also at radio wavelengths, estimates of electron temperatures are not trivial, although less complicated than in the optical band, due to the fact that they require simultaneous accurate measurements of the line and of the continuum.

Electron temperatures are available for 404 of the 575 sources in our catalog with more reliable estimates of R, (Caswell & Haynes [53]; Downes et al. [94]; Reifenstein et al. [252]; Wilson et al. [343]; Wink et al. [346], [347]). We are then in a position to investigate the dependence of HII region electron temperatures upon Galactocentric distance. Such gradient is thought to be causally related to the abundance gradient, as oxygen is one of the principal coolants in HII regions. Non-LTE effects should be small over the entire range of frequencies 5 to 22 GHz (Shaver et al. [288]; Wink et al. [347]),

---

[5] The term N_+/N_e accounts for the helium abundance.

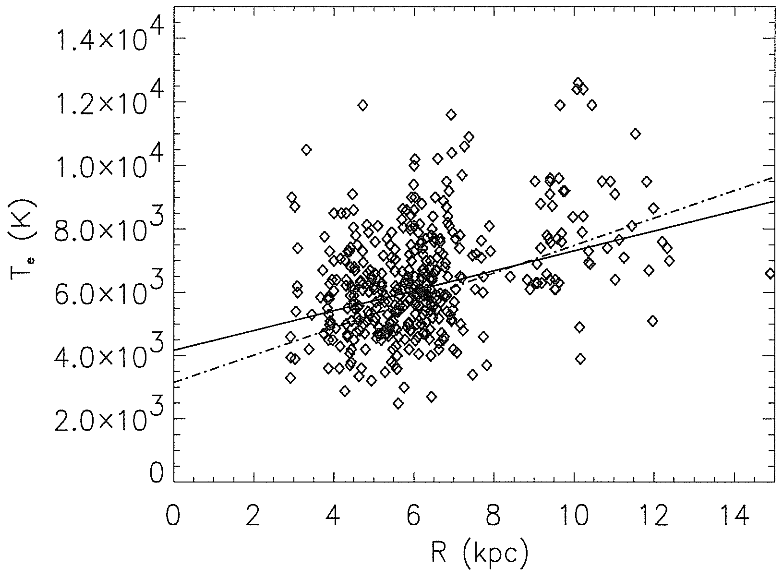

Figure 4.7: Electron temperatures versus galactocentric distance. The solid line shows our least-squares linear relationship, the dot-dashed line that found by Shaver et al. [288].

so that corrections to the computed T_e values are not necessary. When two or more values of T_e are available for the same source, their weighted average has been taken. The data shown in Fig. 4.7 confirm the previously reported correlation between T_e and R, based on much smaller samples (Churchwell et al. [57]; Downes et al. [94]; Shaver et al. [288]). The least-square linear relationship is:

$$T_e = (4166 \pm 124) + (314 \pm 20)R \text{ K} \tag{4.6}$$

close to the previous result by Shaver et al. [288] who found $T_e = (3150 \pm 110) + (433 \pm 40)R$ K.

Shaver et al. [288] have shown that the electron temperature gradient is a function of both the effective temperature, T_{eff}, and the electron density, n_e. Such a dependence could explain much of the observed scatter.

4.4 Distances from the Sun

The galactocentric radius R is related to the distance D from the Sun by the equation:

$$R = (R_0^2 + D^2 - 2DR_0 \cos l)^{\frac{1}{2}} \ , \tag{4.7}$$

which has obviously, in general, two real solutions for D if $R \leq R_0$:

$$D_{far/near} = R_0(\cos l \pm (\cos l^2 - (1 - (R/R_0)^2))^{\frac{1}{2}}) \tag{4.8}$$

corresponding to the two intersections of the line-of-sight with the orbit of radius R. The solution is unique only for sources lying outside the solar circle or whose line-of-sight is tangent to their orbit.

To break the degeneracy we need auxiliary data. Two kinds of data have been used: absorption lines and optical counterparts. Since only neutral (HI) or molecular (H_2CO and OH) gas in front of an HII region can absorb its continuum emission, if the region is at the "near" distance the gas absorption line velocity is lower than its recombination line velocity. On the other hand, if the HII region is at the "far" distance it is possible to detect absorption at a velocity higher than that of its recombination line. At the same time, if an optical counterpart is detected, then it is very likely that the HII region is at the "near" distance since the heavy dust obscuration at optical wavelengths makes detections of far sources quite difficult.

Tables 4.2, 4.3 and 4.4 list the sources for which the ambiguity can be resolved using auxiliary data. HI data are mainly taken from Kuchar & Bania [187] and Caswell et al. [52]. Additional data are taken from Kerr & Knapp [180] and Goss & Radhakrishnan [131]. H_2CO data are from Wilson [345]. Optical identifications are from the catalogs by Marsálková [208], Blitz et al. [24], and Brand & Blitz [28]. Complementary data on individual sources are from Miller [222] and Shaver et al. [287].

Of our 575 sources with $|V_r| \geq 10\,\mathrm{km\,s^{-1}}$, 117 have a unique solution for D (84 lie outside the solar circle and for 33 the line of sight is tangent to their galactocentric orbit); for 177 others we have additional data allowing us to discriminate between the two solutions; 281 are left with the distance degeneracy. For the latter, we need an additional distance indicator.

4.4.1 The luminosity-physical diameter correlation

A rough proportionality between luminosity and linear diameter is expected based on the following argument. The luminosity is proportional to the product of the emission measure (which is proportional to the linear diameter) with the square of the angular size. But, for our sample, the distribution of angular sizes has a dispersion of only $6'$ which is small enough not to swamp the correlation with the emission measure.

In order to verify the correlation, we have selected from the catalog presented in Chapter 3 the HII regions with flux densities, S_ν, and angular diameters, θ, measured with the same instrument as well as with an unambiguous determination of the distance, D, from the Sun. We have 57 such sources with measurements at 2.7 GHz and 190 with measurements at 5 GHz. At both frequencies we find a highly significant correlation between the luminosity $L_\nu = 4\pi D^2 S_\nu$ and linear diameter (see Fig. 4.8). The Pearson correlation coefficients are 0.54 (corresponding to a probability $p \simeq 10^{-5}$ that the correlation is occurring by chance) at 2.7 GHz, and 0.56 ($p \simeq 10^{-17}$) at 5 GHz.

On the other hand, we should worry about the possibility that the correlation is an artifact arising through the dependence of luminosity on D^2 while the linear diameter

Table 4.2: Galactic HII regions for which the distance ambiguity was resolved using auxiliary data. The (*o*) denotes HII regions with an optical counterpart, for which the "near" solution was chosen; (*a*1) and (*a*2) denote sources for which, respectively, HI or H_2CO absorption data are available.

l	b	*Near or Far kinematic distance*		l	b	*Near or Far kinematic distance*	
6.4	-0.5	near	(o)	19.1	-0.3	near	(a2)
6.5	0.1	near	(a1)	19.6	-0.2	near	(a2)
6.6	-0.3	near	(o)	19.6	-0.1	near	(a2)
6.6	-0.1	near	(a1)	19.7	-0.1	near	(a2)
6.7	-0.2	near	(a1)	21.0	0.1	far	(a2)
7.0	-0.2	near	(o)	21.9	0.0	near	(o)
8.4	-0.3	near	(a2)	22.8	-0.5	far	(a2)
8.7	-0.4	near	(o)	22.9	-0.3	far	(a2)
10.5	0.0	near	(a2)	22.9	0.7	near	(o)
11.7	-1.7	near	(o)	23.0	-0.4	far	(a2)
12.4	-1.1	near	(o)	23.1	0.6	near	(o)
13.4	0.1	far	(a2)	23.4	-0.2	tangent	(a2)
14.0	-0.1	near	(a2)	23.5	-0.0	far	(a2)
14.2	-0.2	near	(o)	23.7	0.2	tangent	(a2)
14.2	-0.1	near	(o)	23.9	-0.1	far	(a2)
14.4	-0.7	near	(a2)	24.0	0.2	far	(a2)
14.6	0.0	near	(o)	24.2	-0.1	far	(a2)
14.6	0.1	near	(a2)	24.4	0.1	tangent	(a2)
15.0	-0.7	near	(o)	24.5	0.2	tangent	(a2)
15.1	-0.9	near	(o)	24.5	0.5	tangent	(a2)
15.1	-0.7	near	(o)	24.7	-0.2	tangent	(a2)
15.2	-0.8	near	(a2)	24.7	-0.1	near	(o)
15.2	-0.6	near	(a2)	24.8	0.1	tangent	(a1)
16.6	-0.3	near	(o)	25.3	0.3	near	(o)
16.9	0.8	near	(o)	25.4	-0.3	far	(a2)
17.0	0.8	near	(o)	25.4	-0.2	far	(a2)
17.0	0.9	near	(a2)	25.7	0.0	far	(a2)
18.1	-0.3	near	(a2)	25.8	0.2	tangent	(a2)
18.2	-0.3	near	(o)	26.1	-0.1	far	(a2)
18.2	-0.4	near	(a2)	27.3	0.1	far	(a2)
18.3	-0.4	near	(a2)	27.5	0.2	far	(a2)
18.3	-0.3	near	(a2)	28.6	0.0	far	(a2)
18.3	1.9	near	(a2)	28.7	0.0	far	(a2)
18.7	2.0	near	(o)	28.8	0.2	tangent	(a2)
18.9	-0.4	near	(o)	29.0	-0.6	near	(o)
18.9	-0.5	near	(a2)	29.1	-0.7	near	(o)
19.0	-0.0	near	(a2)	29.9	-0.0	far	(a2)

Table 4.3: Galactic HII regions for which the distance ambiguity was resolved using auxiliary data. The (*o*) denotes HII regions with an optical counterpart, for which the "near" solution was chosen; (*a*1) and (*a*2) denote sources for which, respectively, HI or H_2CO absorption data are available.

l	*b*	*Near or Far kinematic distance*		*l*	*b*	*Near or Far kinematic distance*	
30.2	-0.1	far	(a2)	39.9	-1.3	near	(o)
30.5	0.0	near	(o)	40.5	2.5	near	(o)
30.5	0.4	near	(o)	41.1	-0.2	far	(a1)
30.6	-0.1	tangent	(a1)	41.2	0.4	near	(a1)
30.7	-0.3	tangent	(a2)	41.5	0.0	far	(a1)
30.8	-0.0	near	(a1)	42.1	-0.6	near	(a1)
31.0	0.0	far	(a1)	42.4	-0.3	far	(a1)
31.2	-0.1	far	(a1)	42.6	-0.1	near	(a1)
31.3	0.1	tangent	(a1)	43.9	-0.8	far	(a1)
31.4	-0.3	near	(a2)	44.3	0.1	near	(a1)
31.4	0.3	tangent	(a2)	45.1	0.1	far	(a1)
31.6	0.1	near	(a1)	45.5	0.1	far	(a1)
31.8	1.5	near	(o)	46.5	-0.2	near	(a1)
32.2	0.1	far	(a1)	48.6	0.0	far	(a1)
32.8	0.2	far	(a1)	48.6	0.2	far	(a1)
33.1	-0.1	tangent	(a1)	49.4	-0.2	far	(a1)
33.4	-0.0	far	(a1)	51.1	0.2	far	(a1)
34.3	0.1	near	(a1)	52.8	0.3	far	(a1)
34.9	-0.0	near	(a1)	53.6	0.0	near	(o)
35.1	-1.5	near	(a2)	53.6	0.2	far	(a1)
35.2	-1.8	near	(a2)	60.9	-0.1	near	(o)
35.3	-1.8	near	(a2)	62.9	0.1	near	(o)
35.6	-0.5	near	(a1)	63.2	0.4	near	(o)
35.6	-0.0	far	(a1)	63.2	0.5	near	(o)
35.6	0.1	far	(a1)	302.8	1.3	near	(o)
35.7	-0.0	near	(a2)	305.4	0.2	far	(a1)
36.3	-1.7	near	(o)	308.7	0.6	near	(o)
36.5	-0.2	far	(a1)	311.0	0.4	near	(o)
37.4	-0.2	far	(a2)	311.9	0.1	far	(a1)
37.4	-0.1	far	(a1)	311.9	0.2	far	(a1)
37.4	-0.0	far	(a1)	316.8	-0.1	near	(o)
37.5	-0.1	far	(a1)	316.8	-0.0	near	(o)
37.6	-0.1	far	(a1)	317.0	0.3	far	(1a)
37.7	-0.1	far	(a1)	320.2	0.8	near	(o)
37.8	-0.2	far	(a1)	321.1	-0.5	near	(o)
37.9	-0.4	far	(a1)	322.2	0.6	near	(a1)
38.1	-0.0	far	(a1)	324.2	0.1	near	(o)

Table 4.4: Galactic HII regions for which the distance ambiguity was resolved using auxiliary data. The (*o*) denotes HII regions with an optical counterpart, for which the "near" solution was chosen; (*a*1) and (*a*2) denote sources for which, respectively, HI or H_2CO absorption data are available.

l	*b*	*Near or Far kinematic distance*		*l*	*b*	*Near or Far kinematic distance*	
326.6	0.6	near	(a1)	333.6	-0.2	near	(a1)
326.7	0.6	near	(o)	336.4	-0.2	near	(o)
327.3	-0.6	near	(a1)	336.5	-1.5	near	(a1)
327.3	-0.5	near	(o)	336.8	0.0	far	(a1)
328.0	-0.1	near	(o)	337.1	-0.2	far	(a1)
328.3	0.4	far	(a1)	337.9	-0.5	near	(a1)
328.6	-0.5	near	(o)	338.9	0.6	near	(a1)
330.9	-0.4	near	(a1)	340.8	-1.0	near	(a1)
331.3	-0.3	near	(a1)	345.4	-0.9	near	(a1)
331.5	-0.1	far	(a1)	345.4	1.4	near	(a1)
332.8	-1.4	near	(o)	348.2	-1.0	near	(o)
332.8	-0.6	near	(o)	348.7	-1.0	near	(o)
333.0	-0.4	far	(a1)	350.5	1.0	near	(o)
333.1	-0.4	near	(o)	351.6	-1.3	near	(o)
333.3	-0.4	near	(o)				

Table 4.5: Fractions of near (N), far (F), and tangent (T) solutions resulting from absorption data. The last column shows the number of sources of the catalog whose distance ambiguity is resolved through listed HI absorption data.

		N (%)	F (%)	T (%)	N
HI	Kuchar & Bania [187]	20	72	8	40
	Caswell et al. [52]	67	28	5	18
	Kerr & Knapp [180]	55	45	-	9
H_2CO	Wilson [345]	44	37	19	84

is proportional to D. To check if this can be the case, we have computed the partial correlation coefficient between the two quantities, i.e. the correlation at constant D. For the combined sample of 190 + 57 sources (extrapolating to 5 GHz the 2.7 GHz fluxes with a spectral index of -0.1, $S \propto \nu^{-0.1}$, as appropriate for optically thin free-free emission) we find a partial correlation coefficient of 0.37 for which $p \simeq 10^{-8}$. The correlation is therefore clearly physically significant. This issue will be further discussed in section 4.5. Assuming a linear relationship between $\log L_\nu$ (in erg/s) and $\log d$ (in pc):

$$\log\ L_\nu = a + b \times \log\ d \tag{4.9}$$

a least square fit yields $a = 31.9$, $b = 1.05$ at 2.7 GHz and $a = 32.4$, $b = 0.86$ at 5 GHz. Combining the two samples, we obtain $a = 32.1$, $b = 0.88$ at 5 GHz.

The solar distance D can then be estimated as:

$$D = 10^{\frac{a}{2-b}} \left(\frac{\theta}{1''}\right)^{\frac{b}{2-b}} \left(\frac{\nu}{1GHz}\right)^{\frac{-1}{2-b}} \left(\frac{S}{1Jy}\right)^{\frac{-1}{2-b}} \text{kpc} \tag{4.10}$$

Although the dispersion around the above relationship is too large to make it a good distance indicator for individual sources, it allows us to discriminate in a statistical sense among the "near" and "far" solutions. To test the reliability of this approach we have applied it to the 177 sources for which the distance degeneracy has been broken using complementary data. We find that the fractions of "near" ($\simeq$ 65%) and "far" ($\simeq$ 35%) distances are correctly reproduced although the correct distance is assigned to only $\simeq$ 60% of individual sources.

We have homogeneous measurements of flux densities and of angular diameters at either 2.7 or 5 GHz for 256 out of the 281 HII regions with distance degeneracy. To these sources we apply eq. (4.10). We find that 100 ($\sim$ 40%) objects are assigned to the "near" solution and 155 ($\sim$ 60%) to the "far" solution.

To cross-check our result we consider the distribution of the 256 sources in the $\log L_\nu$–$\log d$ plane, assuming that they are either at the "near" or at the "far" distance (see Fig. 4.9). There is a better fit to the luminosity - diameter relation of eq. (4.10) for the "far" solution. However, the spread is greater than in Fig. 4.8, suggesting that there is a mix of near and far distances, with the majority being at the "far" distance.

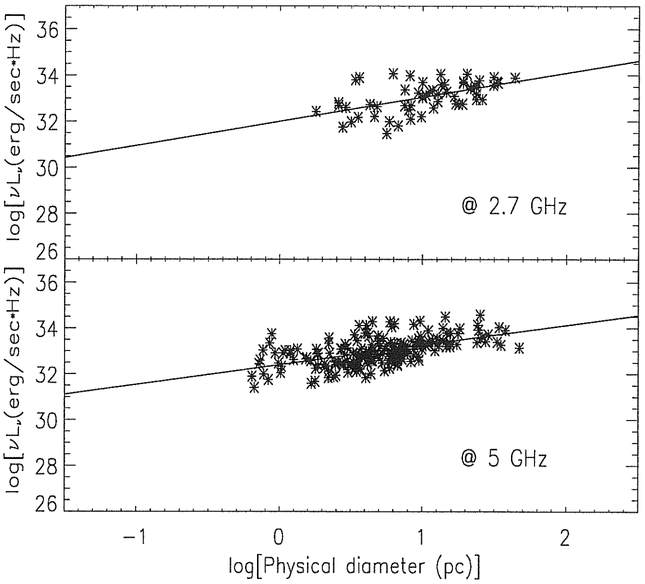

Figure 4.8: Luminosity-physical diameter correlation at 2.7 (57 sources) and 5 GHz (190 sources) for HII regions with unambiguous distances.

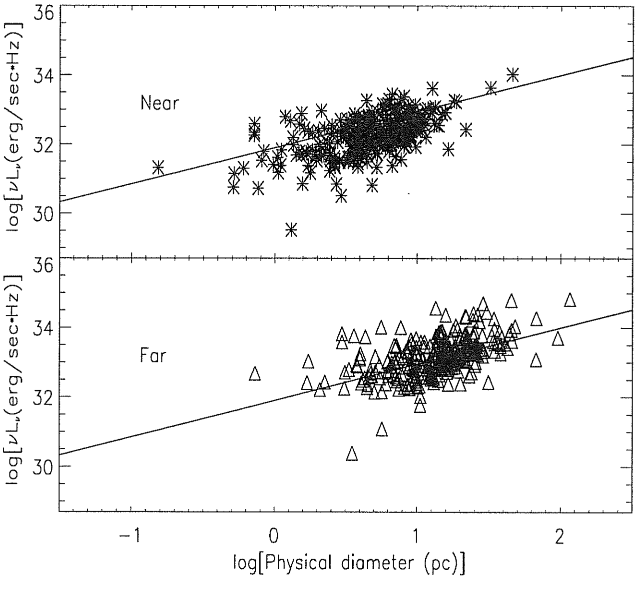

Figure 4.9: Luminosity-physical diameter best-fit derived for unique distance plus auxiliary data sources (solid line) overlaid on the luminosity-physical diameter distribution obtained assuming *near* (upper panel) or *far* solutions (bottom panel).

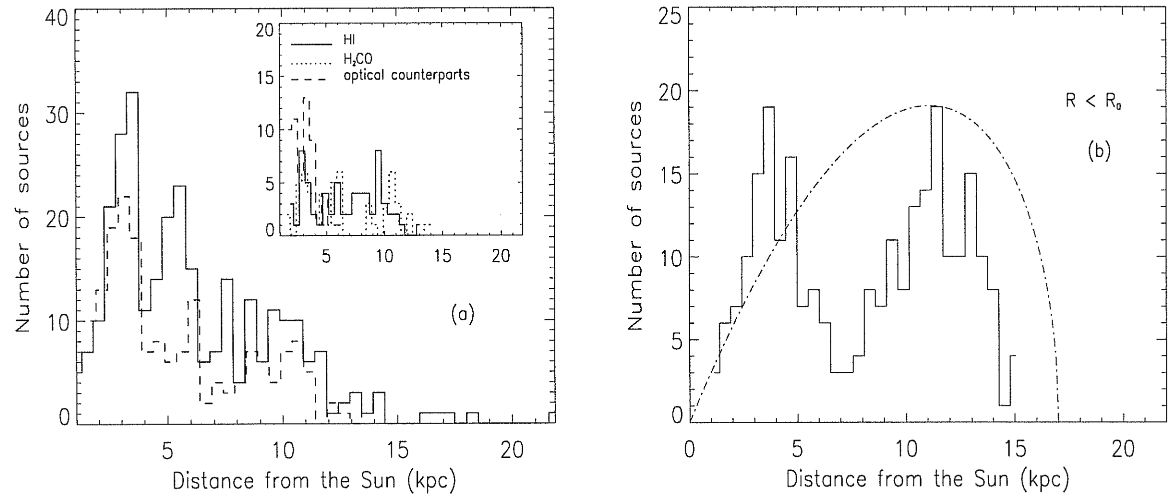

Figure 4.10: Distributions of solar distances for HII regions. The Panel (a) shows the distribution of all 294 sources with unambiguous distance estimates (solid histogram) and of the subset of 177 sources whose near/far degeneracy was broken by complementary data (dashed). The insert details the distributions of the various kinds of complementary data. Panel (b) shows the distribution of 256 sources with near/far degeneracy resolved using the luminosity-diameter relationship; the dashed line shows the expected shape in the case of a uniform distribution of HII regions in the solar circle.

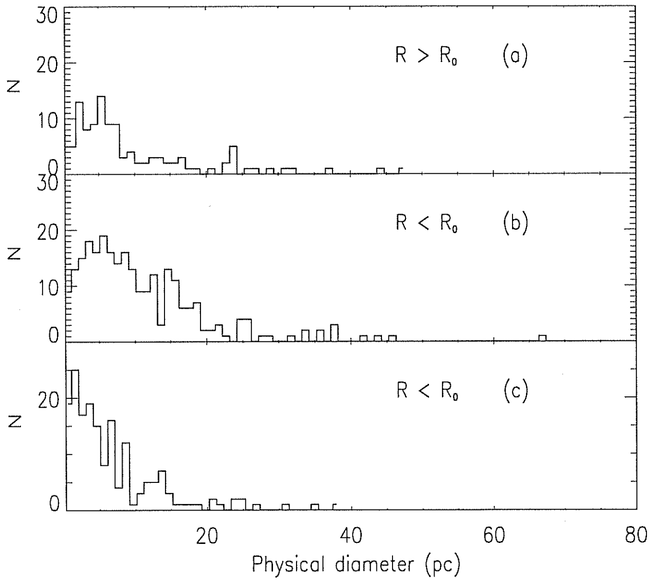

Figure 4.11: Distributions of linear diameters. Panel (a): 117 sources with unique solutions for solar distances; panel (b): 256 sources with near/far degeneracy resolved using the luminosity-diameter relationship; panel (c): 177 sources with near/far degeneracy resolved using auxiliary data.

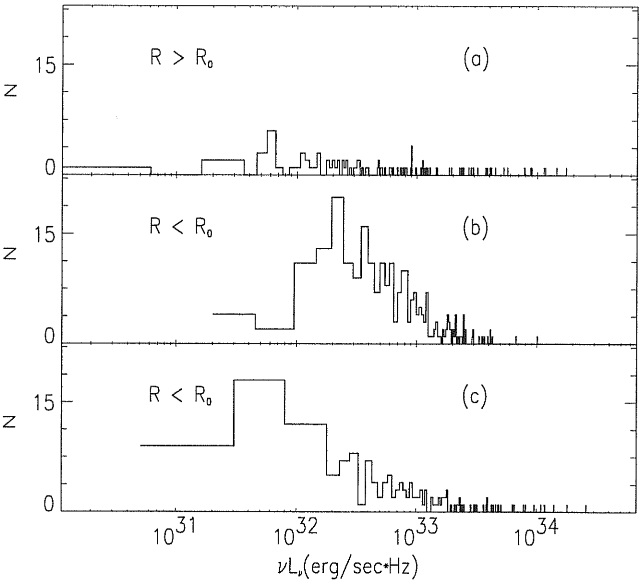

Figure 4.12: Distributions of 2.7 GHz luminosities. Panel (a): 117 sources with unique solutions for solar distances; panel (b): 256 sources with near/far degeneracy resolved using the luminosity-diameter relationship; panel (c): 177 sources with near/far degeneracy resolved using auxiliary data.

4.4.2 Distance degeneracy and properties of the sample

We will now consider the implications of breaking the distance ambiguity on the properties of the HII regions lying within the solar circle ($R < R_0$). The considerations will include the distributions of radial distance from the Sun, the physical diameter and the source luminosity.

The distribution of distances from the Sun from different samples with unambiguous distances are shown in Fig. 4.10(a). The dashed line is for the 177 sources with $R < R_0$ whose distance ambiguity has been resolved using the complementary data plotted in the insert. The full line is the sum of these 177 sources plus the 117 sources at $R > R_0$ with unambiguous kinematic distances.

Fig. 4.10(b) shows the distributions of sources whose near/far degeneracy has been resolved using the luminosity-diameter relationship. It can be seen that the number of sources reaches a first peak at 3-5 kpc from the Sun followed by a minimum at 6-9 kpc and a second peak at 10-14 kpc. The minimum corresponds to distances from the Sun which include the Galactic centre region where there is a deficit of detected sources.

As a further check, we consider the extreme case of a uniform distribution of HII regions in the galactic plane. Under this assumption, the expected number N of sources in the region of the Galactic plane at a distance $D \pm \Delta D$ from the sun is given by $N(D) = K \times (\theta \cdot D \cdot \Delta D)$, where θ=arcos($D/2R_0$) is the angle subtended by the portion of the Galactic at distance $D \pm \Delta D$ from the sun, and K is the uniform density of HII

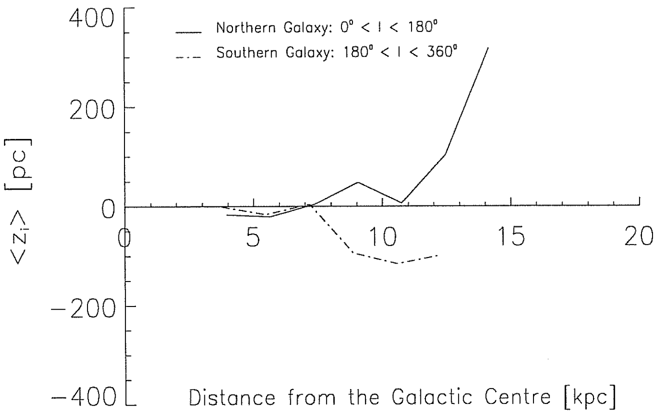

Figure 4.13: Variation of bin-averaged z with distance from the Galactic centre, R.

regions. According to this calculation the distribution has a peak at 12-14 kpc from the Sun. We conclude that the distribution in Fig. 4.10(b) is an acceptable fit to expectation, but with a small deficit of more distant sources. This deficit is expected given the incompleteness of the catalog at faint fluxes (see Fig. 3.6 in Chapter 3). Application of eq. (4.10) would appear to have been successful.
The distribution of sources in Fig. 4.10(a) with $R < R_0$ (dashed line) shows a strong deficit in the range 12-14 kpc compared with Fig. 4.10(b). There are a number of contributing factors. Those sources with optical counterparts are preferentially nearby because of obscuration at larger distances. In addition, it is more difficult to measure accurate absorption spectra for sources at lower flux densities; these will again be preferentially at larger distances. Table 4.5 illustrates this situation. The deeper survey by Kuchar & Bania [187] shows a near to far number ratio 20:72; this may be compared with the expected ratio 25:75 for a uniform distribution in the Galactic plane. The less deep survey by Caswell et al. [52], Kerr & Knapp [180] and Wilson [345] have a majority of sources at the near distance.

We now turn to the distribution of linear diameters deduced from the application of our technique of resolving the distance ambiguity. Low diameter sources are somewhat under-represented in Fig. 4.11(b), since objects in this sample are on average at greater distances as seen in Fig. 4.10(b). Fig. 4.12 shows the 2.7 GHz luminosity distribution for the same three samples of sources as in Fig. 4.11. The 256 sources (Fig. 4.12(b)) whose distance ambiguity is broken by the use of eq. (4.10) have higher intrinsic luminosities than the other two samples. Again this is because of their greater average distances for similar flux density and angular size distributions.

4.4.3 The z-distribution of Galactic HII regions

We take all 550 HII regions with distance determinations and estimate their z distances from the Galactic plane using the expression:

$$z = (D \times sin(b)) \times 10^3 \tag{4.11}$$

where z is in pc, and the distance D from the Sun is in kpc. For the Northern (quadrants I and II; $0^0 \leq l \leq 180^0$) and the Southern (quadrants III and IV; $180^0 \leq l \leq 360^0$) Galaxy, we have binned the galactocentric distances, R, into annuli $0.2R_0$ wide. Fig. 4.13 shows the mean of the z-distribution, $< z_i >$, where i is the index of the bin. The increasing $< z_i >$ with R in quadrants I and II and a corresponding decrease in quadrants III and IV clearly show the warp[6] of the Galactic plane well known from HI and CO studies (see, for example, Burton [49]), although of in the case of HII regions it has a smaller magnitude.

In order to investigate the thickening of the HII region layer with R, we have also computed, for each bin, the width σ_i of the z-distribution:

$$\sigma_i = \left[\sum_{j=1}^{N}(z_j - < z_i >)^2\right]^{\frac{1}{2}} \tag{4.12}$$

where N is the number of sources in the i-bin (see Table 4.6). The uncertainty on σ is dominated by the sampling error, that we have estimated following Danese et al. [76], on the assumption of an underlying Gaussian distribution. The result is illustrated in Fig. 4.14 for all 550 sources with distances and shows that on both sides of the Galaxy, the HII region layer thickens with increasing R. A similar effect is found for the distribution of OB stars by Bronfman et al. [41] and for the distribution of molecular gas, based on the data from Cohen et al. [61], Grabelsky et al. [136], May et al. [213] and Digel [89], as reported in Bronfman et al. [41].

For $R < R_0$, the width of the z-distribution (Fig. 4.14) is almost constant. Table 4.7 gives the azimuthally averaged values of σ for the combined Northern and Southern data sets. The best-determined distances give $\sigma \simeq 39.3\,\text{pc}$; when the data for HII regions with distances relying on eq. (4.10) are included, $\sigma \simeq 52\,\text{pc}$. These values are similar to the values $\sigma = 32\,\text{pc}$ derived for dust-embedded OB stars (Bronfman et al. [41]) and $\sigma = 51\,\text{pc}$ for the H_2 layer (Bronfman et al. [40]). The HI (Malhotra [205]; Binney & Merrifield [20]) layer is wider by a factor of about 2. Pulsar dispersion measures indicate a thin disk of ionized hydrogen with $\sigma = 70$ pc (Reynolds [260]).

The negative mean value of z, $< z >$, is consistent with the well known result that the sun lies above the plane: Reed [247] finds $z_\odot = 10$–12 pc by analyzing the distribution of 12,522 OB stars.

---

[6] See section 1.2.2 in Chapter 1.

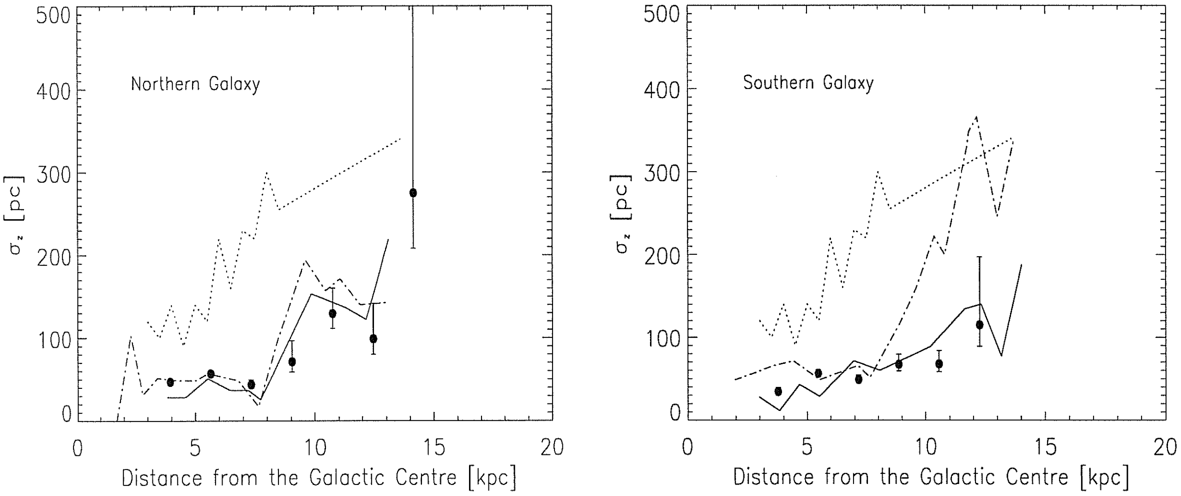

Figure 4.14: Azimuthally-averaged thickness in the Northern ($0^0 \leq l \leq 180^0$) and Southern ($180^0 \leq l \leq 360^0$) Galaxy (filled circles). Also shown for comparison are the UCHII layer (solid line), the H_2 layer (dashed line) (both from Bronfman et al. [41]) and the HI layer (dotted line). Data are from Malhotra [205] for $R < R_0$ and from Binney & Merrifield [20] for $R > R_0$.

Table 4.6: Azymuthally-averaged σ_z for the Northern and the Southern hemisphere with sampling errors, under the assumption of an underlying Gaussian distribution. Centroids of the bins (R_{bin}) and number of sources per bin (N) are also shown.

	Northern		Southern	
R_{bin} (kpc)	N	σ_z (pc)	N	σ_z (pc)
3.9	103	$47^{+3.67}_{-2.97}$	36	$34.3^{+4.9}_{-3.5}$
5.6	124	$56.9^{+4}_{3.3}$	96	$56.2^{+4.6}_{-3.7}$
7.3	41	$43.6^{+5.9}_{4.2}$	57	$48.8^{+5.3}_{-4.0}$
9.0	10	$71.2^{+25.5}_{-12.2}$	24	$67.1^{+12.3}_{-7.9}$
10.7	19	$129.3^{+30.8}_{-17.9}$	15	$67.6^{+16.1}_{-9.4}$
12.4	8	$98.7^{+43}_{-18.5}$	5	$114.7^{+82.5}_{-25.7}$
14.1	4	275^{+270}_{-66}	-	-

Table 4.7: Width σ and mean, $< z >$, of the z-distribution within the solar circle. The results in the first column use sources with unique solutions (u) plus sources whose distance degeneracy was resolved with auxiliary data (aux) or with the luminosity-diameter correlation (assig). In the second column, the last group (assig) of sources is not included.

σ (pc) u+aux+assig	σ (pc) u+aux	$< z >$ (pc)
52	-	-11.3
-	39.3	-7.3

4.5 Conclusions

We have analyzed the spatial distribution of 550 Galactic HII regions taken from the 2.7 GHz catalog presented in Chapter 3, exploiting the extensive database of kinematic information included in the catalog. For each source we have derived a galactocentric distance using the FBS89 rotation model.

Distances from the Sun could be unambiguously derived for 117 sources, lying either outside the solar circle (84) or on a line-of-sight tangential to their orbit (33). A highly significant correlation between luminosity and linear diameter was found for these sources. The corresponding least-square linear relationship in the log-log plane was used to resolve, at least in a statistical sense, the distance ambiguity for an additional 256 sources. The reliability of this approach was successfully tested comparing the distributions of solar distances, linear diameters and luminosities so obtained with those of sources with unambiguous distances.

An analysis of the z-distribution of HII regions shows:

1. an increase of the mean value of $|z|$ with R, for $R > R_0$, reflecting the shape of the warp;
2. a corresponding increase of the width of the distribution as a function of R, comparable to what is seen for the OB stars (Bronfman et al. [41]) and the molecular gas distribution (Cohen et al. [61]; Grabelsky et al. [136]; May et al. [213]; Digel [89]);
3. an azimuthally-averaged thickness of the HII region layer within the solar circle similar to that of OB stars (Bronfman et al. [41]) but narrower than those of the diffuse HII and HI (Reynolds [260]).

To check to what extent the above results depend on the adopted linear diameter–luminosity correlation, we have repeated the analysis adopting the extreme assumption that the two quantities are totally independent. In this case we have used the mean linear diameter ($\overline{d} = 7.6\,\mathrm{pc}$) of sources with known solar distance as a distance indicator.

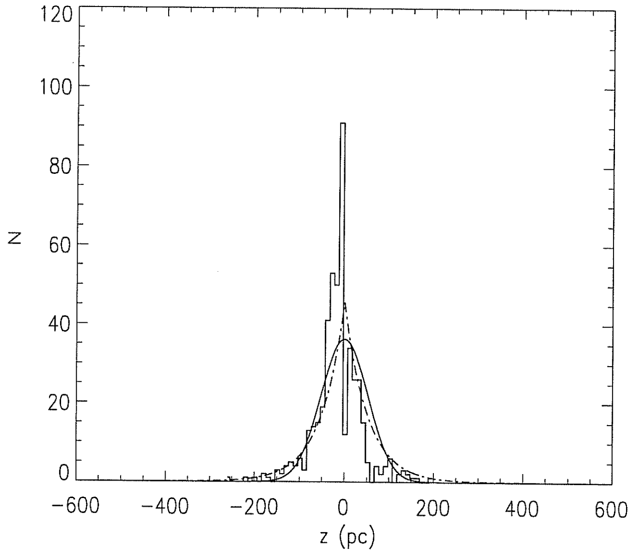

Figure 4.15: z-distribution of the 456 sources at $R < R_0$ whose solar distance is either unambiguous or assigned through the luminosity-diameter correlation. Overlaid are a gaussian (solid line) and exponential curve (dashed line) with σ taken equal to 52 pc (see Table 4.7) and normalized to the number of plotted sources.

The results for $R > R_0$ (and, in particular, the increase of $| < z > |$ and the thickening of the z-width with increasing R) are obviously unchanged since objects outside the solar circle are unaffected by the distance degeneracy. For $R < R_0$ we find $\sigma = 51.4\,\mathrm{pc}$, $< z >= -7.2\,\mathrm{pc}$, not significantly different from the values found using the correlation (see Table 4.7).

Also, we confirm, for a much larger sample, the positive gradient of electron temperature with galactocentric distance discovered in previously published works.

The 2-D distribution within the Galactic plane of HII regions having distances determined in the present study is shown in Fig. 4.16. The HII regions show spiral-like structures, in acceptable agreement with the spiral arms delineated by the TC93 model. This fact is partly expected due to the fact that the skeleton model of the arm shapes in TC93 is derived from the map published in Georgelin & Georgelin [125], built on the basis of velocity data from Reifenstein et al. [252] and Wilson et al. [343]) complemented by the information contained in Downes et al. [94] and Caswell & Haynes [53] (see section 4.2). However, our analysis exploits data not available for the TC93 analysis (see Table 4.1) and makes use of a different rotation curve. From this point of view, the agreement with the TC93 model is not a trivial result. A more detailed study of the spiral arm structure is beyond the goal of this work and represents one of the future developments of the current analysis.

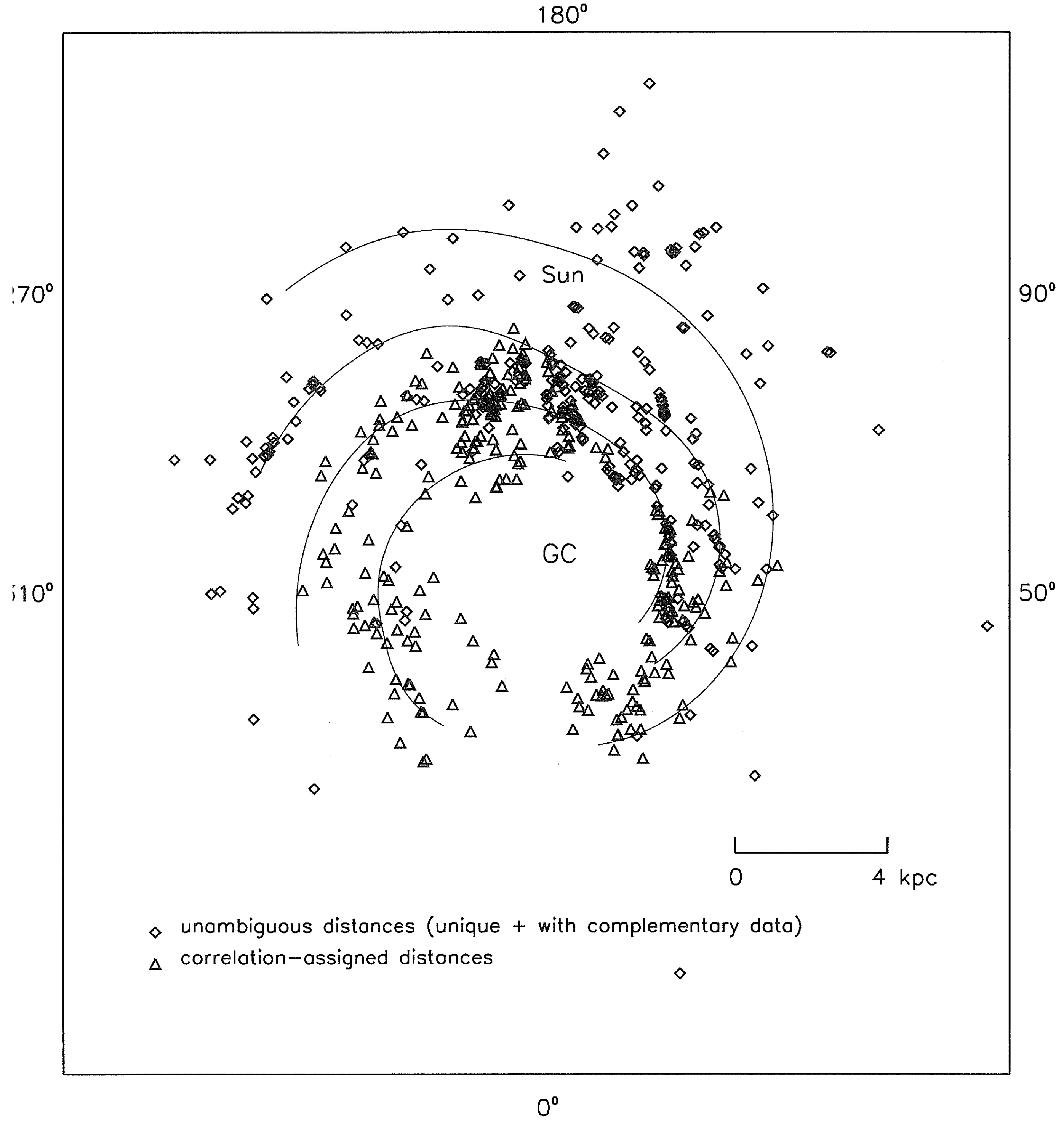

Figure 4.16: 2-D distribution of 550 HII regions from the catalog presented in Chapter 3. The diamonds correspond to the 117 sources for which there is no distance ambiguity, plus the 177 sources for which the distance degeneracy was resolved thanks to auxiliary data. The triangles correspond to the 256 sources to which the luminosity-diameter correlation was applied. Also shown is the spiral arm model by Taylor & Cordes [311]. An updated version of this model is given in Cordes & Lazio [67], [68].

Chapter 5

Applications of the HII region catalog

5.1 Introduction

We have described in Chapter 3 the construction of an extensive data base of radio observations of HII regions which has been distilled into the Synthetic Catalog of 1442 objects at a frequency of 2.7 GHz. We consider some uses of this catalog and of the associated Master Catalog for CMB studies as well as for studies of individual HII regions and, more in general, of the Galactic emission. The chapter is organized as follows: section 5.2 shows that HII regions are easily detectable by instruments devoted to CMB observations therefore contributing significantly to the foreground signal. Section 5.3 discusses the reasons for considering HII regions in the process of instrumental calibration. Section 5.4 deals with the role played by HII regions for pointing and beam-shape reconstruction. In section 5.5, we analyze the straylight effect produced by the overall distribution of Galactic HII regions. In section 5.6, we describe the use of the catalog in view of observations of HII regions in the poorly explored, yet scientifically relevant, millimetric spectral region while, in section 5.7, we discuss how, by taking into account the thermal emission from HII regions, it is possible to explain the lack of a clear correlation between total intensity and polarized emission from the Galactic plane. Finally, in section 5.8 we summarize the main conclusions of the chapter.

5.2 Detectability of HII regions

The rms noise in Jansky per second of integration, $rms_{1s,f}$, is related to the rms antenna temperature in Kelvin degrees per second of integration, $rms_{1s,a}$, by:

$$(rms_{1s,f}/\mathrm{Jy}) = 2.95 \times 10^{-3} (\mathrm{FWHM/arcmin})^2 \cdot (\nu/\mathrm{GHz})^2 (rms_{1s,a}/\mathrm{K}) \qquad (5.1)$$

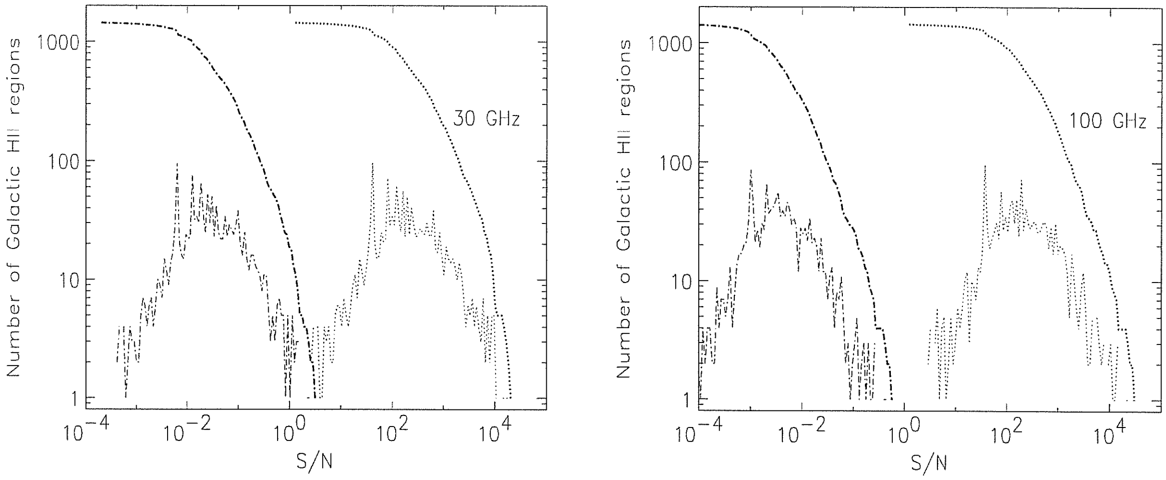

Figure 5.1: Differential (bottom curves) and cumulative distributions (upper curves) of S/N ratios of HII regions in the Synthetic Catalog at 30 and 100 GHz for PLANCK (dotted lines) and *COBE*-DMR (dash-dot lines). The S/N binsize for the differential distribution is of order of ~ 0.05. The *COBE*-DMR angular resolution is 7° at both frequencies. PLANCK has a nominal FWHM of ~ 33.6′ at 30 GHz and 10′ at 100 GHz.

where FWHM is the full-width at half maximum of the instrument beam and ν is the frequency. More generally, this expression relates the flux density to its antenna temperature of a point-like source on the axis of a Gaussian, symmetric beam.

Eq. (5.1) can be then used to determine the S/N ratio for a point source of a given flux density. Appropriate correction factors need to be applied if the source is extended. For example, in the case of an extended source with uniform surface brightness, the S/N ratio is ~ 40 to 90 % of the value computed with Eq. (5.1) if its diameter is ~ 2 − 3 times the beamwidth or ~ 1/2 − 1/3 the beamwidth, respectively. The S/N ratio represents an easy way to compare the signal produced by Galactic HII regions with the sensitivity of a typical CMB anisotropy experiment. Therefore, we have performed this calculation in the case of the high resolution satellite experiment PLANCK by ESA [1], scheduled for launch in 2007. PLANCK will observe the entire sky with a sensitivity at the end of the mission of about 10 μK per resolution element. The beamwidths vary between ~ 33.6′ and 5′ from 30 to 857 GHz respectively. For numerical estimates, we consider here the channels at 30 and 100 GHz which have a nominal FWHM of ~ 33.6′ and 10′. For comparison, we make the same calculation for *COBE*-DMR for which, at 31.5 and 90 GHz the rms temperature was 150 and 100 μK and the beamwidth was 7° (Boggess et al. [26]).

The S/N for all the HII regions in the Synthetic Catalog have been calculated as discussed above. The flux densities were estimated at each frequency extrapolating the values at 2.7 GHz with a spectral index of 0.1 ($S_\nu \propto \nu^{-0.1}$). Fig. 5.1 shows the number of sources per

---

[1] http://planck.esa.nl

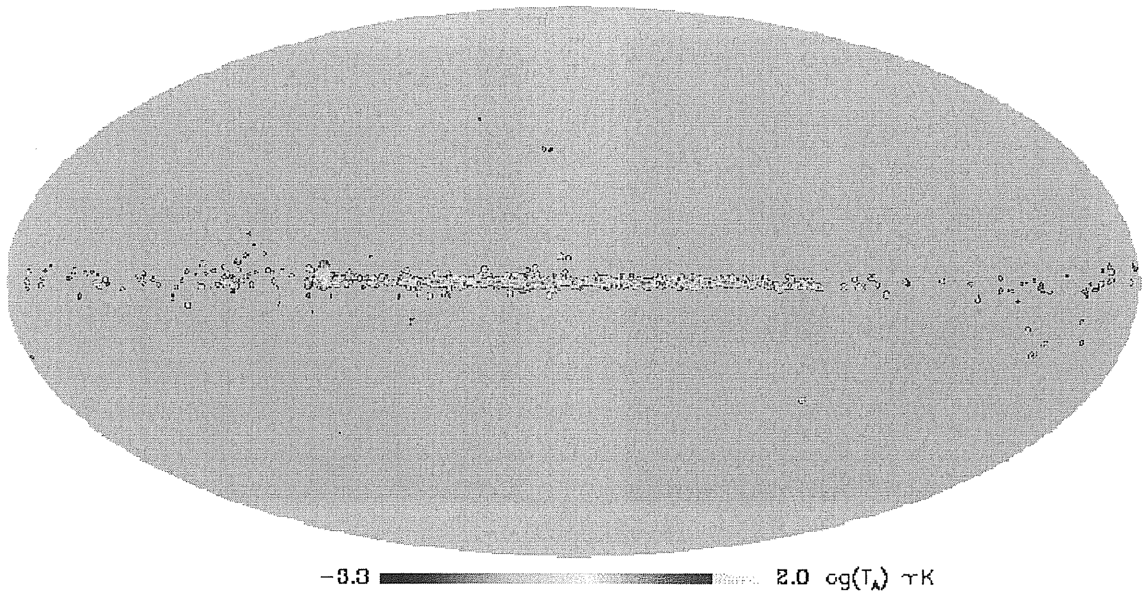

Figure 5.2: Simulated map, in terms of antenna temperature at 30 GHz, of the distribution of the Synthetic Catalog HII regions for an instrument with a FWHM of 33.6′. The map is displayed in an all-sky Mollweide projection. The colours indicate the values of $\log(T_{\mathrm{antenna}})$ (see the colour bar). Signals reach values of up to tens of mK. See also the text.

S/N bin, given a binsize of $\sim$ 0.05 (differential distribution), and the number of sources with S/N greater than a given value (cumulative distribution) for both PLANCK and *COBE*-DMR at $\sim$ 30 and $\sim$ 100 GHz. From Fig. 5.1 it is clear that the vast majority of sources in the Synthetic Catalog produce a signal well above the PLANCK detection threshold: 80% of them will have $S/N > 100$ (note, however, that the confusion noise has not been considered).

Thus, PLANCK's high sensitivity and high resolution should allow to significantly extend the existing HII regions data base. It is important to emphasize that none of the individual HII regions can been seen by *COBE*-DMR whose sensitivity, according to Eq. (5.1), is a factor of 6×10^3 lower than PLANCK's at 30 GHz and a factor 4×10^4 lower at 100 GHz. Fig. 5.2 shows the catalog HII regions as seen by PLANCK at 30 GHz, where the beam-width is 33.6'.

To produce the map in Fig. 5.2, we have implemented a code which simulates the contribution of each source in the Synthetic Catalog at a given angular resolution by assuming a symmetric Gaussian profile for the source brightness distribution and numerically convolves, in real space, the relevant part of the map – obtained after considering the contribution from all the sources in the catalog – with another symmetric Gaussian profile having the instrument FWHM. The final map is generated in HEALPix (Hierarchical

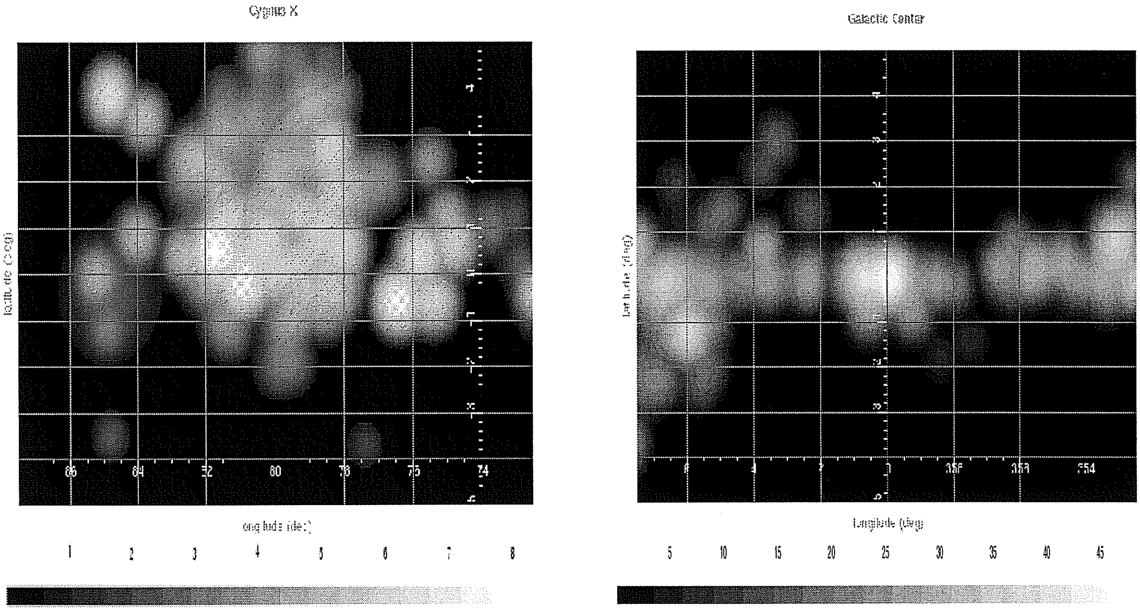

Figure 5.3: Simulated maps of the Cygnus X region (left panel) and of the Galactic Center region (right panel) at 30 GHz with a FWHM resolution of 33.6′. The units of the color bar are mK. Minimum and maximum refer to positive pixel signal values.

Equal Area and IsoLatitude Pixelization of the Sphere, by Gòrski et al. [130]). Fig. 5.3 shows the strong Galactic centre and Cygnus X regions. Antenna temperatures as high as ∼ 50 mK are seen.

5.3 The role of HII regions in instrumental calibration

As far as instrumental calibration for CMB observations is concerned, HII regions play a twofold role. On one side, it is necessary to investigate if, bright sources such as these, can degrade the calibration accuracy which, for such experiments, is particularly important[2]. On the other hand, since HII regions are non-variable sources and have quite a well-known spectrum, they also appear to be possible candidates for relative calibration. These two topics are discussed separately in the following.

---

[2] It can be shown that, to recover the values of cosmological parameters with the precision of a few %, CMB experiments must reach a calibration accuracy of order $\simeq 1\%$ (see, for instance, Cappellini et al. [50]).

5.3.1 The impact on the accuracy of absolute calibration

In the framework of the preparatory work for the PLANCK space mission[3], Cappellini et al. [50] have investigated the problem of how to achieve a high calibration accuracy by keeping under control the statistical [4] and systematic [5] errors which may affect the instrument performance. In this context, the contribution of HII regions has been analyzed. To clarify the subject, a brief summary of the basic calibration concepts is given.

Calibrating an instrument means converting the output signal of each detector channel (e.g. telemetry units in the case of a space instrument) to physical units (e.g antenna temperature). If the instrument response is linear:

$$T_A = G_0 V + T_{\text{offset}} \tag{5.2}$$

where V is the receiver voltage output corresponding to the sky antenna temperature T_A; $\mathrm{T}_{\text{offset}}$ the instrumental offset; G_0 the calibration factor, constant to first order. In practice, though, G_0 can vary due to instrumental effects such as variations of the amplifier gain or thermal instabilities. For differential measurements, as in the case of CMB anisotropy experiments, the calibration factor is determined by comparing pairs of sources:

$$T_2 - T_1 = G_0(V_2 - V_1) \tag{5.3}$$

where $T_2 - T_1 = \Delta T_A$ is the antenna temperature difference of the two sources[6] while $V_2 - V_1 = \Delta V$ is the corresponding detector output. As we have previously mentioned, the error on the determination of G_0 depends on the a-priori uncertainty on the calibration source temperatures, $\sigma_{\Delta T_A}$, and on the intrinsic detector noise, $\sigma_{\Delta V}$. According to (Bersanelli et al. [19]):

$$\frac{\sigma_{G_0}}{G_0} = \frac{\sqrt{\sigma^2_{\Delta T_A} + (G_0\sigma_{\Delta V})^2}}{\Delta T_A} \tag{5.4}$$

Eq. (5.4) allows an estimate of the accuracy on G_0 for a single pair of sources. However, experiments operating from space cover large areas of the sky and the calibration factor is evaluated from the overall distribution of ΔT_A and ΔV values by minimization of the χ^2 function:

$$\chi^2(g) = \sum_k \left[\frac{\Delta V_k - \Delta T_k^{cal}/g}{\sigma_{\Delta V_k}}\right]^2 \tag{5.5}$$

---

[3] For a summary of the instrumental characteristics of the satellite, we refer the reader to section 5.2.

[4] Intrinsic detector noise.

[5] Uncertainty on the emitted flux density of the calibration sources.

[6] Usually, the pair consists of a bright source in the sky and the underlying background.

where k is the index of the pair of observed points used for calibration. According to this expression, G is the value of g that minimizes $\chi^2(g)$ while G_0 is the true value of the calibration factor, i.e. the value which has to be recovered.

For CMB anisotropy experiments, an ideal calibration source is represented by the CMB dipole[7] which not only always enters the field of view of the instrument, thus allowing to continuously calibrate it, but also it has been accurately measured by the COBE-FIRAS instrument (Fixsen et al. [110]). Its amplitude ($\Delta T = T_0\beta = 3.372 \pm 0.014$ mK in the direction (l,b) = ($264.14^0 \pm 0.15$, $48.26^0 \pm 0.15$)) is known with the accuracy of $\simeq 0.4\%$.

In addition to the CMB dipole, different components contribute to the emission at the frequencies of CMB experiments. These emissions act as contaminants of the prime calibrator, i.e. the dipole, and generate a systematic uncertainty in the calibration process. The main sources of emission which have been considered by the analysis are the ones which are diffuse in nature such as synchrotron, free-free and interstellar dust emission. Known HII regions drawn from the catalog described in Chapter 3 have also been included while extragalactic point sources have not been taken into account at this stage of the analysis. The amplitude and spatial distribution of all the considered components have been modelled[8] to produce synthetic sky maps in the HEALPIx scheme[9]. Each emission has been extrapolated to the frequency of interest by using a suitable spectral index for that specific component. In particular, HII region flux densities have been extrapolated with the spectral index $\alpha = -0.1$. The uncertainty associated to these foreground components have also been considered and a full-sky map of errors, $\sigma_T(\alpha,\delta)$, has been built. With both the synthetic maps for each component and the full-sky error map at the frequency of interest, two types of sky maps have been produced at each considered frequency, namely, a *calibrator* map:

$$T^{cal}(\alpha,\delta) = T_{dip}(\alpha,\delta) + T_{sync}(\alpha,\delta) + T_{dust}(\alpha,\delta) + T_{ff}(\alpha,\delta) \tag{5.7}$$

which corresponds to our knowledge of the sky based on available data and an *observed* map:

$$T^{obs}(\alpha,\delta) = T^{cal}(\alpha,\delta) + T_{HII}(\alpha,\delta) + \sigma_T(\alpha,\delta) \tag{5.8}$$

---

[7] A dipole pattern is what appears to an observer who moves with velocity $\beta = v/c$ with respect to the CMB field and it is given by:

$$T(\theta) = T_0 \frac{\sqrt{1-\beta^2}}{1-\beta cos(\theta)} = T_0 + T_0 \beta cos(\theta) + \emptyset(\beta^2) \tag{5.6}$$

where T_0 is the isotropic CMB temperature and θ is the angle between β and the line of sight.

[8] The process of modelling has been performed, in the case of extended emissions, by using available templates for each diffuse component. In particular, the analysis makes use of the following maps: for synchrotron emission, the 408 MHz map by Haslam et al. [150]; for dust emission, the 100 μm IRAS/DIRBE map by Schlegel et al. [274]; for free-free emission, a template has been obtained by assuming that free-free is spatially correlated with dust and that, its amplitude at 100 GHz is 1/3 of that of dust (De Zotti et al. [85]).

[9] The reader is referred to section 5.2 for details and references.

where:

$$\sigma_T(\alpha,\delta) = \sqrt{\sigma^2_{T_{dip}} + \sigma^2_{T_{sync}} + \sigma^2_{T_{dust}} + \sigma^2_{T_{ff}}} \tag{5.9}$$

which is the *real* sky. As we can see from comparison of eqs. (5.7) and (5.8), the HII region emission has been added only in the observed sky. This is because, in order to be more conservative, the systematic error on the recovery of the calibration factor introduced by HII regions has been estimated under the assumption that no information on their presence in the sky is available while calibrating the instrument. To complete the simulation process, it has then been necessary to create fictitious data streams taking into account the PLANCK scanning strategy[10]: in practice, the calibrator and observed maps are converted into antenna temperature and convolved with a gaussian beam with the Full Width Half Maximum (FWHM) of PLANCK at each considered frequency. This step has been realized by making use of the pipeline developed by the PLANCK Data Processing Center and which incorporates all the specifics of the payload and of the receivers (i.e. noise properties). At this point, the calibrator factor G is computed from the data streams by applying eq. (5.5) for two different time-scales: each hour and day for a total integration time equal to the mission time ($\sim$ 1 year). The results retrieved by the simulations are the following:

- known HII regions affect less than 0.5% of the sky, contaminating $\sim$ 7% of the scan circles in a very small number of pixels per circle;
- in a very limited number of cases, the systematic error introduced by the presence of HII regions goes beyond the threshold of the overall 1% uncertainty which is required by CMB anisotropy experiments;
- however, if the calibration procedure is repeated excluding in the χ^2 function the pixels with known HII regions, the systematic error is significantly decreased also in those cases.

5.3.2 Candidates for relative calibration

In the previous section, we have seen that HII regions do not impact significantly on the process of absolute calibration in the case of high-sensitivity, high-resolution CMB experiments such as PLANCK. In general, these objects cannot be used for absolute calibration since the accuracy on their flux density and position is often not very high and, also, the number of transits in the instrument field of view over the entire mission lifetime is very limited. However, objects such as HII regions can be very useful for the so-called *relative* calibration which consists in monitoring the stability of the calibration

---

[10] PLANCK sits on a Lissajous orbit around the Lagrangian point L2 of the Sun-Earth system. The spacecraft spins at 1 r.p.m. and the field of view is 5^0 from the telescope optical axis at a given angle $\alpha \simeq 85^0$ from the spin axis which is repointed of $2.5'$ every hour to maintain the anti-solar direction.

factor G[11] over the mission time. In this case, the physical characteristics which are required are brightness, compactness and temporal stability which make these sources easily recognizable in the received signal.

5.4 The use of HII regions for beam-shape and pointing reconstruction

HII regions are bright and compact sources so that they represent suitable candidates for beam reconstruction in experiments operating from radio up to infrared frequencies with a few arcmin-resolution. In the case of CMB measurements performed from space, two techniques have been suggested for the in-flight reconstruction of the beam: on one side, the use of planet transit (Burigana et al. [44]); on the other the use of the interplay between amplitudes and phases of the CMB signal with the instrumental noise (Chiang et al. [55]). In particular, the former method, which allows the complete reconstruction of the beam shape down to a level of -25 dB, despite being originally conceived for planet transit, can be applied to any other class of bright and compact objects, such as HII regions. Furthermore, these sources have also the advantage of providing a larger number of transits over the mission time, compared to planets.

The characteristics which make HII regions viable candidates for beam reconstruction – brightness and compactness – are also important for pointing reconstruction. It is important to recall that, for example, a few compact HII regions – namely, RCW38, RCW57, IRAS08576, IRAS1022 – were used by BOOMERAng (de Bernardis et al. [81]) for this purpose, together with other auxiliary bright radio sources, such as QSOs and BL LACs. In addition, recently, Walsh [335] has suggested the use of UCHII as pointing calibrators for single dish submillimeter telescopes.

Both for beam reconstruction and pointing, the HII region Catalog presented in Chapter 3 provides useful information for the selection of sources. As an illustrative case, the Synthetic Catalog contains 36 HII regions which have a flux density $\geq$ 30 Jy at 30 GHz[12] and a diameter $\leq 5'$. More accurate flux densities and positions of cataloged HII regions will also become available soon from ground-based aperture synthesis observations such as the nearly completed Canadian Galactic Plane Survey[13].

5.5 The contribution of HII regions to straylight

HII regions, as delineated in Fig. 5.3, can in principle also represent a significant contribution to one of the most critical spurious systematic effects in CMB experiments, the so-called *straylight contamination.* This effect consists in unwanted radiation coming

---

[11] See section 5.3.1, eq. (5.5) for the definition of G.

[12] The extrapolation from 2.7 GHz has been made with the spectral index -0.1.

[13] More information at: http://www.ras.ucalgary.ca/CGPS/

from direction far from the optical axis and it does not pertain only to the telescope but to the entire optical system, including solar panels, shielding, thermal stability and focal assembly components. The variation of straylight signal over the mission time contaminates the anisotropy measurement in a way which is not easily controllable in the data analysis process. This is mainly due to the fact that an accurate measure, both on the ground and in flight, of the antenna pattern at very low response levels is quite complicated. In addition, the straylight signal, once it is reduced by an appropriate optical design (see below), is expected to be embedded in a mixture of true signal, noise and other systematic effects (see, for instance, Burigana et al. [43]).

The antenna response far from the beam axis – denoted as *sidelobes* – largely depend on diffraction and scattering effects on the edge of the telescope mirrors, as well as from other supporting structures. Therefore, one can try to reduce the entity of such features by decreasing the illumination at the edge of the primary mirror which, in other words, corresponds to increase the *edge taper*, that is the ratio between the power per unit area incident on the center of the mirror and the power incident on its edge. In practise, the higher the edge taper, the lower the sidelobes level and the straylight contamination. Unfortunately, though, increasing the edge taper has a negative impact on the angular resolution, once the size of the primary mirror is fixed (Mandolesi et al. [207]). Consequently, it is extremely important for CMB anisotropy experiments to reach the best trade-off between the improvement of the angular resolution – required to measure the high-order acoustic peaks of the anisotropy power spectrum – and the minimization of the straylight contamination, especially the one due to the Galactic emission, including the contribution of HII regions.

A systematic investigation of this issue, at 100 GHz[14], has been done by Burigana et al. [45], again in the context of the preparatory work for the PLANCK space mission. The general idea behind this analysis is the following: for each receiver and for a given optical configuration – corresponding to a fixed value of the edge taper for a given position of the receiver – and a simulated Galactic emission at a specific frequency, fictitious satellite data streams are produced, taking into account the scanning strategy of the instrument. The straylight in the sidelobes so obtained is then evaluated for each of the chosen optical configurations. The best trade-off between angular resolution and straylight is then the optical configuration which allows a minimization of the straylight signal without a degradation of the resolution under a certain threshold. In particular, as a reference frame, two angular regions are defined within the antenna pattern[15]: the *intermediate* and the *far* sidelobes. The intermediate pattern is the angular region between 1.2^0 and 5^0 while the far pattern corresponds to off-axis angles $> 5^0$. For simulating the Galactic emission, maps in the HEALPIx scheme[16] of each of the emission components – synchrotron, free-free and dust emission – have been built by modelling their amplitude and

---

[14] For the choice of frequencies, see section 5.3.1.

[15] It is important to stress that such definitions are arbitrary and are used only as a practical reference for the discussion and evaluation of the results.

[16] See section 5.2. for details and reference on HEALPIx.

spatial distribution using available extended surveys as a reference[17]. The extrapolation to the considered frequency has been made by adopting a suitable spectral index for each component. For HII regions, the Synthetic Catalog described in Chapter 3 has been exploited and source flux densities have been extrapolated with a spectral index of -0.1. Data streams have been produced by means of the same pipeline adopted for the calibration study of section 5.3.1. The results of the simulation indicate that:

- the overall straylight contamination is quite low (at the level of a few μK);
- the contamination in the far sidelobes is larger than in the intermediate sidelobes;
- the contribution on the far sidelobes is mainly due to the diffuse components;
- HII regions do not impact significantly on the straylight signal, neither in the intermediate nor in the far sidelobes;
- a trade-off between angular resolution and straylight is therefore easily achievable for each receiver.

5.6 Radio/millimeter studies of HII regions

The Synthetic Catalog discussed in Chapter 3 provides a rich source of information for further studies of individual HII regions. In particular, in this section we want to emphasize the scientific case for observations in the millimeter band, for which the Synthetic Catalog may represent a valid tool for selecting detectable sources and estimating flux densities.

Compact HII regions are bright millimetric sources of our Galaxy. Yet, direct information on their emission at these frequencies is quite poor, although plenty of measurements are available both at centimeter and far infrared/sub-millimetric wavelengths. Studies of selected objects have been performed (Schwartz [276]; Chini et al. [56]; Gordon [128]; Gear et al. [121]) but they concern only very limited samples. Moreover, despite the wealth of data at neighbouring frequencies, the extrapolation to the millimetric band is quite complicated. At these wavelengths the transition between two different physical mechanisms occurs (see Fig. 5.4): at cm wavelengths, the continuum emission is primarily free-free resulting from the close encounters of unbound, electrically charged particles ionized by ultraviolet photons; at sub-mm wavelengths, it is mostly thermal radiation which comes from the dust grains heated by infrared radiation. This fact illustrates by its own the relevance of observations in this frequency range.

At the same time, millimetric observations of compact HII regions can also shed light on fundamental questions on the physics of star forming regions. A deeper understanding, for instance, is required of the physical relationship between the radio and FIR/submm

---

[17] See section 5.3.1 for the data base which have been used.

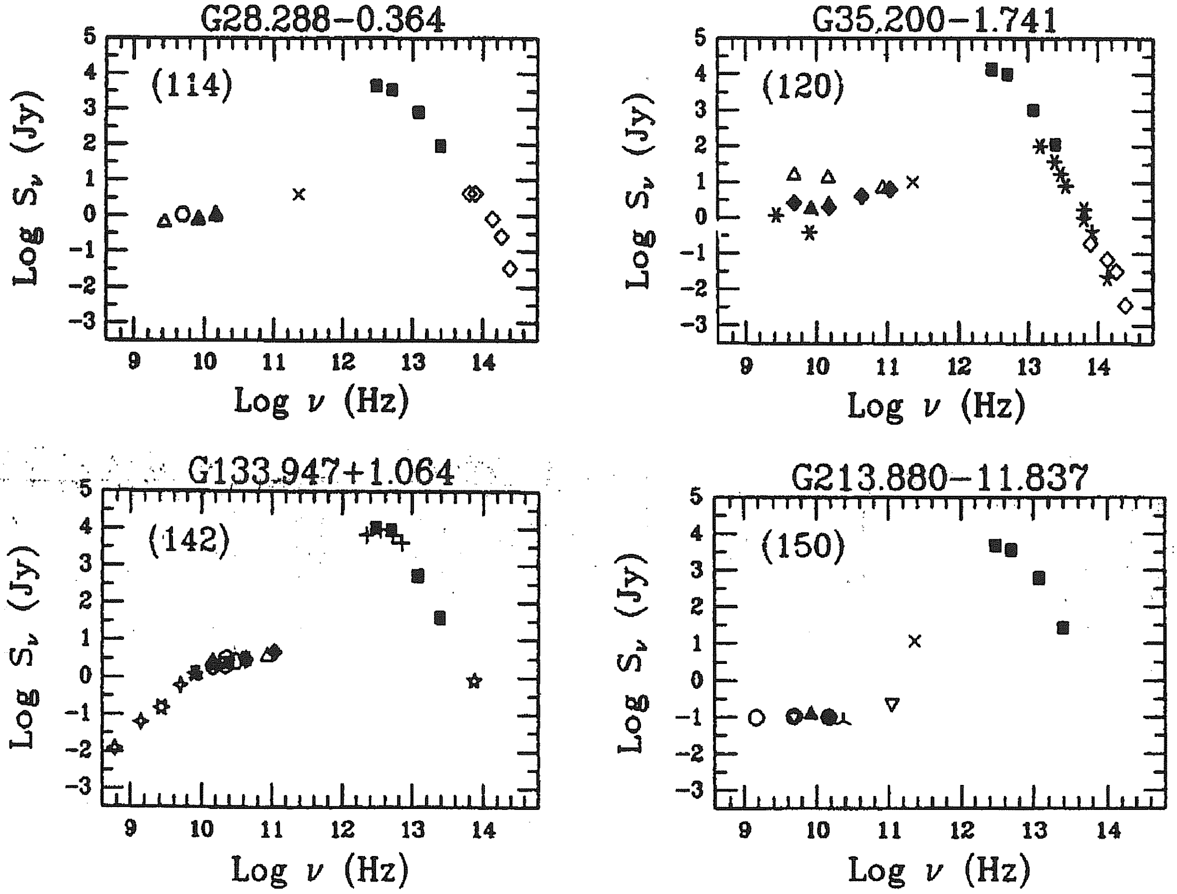

Figure 5.4: Examples of UCHII region spectra from Kurtz et al. [192]. Spectra range from radio to near-infrared wavelengths. Each plot is labelled by the Galactic coordinates of the radio source and also by the figure number which is indexed by source in Table 2 of Kurtz et al. The flux densities shown were obtained with a range of instruments (references given in Kurtz et al. [192]). The spectra exhibit a remarkable similarity and in all cases show a peak at ~ 100 μm which is at least three orders of magnitude higher than the radio continuum peak at ~ 10 GHz.

emission mentioned above. Because the heating mechanisms are different and because the two components may be differently distributed within a source, the free-free emission and the dust emission do not have to be spatially coincident. A displacement between the radio and the FIR contours of emission in M17 has been detected (Wilson et al. [344]; Gatley et al. [118]). More data are nonetheless necessary to constrain this kind of result. By combining high-resolution measurement of the emission at millimeter wavelengths and similar data at centimeter wavelengths, it is possible to realize a comparative study of the morphology in the two frequency bands.

Likewise, comparison of millimeter data with auxiliary data in the sub-millimeter, FIR and IR regions establishes the emission spectrum of the dust grains and allows to constrain crucial parameters such as the dust temperature and the emissivity index of the modified black-body spectrum. These two parameters are crucial in narrowing the possible choices of grain material. A sample of compact HII regions selected from the IRAS sources has been measured (Chini et al. [56]): the derived average temperatures are in the range between 26 K and 65 K when the emissivity index, β, ranges between 2 and 1. Nevertheless, considering the large uncertainty affecting these results, further, more accurate measurements appear to be necessary.

Although not tightly related to the radio/millimeter studies on individual HII regions we are considering in this section, it is also worth mentioning that the Synthetic Catalog may provide a useful crosscheck for source identification in IR experiments such as DENIS (Epchetein et al. [101]) and 2MASS (Kleinmann [184]) for which a major problem is represented by the association of an observed source with a bright IR Galactic object like an HII region rather than with a galaxy.

5.7 HII regions and the polarized diffuse Galactic radio emission

One of the applications of the HII region Catalog presented in Chapter 3 is in the study of the polarization of Galactic foregrounds. Such studies are particularly important since several ongoing or planned experiments (see Staggs et al. [307] for a recent review) are designed to reach the sensitivities required to measure the expected linear polarization of the Cosmic Microwave Background (CMB), and CMB polarization measurements have already been achieved by the DASI (Kovac et al. [186]) and WMAP (Bennett et al. [14]). While there is a very strong scientific case for CMB polarization measurements (cf., e.g., Zaldarriaga [352] and references therein), these are very challenging both because of the weakness of the signal and because of the contamination by foreground emission which may be more polarized than the CMB. Unfortunately, our knowledge of polarized foreground components is also very meager (see Davies & Wilkinson [77] for a recent review).

As part of the investigation of the polarized Galactic synchrotron emission (which is the

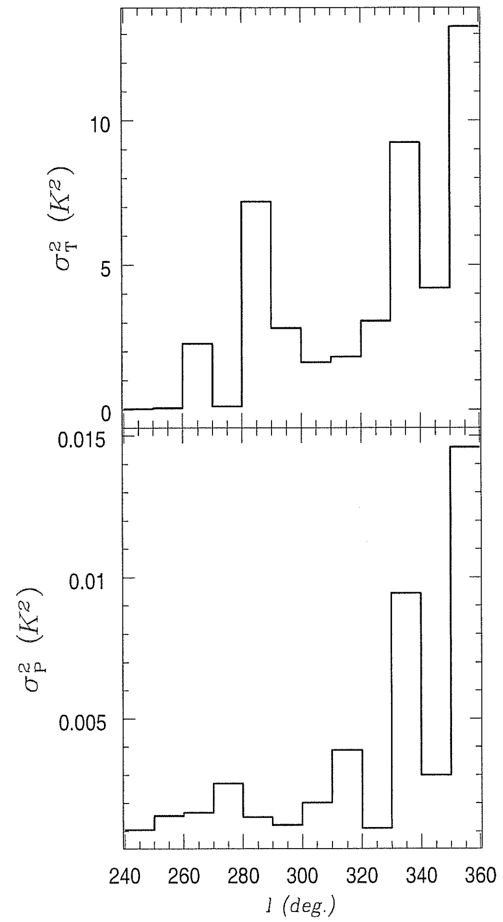

Figure 5.5: Total (upper panel) and polarized intensity fluctuations in the area surveyed by D97 (from Baccigalupi et al. [7]).

Table 5.1: Bright HII regions between l = 300° and l = 320°.

l (deg.)	b (deg.)	$S_{2.7\mathrm{GHz}}$ (Jy)	Size (′)
305.1	0.1	16.3	5
305.2	0.0	62.2	7
305.2	0.2	50.1	4.8
305.4	0.2	62.2	3.5
305.6	0.0	37.6	8
307.6	-0.3	12.2	4.2
308.6	0.6	17.8	7.8
308.7	0.1	12.0	–
308.7	0.6	21.0	–
309.6	1.7	51.0	7.5
310.8	-0.4	16.6	10.9
311.9	0.1	12.9	4
311.9	0.2	11.5	4
312.3	-0.3	10.0	–
316.3	0.0	12.0	–
316.8	-0.1	43.2	2.7
317.0	0.3	15.0	7
318.0	-0.8	11.0	10.8
319.2	-0.4	12.4	5.9
320.2	0.8	11.0	1.8
320.3	-1.4	12.0	–
320.3	-1.0	23.0	–
320.4	-1.1	17.5	6
320.4	-1.0	13.0	5.6

likely dominant foreground contribution at microwave frequencies, at least at intermediate to large angular scales (Tegmark et al. [314]), Baccigalupi et al. [7] have performed an analysis of the polarimetric Parkes survey data (Duncan et al. [96], [97]; hereafter D97). D97 covers 127° of Galactic longitude ($238° < l < 5°$) out to at least $b = \pm 5°$ (for $340° < l < 5°$ the survey extends to $b = +7°$, for $340° < l < 352°$ to $b = -7°$, and for $240° < l < 270°$ to $b = -8°$) with an angular resolution of 10.4′. The center frequency of the observation is 2.417 GHz. A comparison of the total power and polarized emission maps shows little correlation. The same effect is seen for the medium-latitude 1.4 GHz polarimetric survey (Uyaniker et al. [324]; Uyaniker et al. [325]). While the total intensity clearly peaks on the Galactic Plane (apart from a number of spurs and loops extending to high Galactic latitude), the polarized intensity is much more uniformly distributed. Also, many sources which are very bright in total power are not seen in polarized emission and, conversely, bright regions of extended polarization do not appear to be associated to sources of total-power emission (D97, U99).

Two main factors may contribute to this situation. On one side, many bright structures on the Galactic plane are (unpolarized) HII regions and significant thermal radio emission is also expected between and above bright HII regions in our Galaxy: Duncan et al. [96] estimate a thermal flux level of the order of 100 mJy per beam area at 2.4 GHz, comparable to the level of the radio continuum often observed near these regions. The large thermal contributions to the Galactic emission, which are concentrated close to the Galactic plane, obviously make it very unlikely that the total intensity power spectra for these regions can be representative of the synchrotron power spectra at high Galactic latitudes.

On the other side, differential Faraday rotation or variations of the magnetic field orientation may strongly depolarize the emission from distant regions of the Galaxy (Burn [46]; Gardner & Whiteoak [117]; for a recent, detailed discussion of depolarization mechanisms, see Sokoloff et al. [302]) so that only the polarized emission of relatively local origin can be observed. The two factors may act together: variations in the density of thermally emitting electrons may lead to a large enough differential Faraday rotation to produce substantial depolarization; in addition, the magnetic field may be tangled by turbulent motions of the ionized gas, leading to further depolarization.

Fig. 5.5 shows the fluctuations around the mean of both total and polarized intensities for the D97 survey, as a function of the angular distance from the Galactic center, for regions 10° wide in longitude. It may be noted that polarization and total intensity fluctuations are correlated only near the Galactic center. The intensity peaks are associated to the most prominent Galactic sources, i.e. the Galactic center and the Vela Supernova remnant ($260° \leq \mathrm{l} \leq 270°$). For polarization, the signals at $320° \leq \mathrm{l} \leq 360°$ are due to features appearing near the Galactic center such as the polarization "plume" (Duncan et al. [98]), while away from the Galactic center, at $\mathrm{l} \leq 320°$, only the supernova remnant produces peaks both in total and in polarized intensity.

Also, and most important, this figure shows that the total intensity fluctuations are higher by 2 or 3 orders of magnitude than the polarization ones, implying a polarization degree much lower than the maximum expected for un-depolarized synchrotron emission.

In fact, most of the observed intensity close to the Galactic plane appears to come from bright HII regions. For example, the region between $\mathrm{l} = 300°$ and $\mathrm{l} = 320°$ contains 95 bright HII regions drawn from the catalog presented in Chapter 3; the brightest ones are listed in Table 5.1 with their flux density at 2.7 GHz and their angular sizes which are typically in the range $2'$–$10'$. It is easily checked that these sources account for most, if not all, of the total intensity reported by D97. The intensity fluctuations due to them can be roughly estimated to be:

$$\sigma^2_{HII} \simeq \frac{\sum_i S_i^2}{N_{\rm pixels}} , \tag{5.10}$$

where S_i is the flux of the $i-th$ HII region in the Catalog, scaled to the D97 resolution and to 2.4 GHz by assuming a spectral index of 0.1 ($S_\nu \propto \nu^{-0.1}$), appropriate for the free-free emission. This yields $\sigma_{HII} \simeq 1$ Jy/beam, close to the value of 1.4 Jy/beam that we obtain from the D97 data. These sources, bright in total intensity, are not polarized, although Keating et al. [179] claim that Thomson scattering by the electrons in the HII region itself may polarize the radiation tangentially to the edges of the cloud structure at a maximum level of about 10% for an optically thick cloud. Therefore, under the assumption of no polarization, the observed effect according to which the total power along the Galactic plane has little correspondence in polarization, as from Fig. 5.5, can be explained.

5.8 Conclusions

In this chapter, we have seen that the HII region Catalog provides an up to date finding list for the brightest HII regions available for study at microwave and sub-millimeter wavelengths. In particular (section 5.2), the Catalog appears to be relevant for future high sensitivity CMB mapping projects such as PLANCK. We have also shown (section 5.3.1) that, although Galactic HII regions do not impact severely on the recovery of the calibration factor, individual compact bright HII regions have a role in relative calibration (section 5.3.2). Moreover, we have seen (section 5.4) that HII regions are useful as pointing and beam-shape indicators and that (section 5.5) the HII region Galactic distribution contribute to the straylight radiation without introducing a significant contamination. In section 5.6, we have pointed out the need of observations of HII regions at millimeter wavelengths for which the Catalog provides information for the selection of sources and estimates of flux densities. Finally, in section 5.7, we have described part of an analysis of the polarized Galactic synchrotron emission for which it has been important to consider the contribution given by HII regions in order to clarify some features of the observed signal.

Chapter 6

A preliminary analysis of the diffuse component in the thin layer

6.1 Introduction

So far, we have considered only the role of HII regions for the warm ionized gas thin layer. However, as we know, this is not only contributed by individual sources but also by diffuse gas. In this chapter, a preliminary analysis of the diffuse component is presented. At radio wavelengths, the ionized gas emits continuum thermal bremsstrahlung radiation (also called free-free) as well as recombination lines. Here we focus on the continuum radiation which, as we have already discussed (Chapter 2, section 2.3.3), cannot be traced directly being emitted over a range of frequencies similar to that of synchrotron radiation produced by relativistic electrons accelerated in the Galactic magnetic field. This fact then requires that, to investigate the diffuse contribution to the thin layer and its relation with HII regions, we single out the free-free from the total observed radio emission. Such decomposition can be achieved by exploiting the spectral dependence of each emission component if data are available at least at two different frequencies. Once the component separation has been performed, we can study the physical properties of the free-free distribution and make a comparison with what we know for HII regions.

The chapter is organized as follows. Section 6.2 describes the data base used for the analysis. Section 6.3 discusses the determination of the zero levels of the considered surveys. Section 6.4 presents the details of the spectral analysis. Section 6.5 shows the results of the component separation and the recovered estimate for the contribution of HII regions to the global free-free emission budget. In section 6.6 the main results of the analysis are summarized.

6.2 Choice of the data base

We first need to select a region of the Galaxy surveyed at many frequencies, close to the plane and in a longitude range where we expect the emission from the ionized gas to be particularly bright. At the same time, we also want to avoid regions where the source of the observed emission is not fully understood such as areas located in the proximity of the Galactic center. Following these guidelines, we have decided to conduct our analysis on the region $20^0 < l < 30^0$ and $-1.5^0 < b < +1.5^0$. At $l \sim 30^0$ and $l \sim 20^0$, the line of sight is tangent, respectively, to the Carina-Sagittarius and the Crux-Scutum arm therefore, in both directions, maximums of emission are expected. As for the latitude range, this has been somehow limited by the sky coverage of one of the two surveys we have used, namely the 5 GHz Parkes survey by Haynes et al. [151]. The reason for choosing a data set with limited latitude coverage relies in the fact that, as we are also going to discuss in the next section, a spectral component analysis requires, for being reliable, the use of high-quality data. In this context, the quality of the data is determined, mainly by the precision of the calibration procedure and by the accuracy in mantaining the baseline reasonably constant. The 5 GHz Parkes survey and the 408 MHz survey by Haslam et al. [150] appear to meet such requirements. Details about the surveys are given hereafter and summarized in Table 6.1.

The 408 MHz survey: The 408 MHz map covers the whole sky and it has been obtained through the combination of four different surveys using, respectively, the Jodrell Bank MkI, the Bonn 100-m, the Parkes 64-m and the Jodrell Bank MkIA telescopes. All the observations were made with a similar observing strategy (i.e. nodding scan technique, Haslam et al. [149]), on large parabolic reflector telescopes. The antenna temperatures of all surveys have been calibrated into brightness temperature using the 404 MHz absolutely calibrated observations by Pauliny-Toth & Shakeshaft [238]). Small corrections were applied to the brightness temperatures of the Jodrell Bank and Effelsberg 100-m surveys: 1 K and 1.75 K were, respectively, subtracted from the brightness temperature scales; in the Effelsberg case, the temperature scale so obtained was then multiplied by 1.085. The temperature scale of the final map is believed to be accurate to better than 10% while the average zero-level has an uncertainty of ± 3 K. Each survey was brought to a standard resolution of $0.85^0 \times 0.85^0$ before combination to the final map.

The 5 GHz survey: The 5 GHz survey was made using the Parkes 64-m telescope and has an angular resolution of $4.1'$. It covers $190^0 \leq l \leq 40^0$ and $-1.5^0 \leq b \leq +1.5^0$. The primary scan direction was chosen to be either right ascension or declination, whichever was nearer to being orthogonal to the galactic plane. In particular, the longitude range $336^0 \leq 1 \leq 40^0$ was scanned in right ascension while the longitude range $180^0 \leq 1 \leq 336$ was scanned in declination. The region of the sky to be surveyed was divided into blocks, each block being $\sim$ 16 square degrees in area. Baseline levels within each block were set by reference to two tie-down scans for which points well off the galactic plane

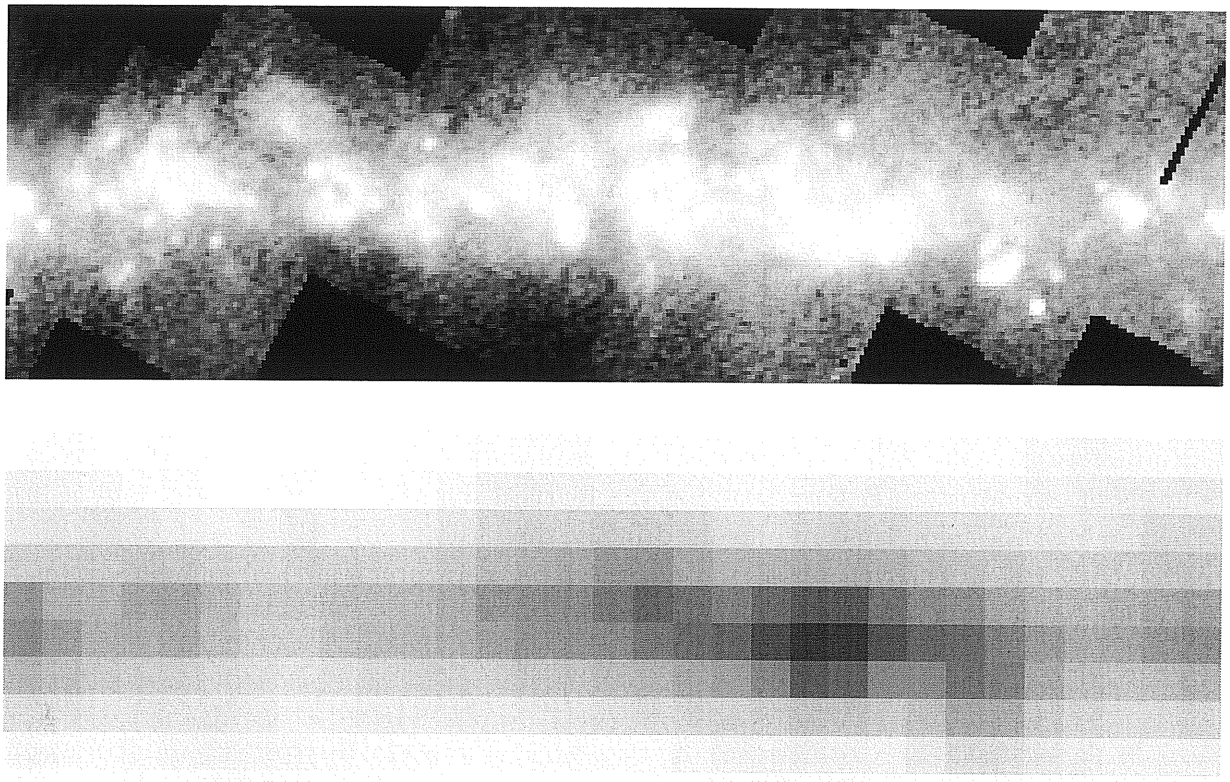

Figure 6.1: The selected Galactic region - $20^0 < l < 30^0$ and $-1.5^0 < b < +1.5^0$ - in the 5 GHz Parkes survey (top panel) and in the 408 MHz Haslam et al. survey (bottom panel). Clearly, the 5 GHz survey, having much higher resolution, allows us to distinguish the details of emission, including individual sources.

were assigned to the zero level. The tie-down scans were chosen to be as long as possible to keep the overall baselines consistent within an area as large as possible. Overall, the zero level, although it was set arbitrary, is believed to be constant over the whole series of blocks (150) to within ~ 0.2 K. The sky brigthness temperature scale has an accuracy of $\sim 10\%$.

6.3 Zero level determination

As mentioned in the introduction, it is possible to perform the separation of the free-free from the synchrotron emission by exploiting the information on their spectral behaviour. However, this method is subject to large errors if the zero levels of each involved survey has not been accurately determined. For this purpose, we have made use of the auxiliary data at 2.3 GHz by Jonas et al. [174]. The 2.3 GHz survey, which has been made with the HartRAO 26-m telescope, covers 67% of the sky with a resolution of 20′. However, the digital format of the map that we worked with has been convolved to a final angular

Table 6.1: Summary of the main properties of the surveys used for the analysis.

Survey	ν	HPBW	Sky coverage
Haslam et al.	408 MHz	$51'$	whole sky
Parkes	5 GHz	$4.1'$	$190^0 \leq l \leq 40^0$ $-1.5^0 \leq b \leq 1.5^0$

resolution of 1.2^0. The estimateduncertainty in the temperature scale is less than 5% and the error in the absolute zero is better than 80-mK in any direction. For these characteristics, the 2.3 GHz data set represents a valid reference for setting the zero levels of our surveys. Before detailing the method applied to our case, we give a brief overview of the main concepts involved in the discussion.
Following Reich & Reich [250], the observed temperature T at a frequency ν can be written as the sum of a series of contributions:

$$T(\nu) = T_{gal}(\nu) + T_{cmb} + T_{ex}(\nu) - T_{zero}(\nu) \tag{6.1}$$

where: $T_{gal}(\nu)$ is the Galactic brightness temperature; T_{cmb} is the brightness temperature of the Cosmic Microwave Background ($= 2.73\pm0.05$ K, Smoot et al. [296]); $T_{ex}(\nu)$ is the contribution of the unresolved extragalactic sources; $T_{zero}(\nu)$ is the zero level correction. The contribution of the unresolved extragalactic sources can be estimated for frequencies up to $\sim$ 1 GHz according to:

$$T_{ex}(\nu) = 30K(\nu/178\;MHz)^{-2.75} \tag{6.2}$$

(Bridle[36]). This relation allows the extrapolation of the known value of 30 K at 178 MHz for the steep-spectrum sources. However, at frequencies higher than $\sim$ 1 GHz, flat-spectrum sources become dominant so that a proper estimate must be performed with a spectral index flatter than -2.75.
If we consider two frequencies ν_1 and ν_2 and we assume that the spectral index β over these two frequencies is constant in some region of the sky, the following relation is valid:

$$T(\nu_1) = A_{12}\{T(\nu_2) - T_{off}(\nu_2)\} + T_{off}(\nu_1) \tag{6.3}$$

where: $A_{12} = (\nu_1/\nu_2)^{-\beta}$ and $T_{off}(\nu)$ is the offset temperature. From eq. (6.1) and (6.3), it follows that:

$$T_{off}(\nu) = T_{cmb} + T_{ex}(\nu) - T_{zero}(\nu) \tag{6.4}$$

Consequently, by assuming T_{zero}=0 at one frequency, the value for T_{zero} at the other frequencies results. The spectral index β can be determined with a so-called T-T plot

(Turtle et al. [323]), i.e. by means of an extrapolation of the temperature differences $T(\nu_1) - T(\nu_2)$ towards zero. In practise, this technique is a direct application of eq. (6.3) and consists in a linear fit of the temperature emission distribution at the frequencies ν_1 and ν_2. The spectral index β can then be recovered from the slope of the fitted line while an estimate of the offset is given by the intercept of the line with the x-axis. The drawback of the method is that it can only be applied in regions of the sky in which β is roughly constant, i.e. in which there are no local intense features of emission. In our case, the selected region is highly contaminated by individual sources such as HII regions and SNRs (cfr. Fig. 6.1, the 5 GHz high resolution map). By searching in the HII region Catalog presented in Chapter 3, we find 102 catalogued sources in the longitude and latitude range that we are considering. A similar check in the Green Catalog (Green [137]) of SNRs retrieves 13 objects. Consequently, we are able to make use of the T-T plot technique for the 408 MHz survey for which high-latitude data are available where the emission is relatively smooth and unaffected by local intense features. Conversely, for the 5 GHz data we have worked out a different approach based on the comparison with the 2.3 GHz data of only selected points in the map where the emission has a known behaviour and for which a known spectral index can be used to extrapolate from one frequency to the other. Hereafter, the procedure followed for the 408 MHz and the 5 GHz survey is described in detail.

Zero level for the 408 MHz survey

After convolving the Haslam et al. map to the Jonas et al. angular resolution, we have selected the region at $-15^0 < b < -5^0$, $20^0 < l < 30^0$, and the corresponding one at $+5^0 < b < +15^0$, $20^0 < l < 30^0$. In this case eq. (6.3) reads:

$$\begin{aligned} T_{2.3GHz} &= (2.3/0.408)^{\beta}\left\{T_{408MHz} - T_{off_{408MHz}}\right\} + T_{off_{2.3GHz}} && (6.5)\\ &= (2.3/0.408)^{\beta}\, T_{408MHz} - (2.3/0.408)^{\beta}\, T_{off_{408MHz}} + T_{off_{2.3GHz}} && (6.6)\end{aligned}$$

The $T_{2.3GHz} - T_{408MHz}$ distribution can then be fitted with a linear funtion such as:

$$T_{2.3GHz} = a \times T_{408MHz} + b \tag{6.7}$$

where:

$$\begin{aligned} a &= (2.3/0.408)^{\beta} && (6.8)\\ b &= T_{off_{2.3GHz}} - (2.3/0.408)^{\beta} \times T_{off_{408MHz}} && (6.9)\end{aligned}$$

The results are shown in Fig. 6.2. The spectral index from the fitted slopes has a mean value $\overline{\beta} = -2.75$ which is in good agreement with published values of the spectral index

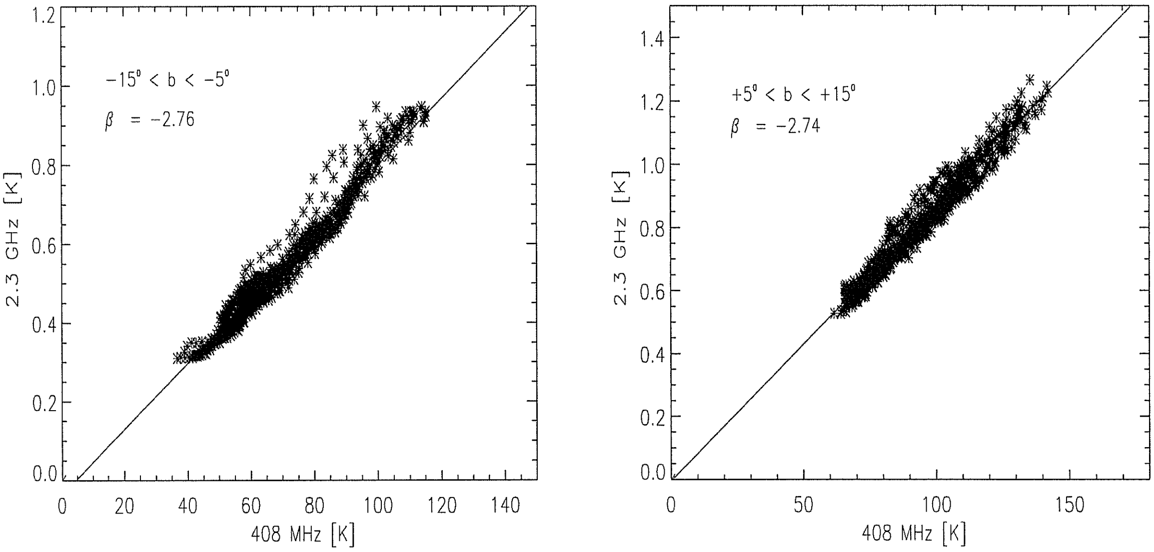

Figure 6.2: T-T plots between 2.3 GHz and 408 MHz for $-15^0 < b < -5^0$ (left panel) and $+5^0 < b < +15^0$ (right panel). The fitted slopes correspond to the spectral indices β reported in the upper left corner of the plots.

of the diffuse galactic emission at these frequencies (see Fig. 6.3) indicating that the quoted temperature scale errors of the two surveys are upper limits.

To recover the offset, we have assumed that the absolute zero level of the 2.3 GHz map is correct. From the values of the intercepts of the fitted lines and from eq. (6.5), it follows that the 408 MHz offsets for the two considered regions of the sky are: 4.6 K ($-15^0 < b < -5^0$) and 0.6 K ($+5^0 < b < +15^0$). Thus, different patches of the 408 MHz map seem to be characterized by different offsets. A similar result has been reported by Jonas [175]. However, the 408 MHz and the 2.3 GHz maps appear to be in general agreement. In fact, if we consider for both data sets a latitude cut of the region $-20^0 < b < +20^0$, $20^0 < l < 30^0$ and we scale the 408 MHz brightness temperature to 2.3 GHz adopting a spectral index for synchrotron emission $\beta = -2.8$, we obtain the result illustrated in Fig. (6.4): the consistency between the two cuts is very good at $|b| >\sim$ a few degrees from the Galactic Plane where the synchrotron radiation is dominant while in the proximity of the plane, where the thermal emission is intense, the offset between the two data sets clearly shows up. Taking this fact into account, we choose to use, as indicative offset, the mean value 2.6 K which we have obtained by taking the average between the two found values. This decision is also corroborated by the following consideration. The minimum value of the 408 MHz map for the range of selected coordinates ($20^0 < l < 30^0$, $-1.5^0 < b < +1.5^0$) is $\sim$ 70 K. Therefore, if we compare this to the offset uncertainty which is of order of few K, its is clear that the propagated error on the spectral index analysis due to such uncertainty is basically negligible. We will come back on this point in

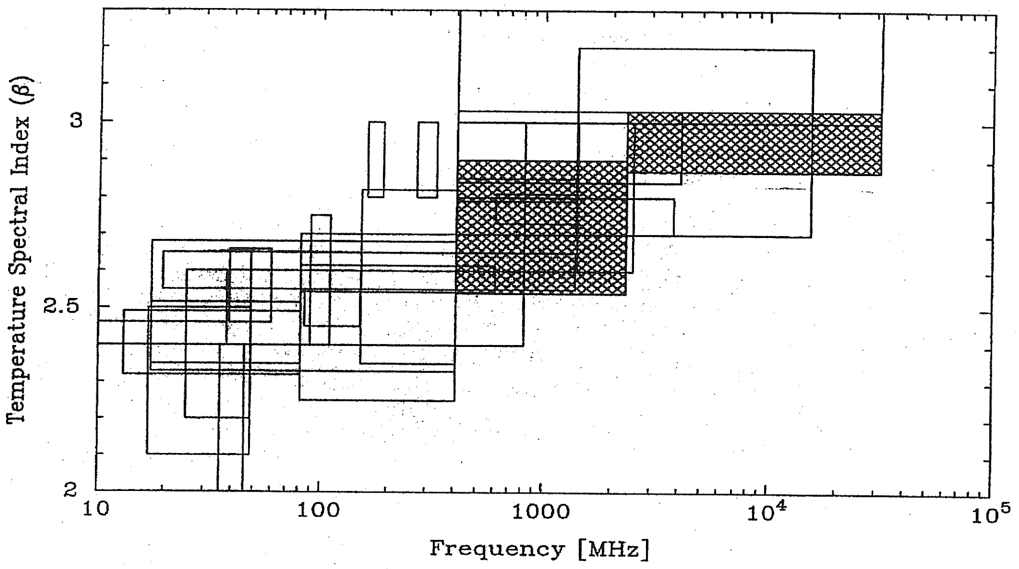

Figure 6.3: A summary of the published measurements of the spectral index of the diffuse galactic emission. The frequency span of each measurement is represented by the width of the associated rectangle while the height of the rectangle indicates the uncertainty in the spectral index. Plotted data are from: Turtle et al. [323]; Penzias & Wilson [241]; Andrew [5]; Yates & Wielebinski [350]; Bridle [36]; Howell [167]; Sironi [292]; Webster [337]; Hirabayashi [162]; Sironi & Bonelli [293]; Lawson et al. [194]; Reich & Reich [250]; De Amici et al. [80]; Kogut et al. [185]. Data in the shaded areas and figure are from Jonas [175].

section 6.4.2. For the moment, with the assumption: T_{off}=2.6 K, by considering a CMB contribution of 2.7 K and an extragalactic contribution of ~ 3 K (computed through the application of eq. (6.2)), we derive a value of T_{zero} ~ -3.1 K which is consistent with the published uncertainty.

Zero level for the 5 GHz survey

For the 5 GHz survey it has not been possible to use a strategy similar to the one applied to the 408 MHz case. In the 5 GHz survey one can clearly distinguish individual sources of emission superposing the diffuse background. As we have already mentioned, it is possible to identify 102 HII regions in the area of the sky we are considering. At radio frequencies, HII regions emit free-free radiation for which the spectral index β is well-known and equal to -2.1 (see Chapter 2, section 2.3.2). The offset of the Parkes map can then be derived according to this strategy: the 5 GHz map is scaled to 2.3 GHz with $\beta = -2.1$ and convolved to 1.2^0; the brightest pixels in the map containing HII regions are selected; the brightness temperature in these pixels is compared to the corresponding pixels in the 2.3 GHz map; the offset of the 5 GHz map is estimated from the average difference between these pairs of pixels. In order to be able to select in the Parkes data the pixels containing HII regions, we have built a simulated map for the 102

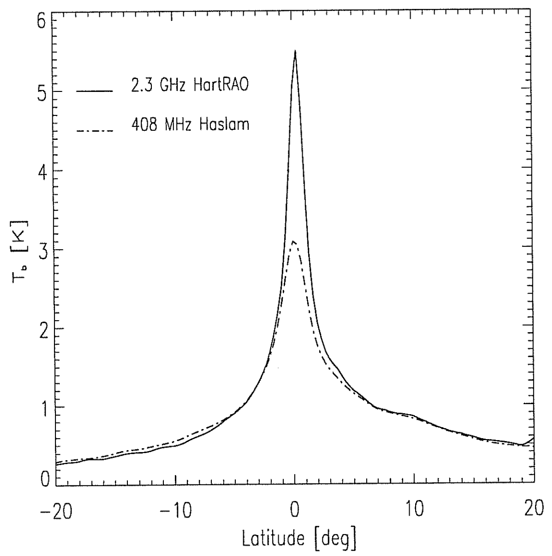

Figure 6.4: Latitude cuts for the 408 MHz survey and the 2.3 GHz survey. The Haslam et al. data have been convolved at the angular resolution of the Jonas et al. map and extrapolated to 2.3 GHz with a spectral index for synchrotron emission $\beta = -2.8$. The cuts have been obtained by averaging the data along slices 20′-wide along the latitude direction.

catalogued HII regions at the frequency of 5 GHz and at the angular resolution of 1.2^0. The simulated map has been constructed following the guidelines described in section 5.2 of Chapter 5. Flux densities and angular diameters data for the sources have been drawn from the Catalog discussed in Chapter 3. In practise, for deriving the Parkes offset we apply again eq. (6.3) which, in this case, reads like:

$$T_{HII_{2.3GHz}} = (2.3/5.)^{-2.1} \{T_{HII_{5GHz}} - T_{off_{5GHz}}\} + T_{off_{2.3GHz}} \tag{6.10}$$

By assuming that the absolute zero level of the Jonas et al. is correct, we compute $T_{off_{5GHz}}$ from:

$$T_{off_{5GHz}} = \langle\, (T_{HII_{2.3GHz}} - (2.3/5.)^{-2.1} \times T_{HII_{5GHz}})\, \rangle \tag{6.11}$$

for which we obtain: $T_{off_{5GHz}} \sim 0.67$ K. From eq. (6.4) we recover the zero-level correction. The CMB contribution had been already subtracted out from the digital version of the data we have used. As for the extragalactic component, at this frequency it is mainly due to flat-spectrum sources. This contribution can be roughly estimated assuming that it doubles the contribution from steep-spectrum sources as derived from eq. (6.2). This turns out to be of order of ~ 0.02 K therefore being completely negligible. The offset we have found thus also corresponds to the zero level correction of the Parkes data.

It is important to point out that in the case of the 408 MHz data, we could have not followed the lines now described for evaluating the offset. This is because, although in principle, we may select in the 408 MHz map the pixels containing SNRs for which a synchrotron spectral index may be adopted for the extrapolation to 2.3 GHz, in practise this turns out to be hardly feasible. The reason is that a quick check in the Green SNR Catalog shows that the 13 objects lying in the coordinates region we are working with have widely varying spectral indices, spanning the range -2.0 – -2.7. This fact clearly introduces in the analysis a systematic effect not easily controllable.

6.4 Spectral analysis and component separation

Having defined the zero levels for the 408 MHz and the 5 GHz survey, we can perform the component separation. For this purpose, we have made use of maps at the common angular resolution of 1.2^0 with a pixel size of $20'$. At each considered frequency, the brightness temperature $T_b(\nu)$ of a single pixel can be written as:

$$T_b(\nu) = T_{ff}(\nu) + T_{syn}(\nu) \tag{6.12}$$

where $T_{ff}(\nu)$ and $T_{syn}(\nu)$ are the free-free and synchrotron emission contribution at the frequency ν. By exploiting the information on the frequency dependence of each component, we have:

$$\begin{aligned} T_b(\nu_1) &= \left(\frac{\nu_1}{\nu_2}\right)^{\alpha_{gal}} T_b(\nu_2) \\ T_{ff}(\nu_1) &= \left(\frac{\nu_1}{\nu_2}\right)^{\alpha_{ff}} T_{ff}(\nu_2) \\ T_{syn}(\nu_1) &= \left(\frac{\nu_1}{\nu_2}\right)^{\alpha_{syn}} T_{syn}(\nu_2) \end{aligned} \tag{6.13}$$

In these expressions, α_{gal}, α_{ff} and α_{syn} are, respectively, the galactic, free-free and synchrotron spectral index. The fraction of thermal emission at each frequency can then be obtained by combining eq. (6.13) to (6.15). In particular, for the case at 5 GHz:

$$\begin{aligned} T_{b_{5GHz}} \left(\frac{0.408}{5}\right)^{\alpha_{gal}} &= T_{ff_{5GHz}} \left(\frac{0.408}{5}\right)^{\alpha_{ff}} + T_{syn_{5GHz}} \left(\frac{0.408}{5}\right)^{\alpha_{syn}} \qquad (6.14) \\ &= T_{ff_{5GHz}} \left(\frac{0.408}{5}\right)^{\alpha_{ff}} + (T_{b_{5GHz}} - T_{ff_{5GHz}}) \left(\frac{0.408}{5}\right)^{\alpha_{syn}} \\ &= T_{ff_{5GHz}} \left(\left(\frac{0.408}{5}\right)^{\alpha_{ff}} - \left(\frac{0.408}{5}\right)^{\alpha_{syn}}\right) + T_{b_{5GHz}} \left(\frac{0.408}{5}\right)^{\alpha_{syn}} \end{aligned}$$

By dividing both sides of the last expression by $T_{b_{5GHz}}$, we get:

$$\left(\frac{0.408}{5}\right)^{\alpha_{gal}} = \frac{T_{ff_{5GHz}}}{T_{b_{5GHz}}}\left(\left(\frac{0.408}{5}\right)^{\alpha_{ff}} - \left(\frac{0.408}{5}\right)^{\alpha_{syn}}\right) \tag{6.15}$$

If we now call:

$$f_{th_{5GHz}} = \frac{T_{ff_{5GHz}}}{T_{b_{5GHz}}} \tag{6.16}$$

then eq. (6.15) can be written as:

$$f_{th_{5GHz}} = \frac{1 - \left(\frac{0.408}{5}\right)^{\alpha_{gal}-\alpha_{syn}}}{1 - \left(\frac{0.408}{5}\right)^{\alpha_{ff}-\alpha_{syn}}} \tag{6.17}$$

Likewise, for the case at 408 MHz, we have:

$$f_{th_{408MHz}} = \frac{1 - \left(\frac{5}{0.408}\right)^{\alpha_{gal}-\alpha_{syn}}}{1 - \left(\frac{5}{0.408}\right)^{\alpha_{ff}-\alpha_{syn}}} \tag{6.18}$$

In particular, for α_{ff} and α_{syn} we have adopted the values -2.1 and -2.9 while α_{gal} is computed, for each pair of pixels, from:

$$\alpha_{gal} = log(T_{b_{5GHz}}/T_{b_{408MHz}})/log(408\ MHz/5\ GHz) \tag{6.19}$$

with $T_{b(\nu)} = T_{gal}(\nu) - T_{off}(\nu)$ according to eq. (6.1) and (6.4). Before illustrating the results of the application of eq. (6.19), we discuss the validity of eq. (6.17) and (6.18) with the assumption α_{ff}=-2.1 over the range 408 MHz – 5 GHz.

6.4.1 The optical thickness regime for free-free in the range 408 MHz - 5 GHz

A critical point of the analysis is the assessment of the physical conditions of the emitting ionized gas in the frequency range we are considering and, in particular, at 408 MHz. We recall from section 2.3.2 of Chapter 2 the expression for the optical thickness τ_{ν}^{ff} of thermal bremsstrahlung in the Altenhoff et al. [2] approximation. In CGS units, this is:

$$\tau_{\nu}^{ff} \simeq 0.08235 T_e^{-1.35} \nu_{GHz}^{-2.1} (EM/cm^{-6}pc) \tag{6.20}$$

If we assume a typical value for $T_e \simeq 8000$ K which is common to both the diffuse ionized gas and HII regions, we see clearly that τ_{ν}^{ff} depends strongly on the emission measure. EM is known to vary widely according to the form of ionized gas we are considering, i.e. diffuse gas or discrete, compact sources. For the diffuse gas, we use the reference

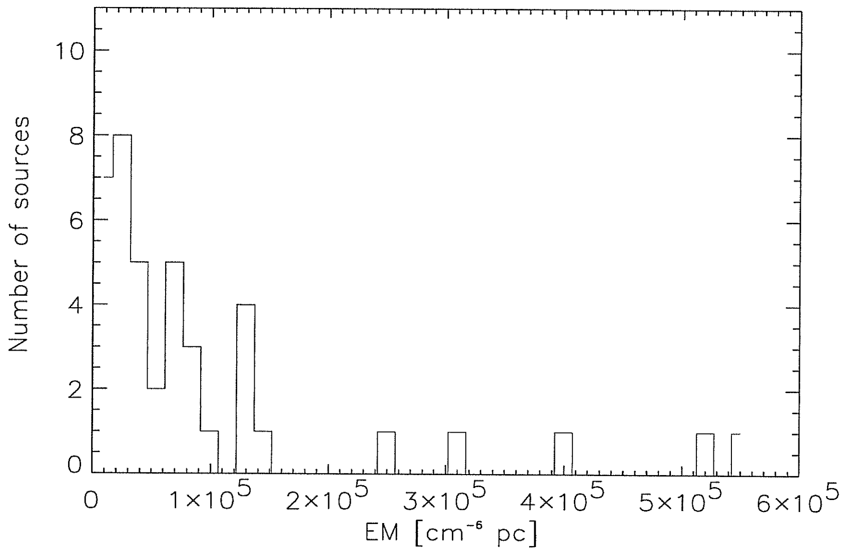

Figure 6.5: Emission measure distribution for 44 cataloged HII regions lying in the range $20^0 < l < 30^0$, $-1.5^0 < b < +1.5^0$. Data are from: Downes et al. [94]; Reifenstein et al. [252]; Wink et al. [346].

value reported by Reynolds [254] of $EM \simeq 9 - 23\ cm^{-6}\,pc$. For this, at 408 MHz we obtain from eq. (6.20) $\tau_\nu^{ff} \sim 2.6\times10^{-5}$ - 6.7×10^{-5} and the optical thin regime applies. As for HII regions, of the 102 sources lying in our selected coordinate range, 44 have an available estimate of the emission measure. The distribution of these values is shown in Fig. 6.5. Most of the sources appear to be characterized by an emission measure $EM \sim 10^4\ cm^{-6}\ pc$ and only a few appear to have higher values, of order of $\sim 10^5\ cm^{-6}\ pc$. In this range of emission measure, τ_ν^{ff} varies in the range $\sim 0.03 - 0.3$. Again, being $\tau_\nu^{ff} < 1$, the assumption α_{ff}=-2.1 is correct. Eq. (6.20) indicates that, at 408 MHz, τ_ν^{ff} is bigger than unity for values of the emission measure $\geq 10^6\ cm^{-6}\ pc$. As we have already discussed (Chapter 3, section 3.3.1), these values of EM tend to characterize mainly UCHII whose flux density at these frequencies is rather faint. In addition, from Fig. 6.5 it appears that none of the bright HII regions we are more likily to consider has such high values of emission measure. In summary, our adopted free-free spectral index appears to be correct over the frequency range 408 MHz – 5 GHz and the error which may be introduced in the analysis by neglecting the presence of UCHII in our region of the sky is assumed to be small.

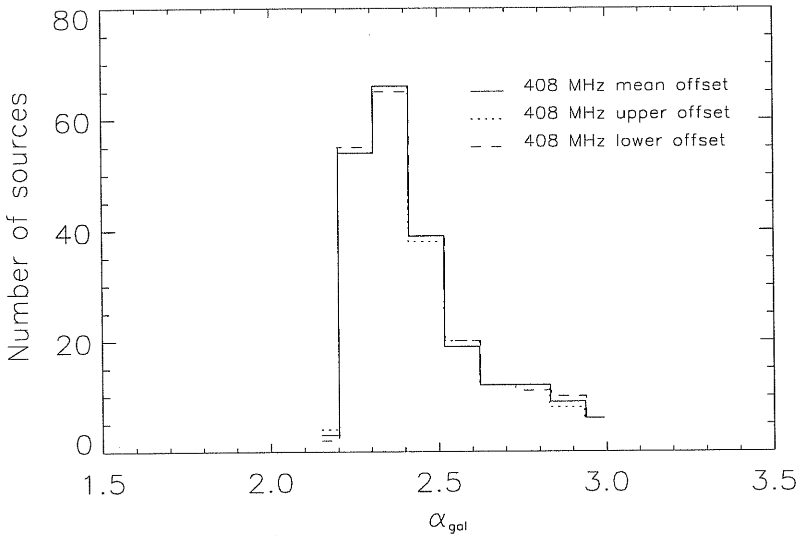

Figure 6.6: Galactic spectral index distribution between 408 MHz and 5 GHz. The distributions recovered assuming different values of the 408 MHz offset are shown. The mean value is (for all cases): $\overline{\alpha_{gal}} = 2.48 \pm 0.2$.

6.4.2 The galactic spectral indices and the component separation

By applying eq. (6.19) pixel by pixel, we obtain the spectral index distribution of Fig. 6.6. The figure has been obtained assuming, for the 408 MHz offset, the mean value 2.6 K as well as the upper and lower estimates we have derived from the T-T plots technique. Clearly, our assumption that the propagated error on the spectral index analysis due to the offset uncertainty would be negligible appears to be correct. The distribution, independently from the choice of the 408 MHz offset, has a mean value $\overline{\alpha_{gal}} = 2.48 \pm 0.2$. In the following, we assume $T_{off_{408MHz}}$=2.6 K. In Fig. 6.7 the variation of spectral index with latitude is also shown: clearly, there is a flattening of the spectral index towards the Galactic Plane. This effect is consistent with what expected since, in proximity of the plane, the contribution of thermal emission from compact HII regions becomes dominant making the galactic spectral index flatten. At the same time, at latitude $|b| \sim 1^0$, the synchrotron radiation becomes more intense than the diffuse thermal emission causing a steepening in the values of α_{gal}.

If we now apply eq. (6.17) and eq. (6.18), we can compute the fraction of thermal emission at 408 MHz and 5 GHz. Results of the calculation are shown in Fig. 6.8. The figures illustrate the variation of $f_{th_{408MHz}}$ and $f_{th_{5GHz}}$ with latitude. Following the same reasoning as for the spectral index case, the thermal fraction of the total emission appears to increase moving towards the plane.

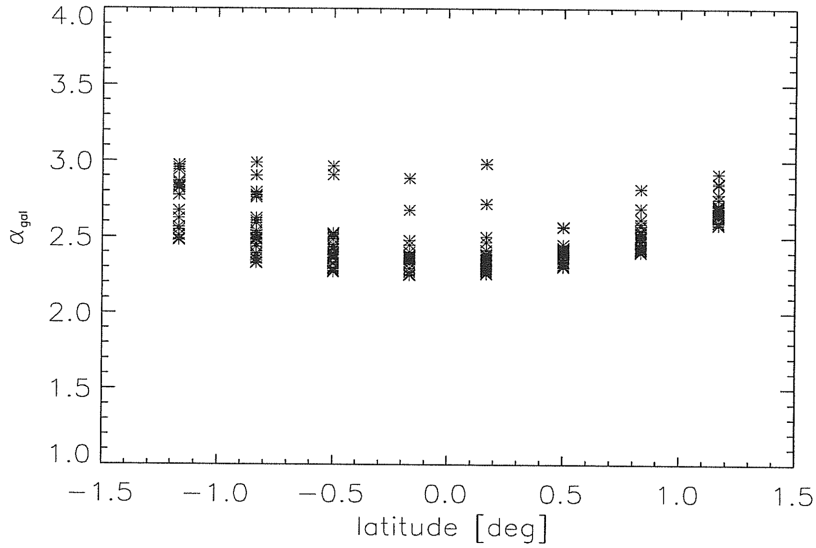

Figure 6.7: Galactic spectral index variation with latitude. Each plotted point – denoted with a cross – corresponds to a pixel. Different points at the same latitude refer to different longitudes in the range $20^0 < l < 30^0$.

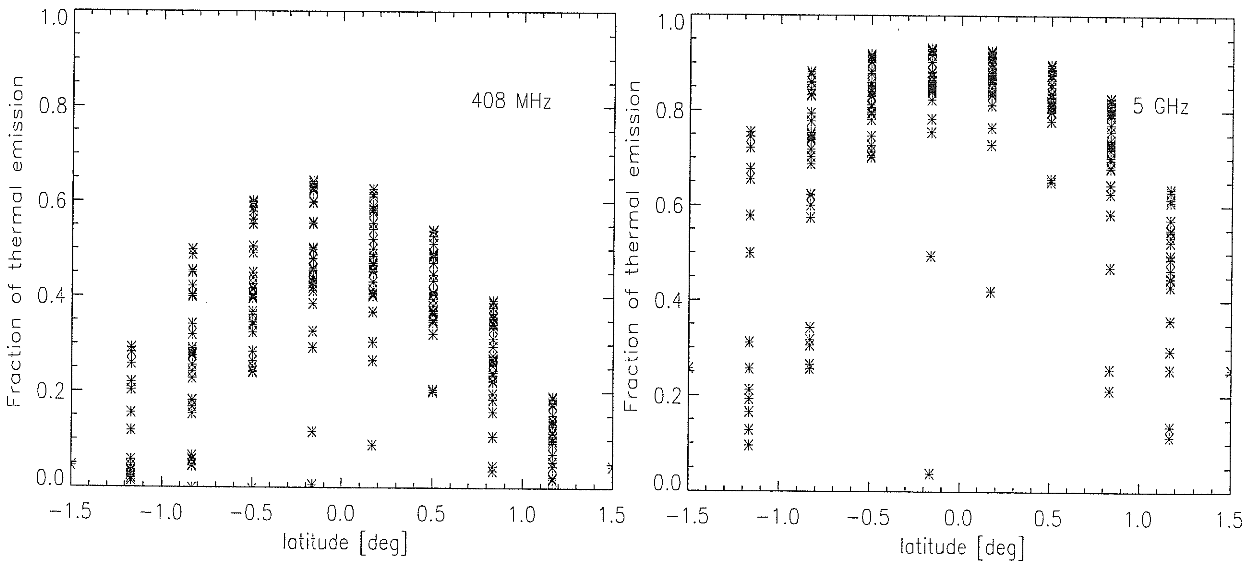

Figure 6.8: Fractions of thermal emission at 408 MHz (right panel) and 5 GHz (left panel). Clearly, the free-free becomes dominant in proximity of the plane where the thermal emission from HII regions is very intense.

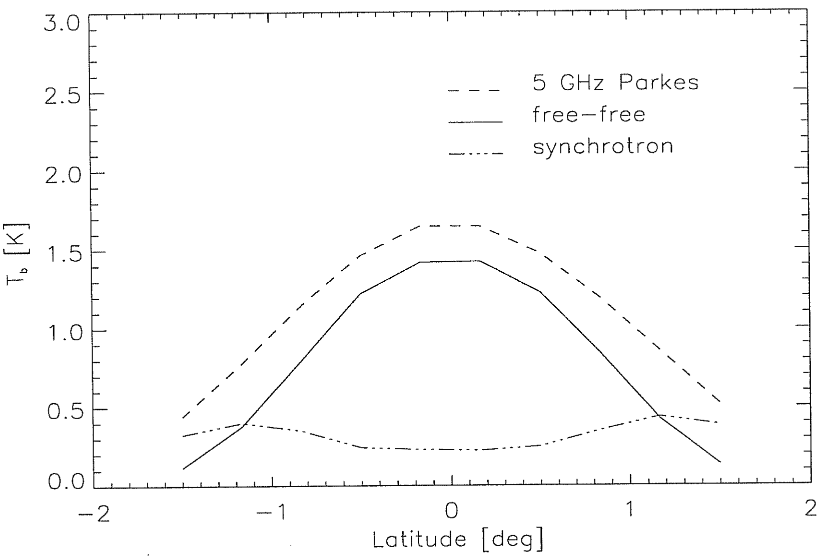

Figure 6.9: Latitude cuts for the total (dashed line), free-free (solid line) and synchrotron (dotted-dashed line) components for the 5 GHz Parkes survey. Clearly, the free free contribution is dominant within one degree from the Galactic Plane. At bigger latitudes, the synchrotron component becomes more intense.

6.5 The free-free component and the contribution from HII regions

Having an estimate, pixel by pixel, of the fraction of free-free, we can then proceed with the component separation for each considered frequency. Fig. 6.9 illustrates the outcome of the analysis in the 5 GHz case. Brightness temperature mean values are shown for each component obtained by averaging out the pixel data along strips 20′-wide in latitude.
As we have mentioned in the introduction, the purpose of this work is to compare the free-free distribution with the distribution of discrete HII regions and to give an estimate of the contribution provided by the latter to the total emission. For this purpose, from Fig. 6.9 we single out the free-free latitude cut and we perform a gaussian fit to the curve in order to evaluate its full-width-half-maximum. This turns out to be of order of ~ 1.7 degrees (Fig. 10, left panel). Analogously, after computing the latitude distribution of the 102 HII regions lying in our selected region of the sky, we consider the gaussian fit to this histogram. The HII region distribution appears to be much narrower – fwhm ~ 0.8 degrees – (Fig. 6.10, right panel) than its parent free-free distribution clearly revealing the presence of diffuse ionized gas in the thin layer. By exploiting the HII region simulated map at 5 GHz, smoothed to an angular resolution of 1.2^0 (see section 6.3), we can also estimate the contribution which they provide to the total emission budget. We obtain:

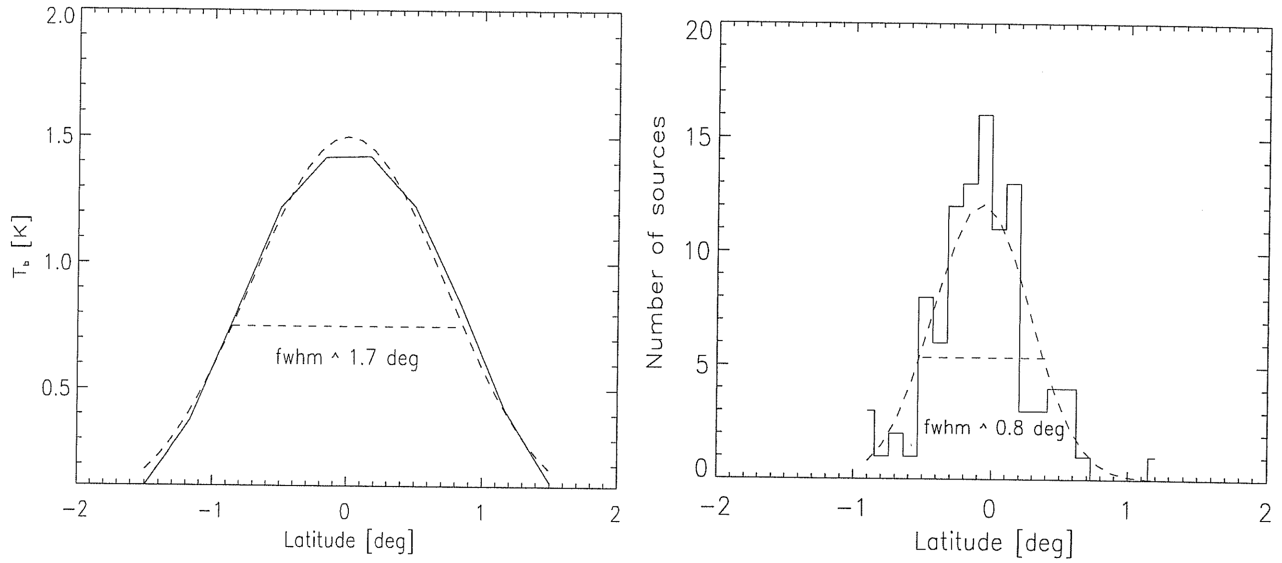

Figure 6.10: Left panel: free-free latitude cut at 5 GHz. The fwhm of the distribution is $\sim$ 1.7 degrees. Right panel: HII region latitude distribution. The fwhm of the distribution is $\sim$ 0.8 degrees.

$$\frac{\sum_{j=1}^{N} T_{b_{HII_j}}}{T_{b_{ff}}} \simeq 11\% \tag{6.21}$$

where N=102, $T_{b_{HII_j}}$ is the brightness temperature of the $j-th$ HII region provided by the simulated map and $T_{b_{ff}}$ is the total brightness temperature of the free-free component of the 5 GHz Parkes map as obtained in section 6.4.

6.6 Conclusions

We have presented the preliminary results of an analysis aimed at the investigation of the contribution of diffuse gas to the thin layer of warm ionized gas. For this purpose, we have realized a decomposition of the total radio emission into its free-free and synchrotron components. The analysis, which has been carried out in a selected region of the Galactic Plane ($20^0 < l < 30^0$, $-1.5^0 < b < +1.5^0$), has made use of data at 408 MHz and 5 GHz. The surveys have had their zero levels adjusted with auxiliary information at 2.3 GHz. The component separation method which has been applied has allowed the recovery of the Galactic spectral indices across the considered region of the sky. Latitude cuts made on the recovered free-free distribution and on the corresponding distribution of cataloged HII region has enabled to show, clearly, the presence of the diffuse component. An estimate of the HII region brightness contribution to the free-free emission budget has given a value $\sim 11\%$ indicating that also in the thin layer the diffuse gas is dominant with respect to discrete HII regions.

Conclusions

The spatial distribution of the Galactic warm ionized gas is characterized by a thin and a thick layer. The thin layer consists in ionized gas located in the proximity of the Galactic Plane while the thick layer corresponds to ionized gas which is situated well above the plane. The thin layer is contributed by discrete HII regions and diffuse gas. Current models (Miller & Cox [223]; Dömgorgen & Mathis [91]) tend to favour a scenario in which the presence of ionized gas in the thick layer is due to ultraviolet radiation leaking out of regions of star formation located in the thin layer. In the light of these models, an accurate knowledge of the physical properties of the thin layer is crucial for a global understanding of the mechanisms regulating the warm ionized gas.

Despite the important role played by the thin layer, no systematic investigation of it has been performed and no attempt of bringing together the widely spread available information on HII regions has been made. Consequently, our knowledge on this component has been based so far either on oversimplified analytical calculations or on scattered observational information which largely suffer from undersampling. For instance, the value which is commonly quoted as the HII region contribution to n_e along every line of sight at the midplane (0.015 cm^{-3}) has been obtained analytically from a statistical average of the population of nearby hot stars (i.e., less than 1 kpc from the Sun) and the Strömgren spheres they would produce in a uniform, high-density medium (Prentice & ter Haar [244]; Lyne et al. [204]). Following the argument by Miller & Cox [223], this value seems to overestimate the effective contribution of traditional HII regions due to the fact that their filling factor is expected to be small given the typical Strömgren radius of an O star in a high-density medium ($R_s \leq 50$ pc for a medium density $n \geq 1.0$ cm^{-3}). The scale height of the HII region distribution which is also usually reported (70 pc) is computed from the same analytical model.

At the same time, the Galactic electron density distribution has been synthesized, in most recent models (Cordes & Lazio [67], [68]), by adopting smoothly varying, large-scale components subsequently perturbed by small-scale under/over dense regions. However, as suggested by Cordes & Lazio [68], an alternative approach is to model the large-scale structure out of those clumps which are recognized to be the fundamental structures comprising the WIM, such as HII regions and shells and supershells. Yet, this second approach is feasible only when accurate information regarding the locations of these structures has been acquired. At present, electron density models rely mainly on pulsar dispersion and scattering measures for which the number of probed lines of sights does not allow to achieve such accuracy.

The arguments discussed above have motivated our work whose main results, together with its future perspectives, are outlined below.

A radio catalog of Galactic HII regions

We have collected radio data on Galactic HII regions from 24 published works and built a self-consistent database of 1442 sources. This work has resulted in the construction of what we have called Master Catalog which consists of 11 different sub-catalogs storing the original information from the source references. In particular, the sub-catalogs list flux densities and diameters as well as radio line velocities, line widths and line temperatures; errors are given on these quantities.

From this large data set observed at a range of frequencies and beamwidths, we have produced a readily accessible Synthetic Catalog giving the flux density, diameter and velocity (where available) at 2.7 GHz, the frequency where most data are given. Errors on these observed parameters have also been derived.

The Master Catalog and the Synthetic Catalog (which are publicly accessible via ftp at: cdsarc.u-strasbg.fr) are going to be constantly updated whenever new data of Galactic compact HII regions become available. At the same time, since the current version of the catalog does not include either ultra compact HII regions (UCHII) or extremely extended HII regions (EHE), we foresee an extension of the catalog to include also these classes of objects.

A full description of the catalog is given in: *A radio catalog of Galactic HII regions for applications from decimeter to millimeter wavelengths*, Paladini, R., Burigana, C., Davies, R., Maino, D., Bersanelli, M., Cappellini, B., Platania, Smoot, G., A&A, 397, 213, 2003

Spatial distribution of Galactic HII regions

We have analyzed the spatial distribution of 550 Galactic HII regions taken from the 2.7 GHz Synthetic Catalog, exploiting the extensive database of kinematic information contained in the catalog. For each source we have derived a galactocentric distance using the Fich et al. [106] rotation model.

Distances from the Sun have been unambiguously derived for 117 sources, lying either outside the solar circle (84) or on a line-of-sight tangential to their orbit (33). A highly significant correlation between luminosity and linear diameter was found for these sources. The corresponding least-square linear relationship in the log-log plane was used to resolve, at least in a statistical sense, the distance ambiguity for an additional 256 sources. The reliability of this approach was successfully tested comparing the distributions of solar distances, linear diameters and luminosities so obtained with those of sources with unambiguous distances.

An analysis of the z-distribution of HII regions has shown: an increase of the mean value of $|z|$ with R, for $R > R_0$, reflecting the shape of the warp; a corresponding increase of the width of the distribution as a function of R, comparable to what is seen for the OB stars and the molecular gas distribution; an azimuthally-averaged thickness of the HII region layer, $\sigma = 52\,\mathrm{pc}$, within the solar circle similar to that of OB stars but narrower than those of the diffuse HII and HI.

The robustness of our results have been checked by repeating the analysis adopting the extreme assumption that luminosities and linear diameters are totally independent. In this case we have used the mean linear diameter ($\overline{d} = 7.6\,\mathrm{pc}$) of sources with known solar distance as a distance indicator. The results for $R > R_0$ (and, in particular, the increase of $| < z > |$ and the thickening of the z-width with increasing R) are obviously unchanged since objects outside the solar circle are unaffected by the distance degeneracy. For $R < R_0$ we find $\sigma = 51.4\,\mathrm{pc}$, $< z >= -7.2\,\mathrm{pc}$, not significantly different from the values found using the correlation.

We have also confirmed, for a much larger sample, the positive gradient of electron temperature with galactocentric distance discovered in previously published works.

In addition, we have found that our recovered HII region 2-D distribution shows spiral-like structures, in acceptable agreement with the spiral arms delineated by the Taylor & Cordes [311] model.

Although a more detailed study of the spiral arm structure was beyond the goal of the analysis, it represents its natural development. In particular, we intend to investigate how the spiral structure results as areas of overdensities in the HII region distribution. An interesting topic we would like to tackle is also the relation between the spiral pattern and the underlying Galactic magnetic field for which a wealth of information is contained in rotation measures data.

This work is the content of: *Spatial distribution of Galactic HII regions*, Paladini, R., Davies, R., DeZotti, G., submitted to MNRAS

Applications of the HII region catalog

The HII region catalog appears to have many applications related to CMB mapping projects such as PLANCK. We have shown that, Galactic HII regions do not appear to impact severely on the accuracy of the recovery of the calibration factor and, at the same time, that individual compact bright HII regions have a role in relative calibration. In addition, we have seen that HII regions are useful as pointing and beamshape indicators and that the HII region Galactic distribution contribute to the straylight radiation without introducing a significant contamination. We have also pointed out the need of observations of HII regions at millimeter wavelengths for which the Catalog provides information for the selection of sources and estimates of flux densities. Finally, as part of an analysis of the polarized Galactic synchrotron emission, we have discussed the importance of considering the contribution of HII regions for a better understanding of the observed signal.

This vast data base can also be useful to address one of the still open questions related to regions of star formation, such as the interplay between the warm ionized gas and the dust. A way to tackle this problem is to study the relationship between the radio and the FIR/submm emission. This can be done by combining the radio data provided by the catalog with information at higher frequencies. Such kind of analysis, representing one of the developments of the present work, would enable us, on one side, to establish the turning point frequency where radiation emitted by dust becomes dominant with respect to the free-free produced by the ionized gas. At the same time, as far as the FIR/submm-part of the spectrum is concerned, it would be important to constrain crucial parameters of the dust like its temperature and the emissivity index which, in turn, determines the nature of the grain material.

The analysis described above is contained in the following papers:

Power spectrum of the polarized diffuse Galactic radio emission, Baccigalupi, C., Burigana, C., Perrotta, F., De Zotti, G., La Porta, L., Maino, D., Maris, M., Paladini, R., A&A, 372, 8, 2001

Trade-off between angular resolution and straylight contamination in CMB anisotropy experiments. II. Straylight evaluation, Burigana, C., Sandri, M., Villa, F., Maino, D., Paladini, R., Baccigalupi, C., Bersanelli, M., Mandolesi, R., submitted to A&A

Optimized in-flight calibration for extended CMB surveys, Cappellini, B., Maino, D., Albetti, G., Platania, P., Paladini, R., Mennella, A., Bersanelli, M., submitted to A&A

A preliminary analysis of the diffuse component in the thin layer

We have presented the preliminary results of an analysis of radio continuum data intended to disentangle the free-free radiation from other components of emission in order to study its physical properties (i.e. the thickness with respect to the plane) and estimate the contribution from compact HII regions. The analysis, which has been carried out in a selected region of the Galactic Plane ($20^0 < l < 30^0$, $-1.5^0 < b < +1.5^0$), has made use of data at 408 MHz (Haslam et al. [150]) and 5 GHz (Haynes et al. [151]). The surveys have had their zero levels adjusted with auxiliary information at 2.3 GHz. The component separation method which has been applied has allowed the recovery of the Galactic spectral indices across the considered region of the sky. Latitude cuts operated on the recovered free-free distribution and on the corresponding distribution of cataloged HII region has enabled us to show, clearly, the presence of the diffuse component. An estimate of the HII region brightness contribution to the free-free emission budget has retrieved a value $\sim 11\%$ indicating that also in the thin layer the diffuse gas is dominant with respect to discrete HII regions.

These results will be reported in: *Analysis of the diffuse component in the thin layer of Galactic warm ionized gas in the range:* $20^0 < l < 30^0$, $-1.5^0 < b < +1.5^0$, Paladini, R., DeZotti, G., Davies, R., in preparation

We foresee several developments in this area. First of all, along the lines followed for the HII region distribution, we would like to estimate the scale height of the diffuse gas in the thin layer. This parameter can be recovered according to the technique first worked out by Haffner et al. [139] for determining the scale height of the Hα emission in the direction of the Perseus arm. In practise, taking into account the dependence of the free-free emission on the emission measure and adopting a model of the electron density distribution, it is possible to convert the observed latitude-dependence of the radio continuum into a function of z, the distance from the Galactic Plane, thus deriving the scale height of the emitting gas.

The estimate so obtained can be further refined by repeating the analysis using information on the radio continuum at three rather than two frequencies. In particular, we would like to complement our 408 MHz and 5 GHz data with the 2.7 GHz Effelsberg 100-m data (Reich et al. [248]; Fürst et al. [115]; Reich et al. [251]) which are characterized by a resolution ($4.3'$) comparable to the 5 GHz Parkes data. The use of three frequencies allows, simultaneously, a more accurate determination of the ionized gas scale height and an estimate of the spatially varying Galactic synchrotron spectral index which, in the current work, was kept fixed.

We are also planning to conduct the same kind of analysis at higher frequencies, in addition to the already used 5 GHz Parkes data, the 10 GHz data by Handa et al. [145] at the angular resolution of $3'$ and the 61 GHz WMAP data obtained with a $20'$-beam. This is motivated by two main reasons: on one side, the improvement of the angular scale is useful for increasing the accuracy on the component separation and, as a consequence, on the scale height parameter. On the other side, from the comparison with the lower-frequency case, it is possible to retrieve important information on the nature of the emitting material. In fact, one of the most problematic topics regarding the warm ionized gas concerns the presence, in the Galaxy, of spinning dust grains whose continuum emission, according to theoretical models (Draine & Lazarian [95]), peaks in the 20–40 GHz region, so that our analysis over a broad frequency range would provide an important check of the validity of such models.

To conclude our discussion, it is important to remember that a new era is opening up for the understanding of the Galactic warm ionized gas. On one side, the current generation of Hα surveys such as the extensive WHAM and SHASSA and the on-going VTSS and MWFC projects is expected to improve of many orders our knowledge of the structure and kinematics of the ionized gas. Moreover, the potentiality of these surveys have been recently enhanced by the successful attempts of correcting the observed Hα emission for dust extiction.

At the same time, further crucial information will be provided by neutral hydrogen surveys. In fact, experiments such as the recently completed HIPASS[1] and the on-going

---

[1] The HI Parkes All Sky Survey (HIPASS) has been conducted on the Parkes 64-m telescope, operated by the Australia Telescope National Facility, between February 1997 and March 2000. HIPASS is the

HIJASS[2], although having being designed for mapping the large-scale distribution of HI density in the Universe, are characterized by sensitivities high enough to be capable of detecting also the very faint recombination lines signal due to the local, Galactic ionized gas. The information provided by these observations, unaffected by undersampling and extinction, is unique and can contribute, in an unprecedented way, to improve our current knowledge of this thermal phase of the interstellar gas.

---

deepest HI survey yet of the sky south of declination $+2^0$. Further information can be found in Barnes et al. [8].

[2] The HI Jodrell All Sky Survey (HIJASS) is a blind survey of neutral hidrogen of the northern sky, δ . 25^0, being conducted on the 76-m Lovell telescope at the Jodrell Bank observatory. For other information the reader is referred to Kilborn [183]

Appendix I

The Master Catalog contains the original data taken from the source references of Table 3.1 in Chapter 3. Due to the extensive amount of information, we have divided for convenience the Master Catalog into 11 sub-catalogs. We give hereafter the description of the structure of each of these compilations while, for a general overview about the content of the sub-catalogs, we refer the reader to section 3.3.1 of Chapter 3.
Each sub-catalog (except for Sub-catalog 1) has 37 columns and 1442 entries corresponding to the total number of sources. The columns are in order of increasing frequency of observation and, at each frequency, the columns are in alphabetical order of the references in Table 3.1. In all sub-catalogs, a null entry corresponds to no information available from the source reference.

Sub-catalog 1 lists only source coordinates, notes about the environment and radio/optical couterparts. For its content specificy, it presents a peculiar structure with respect to the other sub-catalogs. In details:
- Col. 1: source-numbering (records from 1 to 1442)
- Col. 2-3: Galactic coordinates, l and b
- Col. 4-6: celestial coordinates: RA - J2000
- Col. 7-9: celestial coordinate: DEC - J2000
- Col. 10: general remarks - C= complex field, S= strong source nearby, X=strong source nearby ($>$ 10 Jy), radio or optical counterpart. This flags follow the definitions given by Kuchar & Clark [188] according to which a source is in a complex field when there are two or more sources within either $2 \times \Theta_{obs}$ (i.e, four source radii) or $2 \times \Theta_{beam}$, whatever is larger [3], or with a strong and/or much stronger source nearby.

As for the counterpart in other wavebands, for the case of the radio identifications: Ke refers to Kesteven [182]; NRAO to Pauliny-Toth et al. [239]; W to Westerhout [341]; 3C to Third Cambridge Catalog (Bennett [15]) and 4C to Fourth Cambridge Catalog (Gower et al. [135] - Pilkington et al. [243]).
For the optical identifications, the Mársalková Catalog 1974 has been consulted. In this case: BBW refers to Bok-Bester-Wade [27]; DWB to Dickel-Wendker-Bieritz [86]; Ge (a) to Georgelin-Georgelin [122]; Ge (b) to Georgelin-Georgelin [123]; Ge (c) to Georgelin-Georgelin [124]; G to Gum [138]; H to Hoffleit [163]; RCW to Rodgers-Campbell-Whiteoak [266]; S to Sharpless [284] . Moreover, M stands for Messier Catalog;

---

[3] In Kuchar & Clark's paper, fluxes and angular sizes are measured directly from the survey images.

NGC for Dreyers'New General Catalog and IC for the Index Catalog.

Sub-catalog 2 to sub-catalog 11 have the following structure:
- Col. 1: source-numbering (records from 1 to 1442)
- Col. 2-3: Galactic coordinates, l and b
- Col. 4-6: celestial coordinates: RA - J2000
- Col. 7-9: celestial coordinate: DEC - J2000
- Col. 10-11: 1.4 GHz - Altenhoff et al. [3], Felli & Churchwell [102]
- Col. 12-23: 2.7 GHz - Altenhoff et al. [3], Beard [9], Beard & Kerr [10] , Beard et al. [11], Day et al. [78], Day et al. [79], Fürst et al. [114], Goss & Day [132], Reich et al. [249], Thomas & Day [318], Thomas & Day [318], Wendker [340]
- Col. 24: 3.9 GHz - Berlin et al. [18]
- Col. 25-26: 4.8 GHz - Kuchar & Clark [188]
- Col. 27-34: 5 GHz - Altenhoff et al. [3], Altenhoff et al. [4], Caswell & Haynes [53], Downes et al. [94], Mezger & Henderson [220], Reifenstein et al. [252], Wilson et al. [343], Wink et al. [346]
- Col. 35: 14.7 GHz - Wink et al. [347]
- Col. 36: 15 GHz - Wink et al. [346]
- Col. 37: 86 GHz - Wink et al. [346]

Note on sub-catalog 2 and sub-catalog 4: these sub-catalogs, including data on flux and angular diameters, always list values corrected for the instrument beam. Their complementary sub-catalogs are sub-catalog 3 and 5 quoting relative (%) errors.

Note on sub-catalog 6 to 11: these sub-catalogs list line velocity data. Observations may refer to frequencies other than those for the continuum data. In particular:
- Col. 25-26: Kuchar & Clark quote continuum data at 4.85 GHz and line data from Reifenstein et al. [252] and from Wilson et al. [343] at 5 GHz (H109α) and from Lockman [200] at 10 GHz (H85α, H87α and H88α)
- Col. 28: Altenhoff et al. [4] quotes continuum data at 5 GHz while line data are taken from Lockman [200] at 10 GHz (H85α, H87α and H88α)
- Col. 29-33: Caswell & Haynes [53], Downes et al. [94], Mezger & Henderson [220], Reifenstein et al. [252], Wilson et al. [343] quote both continuum and line data at 5 GHz (H109α, H110α)
- Col. 34-36-37: Wink et al. [346] quotes continuum data at 5/15/86 GHz and line data at 8.9/14.7 GHz (H90α and H76α).

Bibliography

[1] Abbott, D. C., ApJ **263** 723 (1982)

[2] Altenhoff, W., Mezger, P. G., Wendker, H., Westerhout, G., Veröff Sternwärte Bonn (1960)

[3] Altenhoff, W. J., Downes, D., Goad, L., Maxwell, A. & Rinehart, R., A&AS **1** 319 (1970)

[4] Altenhoff, W. J., Downes, D., Pauls, T. & Schraml, J., A&AS **35** 23 (1979)

[5] Andrew, B. H., MNRAS **132** 79 (1966)

[6] Armstrong, J. W., Rickett, B. J. & Spangler, S. R., ApJ **443** 209 (1995)

[7] Baccigalupi, C., Burigana, C., Perrotta, F., De Zotti, G., La Porta, L., Maino, D., Maris, M., Paladini, R., A&A **372** 8 (2001)

[8] Barnes, D. G., Staveley-Smith, L., de Block, W. J. G., et al., MNRAS **322** 486 (2001)

[9] Beard, M., Aust. J. Phys. **19** 141 (1966)

[10] Beard, M. & Kerr, F. J., Aust. J. Phys. **22** 121 (1969)

[11] Beard, M., Thomas, B. Mac. A. & Day, G. A., Aust. J. Phys. Ap. Suppl. **11** 27 (1969)

[12] Beck, R. Brandenburg, A., Moss, D., Shukurov, A. & Sokoloff, D., ARA&A **34** 155 (1996)

[13] Becker, R. H., White, R. L., Helfand, D. J. & Zoonematkermani, S., ApJS **91** 347 (1994)

[14] Bennett, C. L., Bay, M., Halpern, M. et al., ApJ **583** 1 (2003)

[15] Bennett, A. S., Mem. R. Astr. Soc. **68** 163 (1962)

[16] Bennett et al., astro-ph/0302207

[17] Berkhuijsen, E. M. & Wielebinski, R., A&A **34** 173 (1974)

[18] Berlin, A. B., Gol'nev, V. Y., Lipovka, N. M., Nizhel'skij, N. A. & Spangenberg, E. E., AZh **62** 229 (1985)

[19] Bersanelli, M., Muciaccia, P. F., Natoli, P., Vittorio, N., Mandolesi, N., A&ASS **121** 393 (1997)

[20] Binney, J. and Merrifield, M. R., *Galactic Astronomy* (1998)

[21] Bland-Hawthorn, J. & Maloney, P. R. PASA **14** 59 (1997)

[22] Bland-Hawthorn, J. & Maloney, P. R., ApJ **510** 33 (1999)

[23] Blitz L., APJ **231** 115 (1979)

[24] Blitz L., Fich, M. & Stark A. A., ApJS **49** 183 (1982)

[25] Bloemen, H., ARA&A **27** 469 (1989)

[26] Boggess, N. W., Mather, J. C., Weiss, R., et al., ApJ **397** 420 (1992)

[27] Bok, B. J., Bester, M. J., Wade, C. M., Daedalus, Harvard Reprint **416** 1 (1955)

[28] Brand J. & Blitz L., A&A **275** 67 (1993)

[29] Bregman, J. and Ashe, G. A., IAUS **144** 387 (1991)

[30] Braccesi, A., *Dalle stelle all'Universo*, ed. Zanichelli (2000)

[31] Bregman, J. N. & Harrington, J. P., ApJ **309** 833 (1986)

[32] Bregman, J. N., Kelson, D. D. and Ashe, G., A., ApJ **409** 682 (1993)

[33] Bregman, J. N., *The Interplay between Massive Star Formation, the ISM and Galaxy Evolution*, Conference Proceedings, ed. Kunth, D., Guiderdoni, B., Heydari-Malayeri, M. and Thuan, T. X. 211 (1996)

[34] Bregman, J., Parriott, J. and Rosen, A., Conference Proceedings, *Large Scale Motions in the ISM of Ellipticals and Spiral Galaxies*, ed. Franco, J. and Carraminana, A. 120 (1999)

[35] Breitschwerdt, D., Egger, R., Freyberg, M. J., Frisch, P. C. and Vallerga, J. V., Space Sci. Rev. **78** 183 (1996)

[36] Bridle, A. H., MNRAS **136** 219 (1967)

[37] Brisken, W. F., Benson, J. M., Goss, W. M. & Thorsett, S. E., ApJ **571** 906 (2002)

[38] Brocklehurst, M., MNRAS **157** 211 (1972)

[39] Brocklhurst, M. & Seaton, M. J., MNRAS **157** 179 (1972)

[40] Bronfman, L., Cohen, R. S., Alvarez, H., May, J. and Thaddeus, P., ApJ **324** 248 (1988)

[41] Bronfman, L., Casassus, S., May, J., Nyman, L.-A., A&A **358** 521 (2000)

[42] Burbidge, G., Gould, R. & Pottasch, S., ApJ **138** 945 (1963)

[43] Burigana, C., Maino, D., Gòrski, K.M. et al., A&A **373** 345 (2001)

[44] Burigana, C., Natoli, P., Vittorio, N., Mandolesi, N. & Bersanelli, M., Exp. Astron. **12/2** 87 (2002)

[45] Burigana, C., Sandri, M., Villa, F., Maino, D., Paladini, R., Baccigalupi, C., Bersanelli, M., Mandolesi, R., submitted to A&A

[46] Burn, B. J., MNRAS **133** 67 (1966)

[47] Burrows, D. N. and Mendenhall, J. A., Nature **351** 629 (1991)

[48] Burton, W. B., Gordon, M. A., Bania, T. M. and Lockman, F. J., ApJ **202** 30 (1975)

[49] Burton W. B., *Galactic and Extragalactic Radio Astronomy*, ed. Verchuur, G. L., & Kellermann, K. I., Springer-Verlag (1988)

[50] Cappellini, B., Maino, D., Albetti, G., Platania, P., Paladini, R., Mennella, A., Bersanelli, M., submitted to A&A

[51] Carroll, B. W. and Ostlie, D. A., *An introduction to Modern Astrophysics*, ed. Addison-Wesley (1996)

[52] Caswell J. L., Murray J. D., Roger R. S., Cole D. J., Cooke, D. J., A&A **45** 239 (1975)

[53] Caswell, J. L. & Haynes, R. F., A&AS **171** 261 (1987)

[54] Chatterjee, S., Cordes, J. M., Lazio, T. J. W., Goss, W. M., Fomalont, E. B. & Benson, J. M., ApJ **550** 287 (2001)

[55] Chiang, L.-Y., Christensen, P.R., Jorgensen, H.E. et al., A& **392** 368 (2002)

[56] Chini, R., Kreysa, E, Mezger, P. G., Gemuend, H.-P., A&A **154** 8 (1986)

[57] Churchwell E., Smith L. F., Mathis J., Mezger P. G., Huchtmeier W., A&A **70** 719 (1978)

[58] Ciardi, B., Bianchi, S. & Ferrara, A., MNRAS **331** 463 (2002)

[59] Clemens D. P., ApJ **295** 422 (1985)

[60] Clemens, D. P., Sanders, D. B. and Scoville, N. Z., ApJ **327** 139 (1988)

[61] Cohen R. S., Dame T. M., Thaddeus P., ApJS **60** 695 (1986)

[62] Collins, J. A. & Rand, R. J., ApJ **551** 57 (2001)

[63] Condon, J. J., ApJ **188** 279 (1974)

[64] Condon, J. J., Broderick, J. J. & Seielstad, G. A., AJ **97** 1064 (1989)

[65] Condon, J. J., Griffith, M. R. & Wright, A. E., AJ **106** 1095 (1993)

[66] Cordes, J., A&SS **278** 11 (2001)

[67] Cordes, J. M. & Lazio, T. J., astro-ph/0207156

[68] Cordes, J. M. & Lazio, T. J., astro-ph/0301598

[69] Cox, D. P. and Smith, B. W., APJL **189** L105 (1974)

[70] Cox, D. P., ApJ **245** 534 (1981)

[71] Cox, D. P. and Reynolds, R. J., ARA&A **25** 303 (1987)

[72] Cox, D. P., Conference Proceedings, *Overview of the Interstellar Medium: Supernova related issues*, ed. Roger, R. S. and Landecker, T. L., 73 (1988)

[73] Cox, D. P., IAU Colloq. 120, *Structure and Dynamics of the Interstellar Medium*, ed. Tenorio-Tagle, G., Moles, M & Melnick, J., 500 (1989)

[74] Cui, W., Sanders, W. T., McCammon, D., Snowden, S. L. and Womble, D. S., ApJ **468** 102 (1996)

[75] Dame, T. M., Ungerechts, H., Cohen, R. S., de Geus, E. J., Grenier, J., May, J., Murphy, D. C., Nyman, L.-A. and Thaddeus, P., ApJ **322** 706 (1987)

[76] Danese L., de Zotti G., di Tullio G., A&A **82** 322 (1980)

[77] Davies, R. D. & wilkinson, A., *Microwave Foregrounds*, ASP Conf. Ser. N. 181, ed. de Oliveira-Costa, A. & Tegmark, M. (1999)

[78] Day, G. A., Thomas, B. Mac. A. & Goss, W. M., Aust. J. Phys. Ap. Suppl. **11** 11 (1969)

[79] Day, G. A., Warne, W. G. & Cooke, D. J., Aust. J. Phys. Ap. Suppl. **13** 11 (1970)

[80] de Amici, G., Bensadoun, M., Bersanelli, M., Kogut, A., Levin, S., Smoot, G. F., Witebsky, C., ApJ **359** 219 (1990)

[81] de Bernardis, P., Ade, P. A. R., Bock, J. J., et al., Nature **404** 955 (2000)

[82] de Jong, T., Boland, W. and Dalgarno, A., A&A **91** 68 (1980)

[83] Dennison, B, Simonetti, J. H. and Topsana, G. A., Publ. Astron. Soc. Aust. **15** 147 (1998)

[84] de Vaucouleurs, G., AnAP **11** 247 (1948)

[85] De Zotti, G., Toffolatti, L. Argüeso Gomez, F., et al., *3K Cosmology*, AIP Conf. Proc., 476, p. 204 (1999)

[86] Dickel, H. R., Wendker, H., Beiritz, J. H., A&A **1** 270 (1969)

[87] Dickey, J. M. and Lockman, F. J., ARA&A **28** 215 (1990)

[88] Dickinson, C., Davies, R. D. & Davis, R. J., astro-ph/0302024

[89] Digel S. W., PhD Thesis, Harvard University (1991)

[90] Diplas, A. and Savage, B. D., ApJ **377** 126 (1991)

[91] Domgörgen, H. & Mathis, J. S., ApJ **428** 647 (1994)

[92] Dove, J. B. & Shull, J. M., ApJ **430** 222 (1994)

[93] Downes, D., AJ **76** 305 (1971)

[94] Downes, D., Wilson, T. L., Bieging, J. & Wink, J., A&AS **40** 379 (1980)

[95] Draine, B. T. & Lazarian, A., ApJ **494** 19 (1998)

[96] Duncan, A. R., Stewart, R. T., Haynes, R. F. & Jones, K. L., MNRAS **277** 36 (1995)

[97] Duncan, A. R., Haynes, R. F., Jones, K. L., Stewart, R. T., MNRAS **291** 279 (1997)

[98] Duncan, A. R., Haynes, R. F., Reich, W., Reich, P., Gray, A. D., MNRAS **291** 279 (1998)

[99] Elmergreen, B. G. & Falgarone, E., ApJ **471** 816 (1996)

[100] Elmergreen, B. G., ApJ **477** 196 (1997)

[101] Epchtein, N., de Batz, B., Copet, E., et al., Ap&SS **217** 3 (1994)

[102] Felli, M. & Churchwell,E., A&AS **5** 369 (1972)

[103] Ferriere, K. M. & Schmitt, D., A&A **358** 125 (2000)

[104] Ferriere, K. M., RvMP **73** 1031 (2001)

[105] Fich, M. & Blitz, L., ApJ **279** 125 (1984)

[106] Fich M., Blitz L., Stark A. A., ApJ **342** 272 (1989)

[107] Field, G. B., Goldsmith, D. W. and Habing, H. J., ApJL **155** L149 (1969)

[108] Finkbeiner, D. P., Davis, M. & Schlegel, D. J., ApJ **524** 867 (1999)

[109] Finkbeiner, D. P., astro-ph/0301558

[110] Fixsen, D. J., Cheng, E. S., Gales, J. M., Mather, J. C., Shafer, R. A., Wright, E. L., ApJ **473** 576 (1996)

[111] Frail, D. A. & Weisberg, J. M., AJ **100** 734 (1990)

[112] Frail, D. A., Cordes, J. M., Hankins, T. H. & Weisberg, J. M., ApJ **382** 168 (1991)

[113] Frail, D. A., et al., ApJL **427** 43 (1993)

[114] Fürst, E., Handa, T., Reich, W., Reich, P. & Sofue, Y., A&AS **69** 403 (1987)

[115] Fürst, E., Reich, W., Reich, P. & Reif, K., A&AS **85** 691 (1990)

[116] Fürst, E., Reich, W., Reich, P. & Reif, K., A&AS **85** 805 (1990)

[117] Gardner, F. F. & Whiteoak, J. B., ARA&A **4** 245 (1966)

[118] Gatley, I., Becklin, E. E., Sellgren, K., Werner, M. W., ApJ **233** 575 (1979)

[119] Gaustad, J. E., McCullough, P. R., Rosing, W. R. and Buren, D. V., PASP **113** 1326 (2001)

[120] Gaylord, M. J., MNRAS **211** 149 (1984)

[121] Gear, W. K., Robson, E. I., Griffin, M. J., MNRAS **231** 55 (1988)

[122] Georgelin, Y. M. & Georgelin, Y. P., A&AS **6** 349 (1970)

[123] Georgelin, Y. M. & Georgelin, Y. P., A&AS **7** 133 (1970)

[124] Georgelin, Y. M. & Georgelin, Y. P., A&AS **3** 1 (1970)

[125] Georgelin, Y. M. & Georgelin, Y. P., A&AS **49** 57 (1976)

[126] Goldsmith, D. W., Habing, H. J. and Field, G. B., ApJ **158** 173 (1969)

[127] Goldsmith, P. F., *Interstellar Processes*, ed. Hollenbach, D. J. and Thronson Jr., H. A. 51 (1987)

[128] Gordon M.A., ApJ **316** 258 (1987)

[129] Gordon, M., *Galactic and Extragalactic Radio Astronomy*, ed. Verschuur, G. L. & Kellermann, K. I. (1988)

[130] Górski K.M., Hivon E. & Wandelt B.D., *Proceedings of the MPA/ESO Conference on Evolution of Large-Scale Structure: from Recombination to Garching*, ed. Banday, A.J., Sheth, R.K., Da Costa, L., N. 37 (1998)

[131] Goss W. M. & Radhakrishnan V., AstL. **4** 199 (1969)

[132] Goss, W. M. & Day, G. A., Aust. J. Phys. Ap. Suppl. **13** 3 (1970)

[133] Gottesman, S. T. & Gordon, M. A., ApJ **162** 93 (1970)

[134] Gordon, M. A. & Cato, T., ApJ **176** 587 (1972)

[135] Gower, J. F. R., Scott, P. F., Wills, D., Mem. R. Astro. Soc. **71** 49 (1967)

[136] Grabelsky, D. A., Cohen, R. S., Bronfman, L. and Thaddeus, P., ApJ **315** 122 (1987)

[137] Green, D. A., *A Catalog of Galactic Supernova Remnants (2000 August version)*, Mullard Radio Astronomy Observatory, Cavendish Laboratory, Cambridge, UK (2000)

[138] Gum, C. S., *Memoirs* RAS **67** 155 (1955)

[139] Haffner, L. M., Reynolds, R. J. and Tufte, S. L., ApJ **523** 223 (1999)

[140] Han, J. L. & Qiao, G. J., *The Cosmic Dynamo*, IAU Symposium N. 157, ed. Krause, F., Rädler, K. H. & Rüdiger, G., p. 279 (1994)

[141] Han, J. L. & Qiao, G. J., A&A **288** 759 (1994)

[142] Han, J. L., Manchester, R. N., Berkhuijsen, E. M. & Beck, R., A&A **322** 98 (1997)

[143] Han, J. L., Manchester, R. N. & Qiao, G. J., MNRAS **306** 371 (1999)

[144] Hanany, S. et al., ApJ **545** 5 (2000)

[145] Handa, T., Sofue, Y., Nakai, N., Hirabayashi, H., Inoue, M., PASJ **39** 709 (1987)

[146] Harding, D. S. and Harding, A. K., ApJ **257** 603 (1982)

[147] Hartmann, J., ApJ **19** 268 (1904)

[148] Hart, L. & Pedlar, A., MNRAS **176** 547 (1976)

[149] Haslam, C. G. T., Quigley, M. J. S., Salter, C. J., MNRAS **147** 405 (1970)

[150] Haslam, C. G. T., Salter, C. J., Stoffel, H. & Wilson, W., A&AS **47** 1 (1982)

[151] Haynes, R. F., Caswell, J. L., Simons, L. W. J., Aust. J. Phys. Astrophys. Suppl. **45** 1 (1978)

[152] Heiles, C., ApJ **208** 137 (1976)

[153] Heiles, C., ApJ **229** 533 (1979)

[154] Heiles, C., ApJS **55** 585 (1984)

[155] Heiles, C., ApJ **315** 555 (1987)

[156] Heiles, C., ApJ **354** 483 (1990)

[157] Heiles, C., ApJ **462** 316 (1996)

[158] Heiles, C., ApJ **551** 105 (2001)

[159] Henderson, A. P., Jackson, P. D. and Kerr, F. J., ApJ **263** 116 (1982)

[160] Heyer, M. H., *New Perspectives on the Interstellar Medium*, Astronomical Society of the Pacific Conference Series, ed. Taylor, A. R., Landecker, T. L. and Joncas, G., **168** 55 (1999)

[161] Hewish, A., Bell, S. J., Pilkington, J. D. H., Scott, P. F. & Collins, R. A., Nature **217** 709 (1968)

[162] Hirabayashi, H., *Galactic Radio Astronomy*, Proceedings from IAUS Symposium, ed. Kerr, F. J. & Simonson, S. C., **60** 353 (1974)

[163] Hoffleit, D., Ann. Harv. Coll. Observ. **119** 37 (1953)

[164] Hogg, D. W., ApJ **121** 1207 (2001)

[165] Hollenbach, D. J. and Salpeter, E. E., ApJ **163** 155 (1971)

[166] Hollenbach, D. J. and Tielens, A. G G. A., Rev. Mod. Phys. **71** 173 (1999)

[167] Howell, T. F., ApL **6** 45 (1970)

[168] Hurwitz, M. and Bowyer, S., ApJ **465** 296 (1996)

[169] Inoue, M. & Tabara, H., PASJ **33** 603 (1981)

[170] Israel, F. P. & van der Kruit, P. C., A&A **32** 363 (1974)

[171] Jackson, P. D. & Kerr, F. J., ApJ **196** 723 (1971)

[172] Jenkins, E. B., ApJ **219** 845 (1978)

[173] Jenkins, E. B., ApJ **220** 107 (1978)

[174] Jonas, J. L., Baart, E. E. & Nicolson, G. D., MNRAS **297** 977 (1998)

[175] Jonas, J. L., PhDT (1999)

[176] Jones, E. M., ApJ **182** 559 (1973)

[177] Kamaya, H., Mineshiga, S., Shibata, K. and Matsumoto, R., ApJ **458** 25 (1996)

[178] Kardashev, N. S., Soviet Astr. **3** 813 (1959)

[179] Keating, B., Timbie, P., Polnarev, A., Steinberg, J., ApJ **459** 580 (1998)

[180] Kerr F. J. & Knapp G. R., AuJPA **18** 9 (1970)

[181] Kerr, F. J. and Lynden-Bell, D., MNRAS **221** 1023 (1986)

[182] Kesteven, M. J. L., Aust. J. Phys. bf 21 369 (1968)

[183] Kilborn, V. A., *Seeing Through the Dust: The Detection of HI and the Exploration of the ISM in Galaxies*, ASP Conference Proceedings, N. 276, ed. Taylor, A. R., Landecker, T. L., Willis, A. G., p. 80

[184] Kleinmann, S. G., *Robotic Telecopes in the 1990s*, Asp Cof. Ser., N. 203 (1992)

[185] Kogut, A., Banday, A. J., Bennett, C. L., Gorski, K. M., Hinshaw, G., Reach, W. T., ApJ **460** 1 (1996)

[186] Kovac, J. M., Leitch, E. M., Pryke, C., Carlstrom, J. E., Halverson, N. W., Holzapfel, W. L., Nature **420** 772 (2002)

[187] Kuchar T. A. & Bania T. M., ApJ **436** 117 (1994)

[188] Kuchar, T. A. & Clark, F. O., ApJ **488** 224 (1997)

[189] Kulkarni, S. R., Blitz, L. and Heiles, C., ApJL **259** L63 (1982)

[190] Kulkarni, S. R. & Fich, M., ApJ **289** 792 (1985)

[191] Kulkarni, S. R. and Heiles, C., *Interstellar Processes*, ed. Hollenbach, D. J. and Thronson Jr., H. A., 87 (1987)

[192] Kurtz, S., Churchwell, E., Wood, D. O. S., ApJS **91** 659 (1994)

[193] Larson, R. B., MNRAS **194** 809 (1981)

[194] Lawson, K. D., Mayer, C. J., Osborne, J. L., Parkinso, M. L., MNRAS **225** 307 (1987)

[195] Lee, L. C. & Jokipii, J. R., ApJ **206** 735 (1976)

[196] Leitch, E. M. et al., ApJ **568** 28 (2002)

[197] Lockman, F. J., ApJ **209** 429 (1976)

[198] Lockman, F. J., ApJ **283** 90 (1984)

[199] Lockman, F. J., Hobbs, L. M. & Shull, J. M., ApJ **301** 380 (1986)

[200] Lockman, F. J., ApJS **71** 469 (1989)

[201] Lockman, F. J., Pisano, D. J. & Howard, G. J., ApJ **472** 173 (1996)

[202] Lockman, F. J., *Seeing Through the Dust: the Detection of HI and the Exploration of the ISM in Galaxies*,
ed. Taylor, A. R., Landecker, T. and Willis, A., ASP 2002

[203] Lynds, B. T., AJ **85** 1046 (1980)

[204] Lyne, A. G., Manchester, R. N., Taylor, J. H., MNRAS **213** 613 (1985)

[205] Malhotra S., ApJ **448** 138 (1995)

[206] Manchester, R. N. and Taylor, J. H., AJ, **86** 1953 (1981)

[207] Mandolesi, R., Bersanelli, M., Burigana, C., Gorsko, K. M., Hivon, E., Maino, D., Valenziano, L., Villa, F., White, M., A&AS **145** 323 (2000)

[208] Màrsalkovà, P., A&SS **27** 3 (1974)

[209] Martin, P. G., ApJS **66** 125 (1988)

[210] Martin, C. L., ApJ **491** 561 (1997)

[211] Mason, B., CBI collaboration, AAS **199** 3402 (2001)

[212] Mathis, J. S., ApJ **301** 423 (1986)

[213] May J., Murphy D. C., Thaddeus P., A&A **73** 51 (1988)

[214] McCammon, D., Burrows, D. N., Sanders, W. T. & Kraushaar, W. L., ApJ **269** 107 (1983)

[215] McCammon, D. and Sanders, W. T., ARA&A **28** 657 (1990)

[216] McCray, R. and Snow, T. P. Jr., ARA&A **17** 213 (1979)

[217] McKee, C. F. and Ostriker, J. P., ApJ **218** 148 (1977)

[218] McKee, C. F., Conference Proceedings, *Fountains, Bubbles and Hot Gas*, ed. Hold, S. S. and Verter, F. **278** 499 (1993)

[219] Menzel, D. H., Nature **218** 756 (1968)

[220] Mezger, P. G. & Henderson, A. P., ApJ **147** 471 (1967)

[221] Mihalas, D. and Binney, J., *Galactic Astronomy: Structure and Kinematics* (1981)

[222] Miller J. S., ApJ **151** 473 (1968)

[223] Miller, W. W. & Cox, D. P., ApJ **417** 579 (1993)

[224] Mills, B. Y. & aller, L. H., Aust. J. Phys. **24** 609 (1971)

[225] Mitra, D., Wielebinski, R., Kramer, M., Jessner, A., A&A **403** 585 (2003)

[226] Murai, T. and Fojimoto, M., PASJ **32** 581 (1980)

[227] Norman, C. A. and Ikeuchi, S., ApJ **345** 372 (1989)

[228] Norman, C. A. & Ferrara, A., ApJ **467** 280 (1996)

[229] Novikov, I. D. & Thorne, K. S., Black Holes, Les Houches, Eds. C. DeWitt., Gordon and Breach, New York (1973)

[230] Olling, R. P. and Merrifield, M. R., MNRAS **297** 943 (1998)

[231] Olling, R. P. and Merrifield, M. R., MNRAS **311** 361 (2000)

[232] Oort, J. H., Kerr, F. J. and Westerhout, G., MNRAS **118** 379 (1958)

[233] Oren, A. L. & Wolfe, A. M., ApJ **445** 624 (1995)

[234] Oster, L., Rev. Mod. Phys. **33** 525 (1961)

[235] Osterbrock, D. E., *Astrophysics of Gaseous Nebulae and Active Galactic Nuclei*, Mill Valley (1989)

[236] Panagia, N. & Terzian, Y., ApJ **287** 315 (1984)

[237] Pangelly, R. M., MNRAS **127** 145 (1964)

[238] Pauliny-Toth, I. I. K. & Shakeshaft, J. R., MNRAS **124** 61 (1962)

[239] Pauliny-Toth, I. I. K., Wade, C. M., Heeschen, D. S., ApJS **13** 65 (1966)

[240] Peacock, J. A., *Cosmological Physics*, ed. Cambridge University Press (1999)

[241] Penzias, A. A.; Wilson, R. W., ApJ **146** 666 (1966)

[242] Perek, L. & Kohoutek, L., *Catalog of Galactic Planetary Nebulae*, Academia, Prague (1967)

[243] Pilkington, J. D. H. & Scott, P. F., Mem. R. Astr. Soc. **69** 183 (1965)

[244] Prentice, A. J. & ter Haar, D., MNRAS **146** 423 (1969)

[245] Rand, R. J. & Kulkarni, S. R., ApJ **343** 760 (1989)

[246] Rand, R. J. & Lyne, A. G., MNRAS **268** 497 (1994)

[247] Reed B. C., PASP **109** 1145 (1997)

[248] Reich, W., Fürst, E., Haslam, C. G. T., Steffen, P. & Reif, K., A&AS **58** 179 (1984)

[249] Reich, W., Fürst, E., Reich, P., Sofue, Y. & Handa, T., A&A **155** 185 (1986)

[250] Reich, P. & Reich, W., A&AS **74** 7 (1988)

[251] Reich, W., Fürst, E., Reich, P. & Reif, K., A&AS **85** 633 (1990)

[252] Reifenstein, E. C., Wilson, T. L., Burke, B. F., Mezger, P. G. & Altenhoff, W. J., A&A **4** 357 (1970)

[253] Reynolds, R. J., ApJ **236** 153 (1980)

[254] Reynolds, R. J., ApJ **268** 698 (1983)

[255] Reynolds, R. J., ApJ **282** 191 (1984)

[256] Reynolds, R. J., ApJ **294** 256 (1985)

[257] Reynolds, R. J., ApJ **298** 27 (1985)

[258] Reynolds, R. J., ApJ **323** 118 (1987)

[259] Reynolds, R. J., ApJL **349** L17 (1990)

[260] Reynolds, R. J., *The Interstellar Disk-Halo Connection in Galaxies*, ed. Bloemen, H. IAU Symposium **144** 67 (1991)

[261] Reynolds, R. J. and Tufte, S. L., ApJL **439** L17 (1995)

[262] Reynolds, R. J., Tufte, S. L., Haffner, L. M., Jaehnig, K. and Percival, J. W., PASA **15** 14 (1998)

[263] Reynolds, R. J., Haffner, L. M., Tufte, S. L., *New Perspectives on the Interstellar Medium*, ASP Conf. Series, Vol. 168, ed. Taylor, A. R. Landecker, T. L., Joncas, G., (1999)

[264] Reynolds, R. J., Haffner, L. M. and Madsen, G. J., *Galaxies: The Third Dimension*, ASP Conf. Series, Vol. 282, ed. Rosado, M., Binette, L. and Arias, L., (2002)

[265] Rickett, B. J., ARA&A **28** 561 (1990)

[266] Rodgers, A. W., Campbell, C. T. & Whiteoak, J. B., MNRAS **121** 103 (1960)

[267] Roesler, F. L., Reynolds, R. J., Scherb, F. and Ogden, P. M., *High Resolution Spectroscopy*, ed. Hack, M., p. 600., (1978)

[268] Rohlfs, K., *Tools of Radio Astronomy* , Ed. Springer & Verlag, Berlin (1990)

[269] Ryba, M. F. & Taylor, J. H., ApJ **371** 739 (1991)

[270] Savage, B. D., Sembach, K. R. and Lu, L., AJ **113** 2158 (1997)

[271] Savage, B. D., et al., ApJL, **538** L27 (2000)

[272] Schaerer, D. & De Koter, A., A&A **322** 598 (1997)

[273] Scheuer, P. A. G., *Proc. Cambridge Philos. Soc.* **53** 764 (1957)

[274] Schlegel, D. J., Finkbeiner, D. P. & Davis, M., ApJ **500** 525 (1998)

[275] Schmidt M., *Galactic Structure*, ed. Blaauw, A. & Schmidt, M., University of Chicago Press, p. 513

[276] Schwartz P.R., ApJ **252** 589 (1982)

[277] Sciama, D. W., ApJ **364** 549 (1990)

[278] Sciama, D. W., ApJ **409** 25 (1993)

[279] Scott, P. F., MNRAS

[280] Scoville, N. Z. and Solomon, P. M., ApJL **199** L105 (1975)

[281] Sembach, K. R. and Savage, B. D., ApJS **83** 147 (1992)

[282] Shapiro, P. R. and Field, G. B., ApJ **205** 762 (1976)

[283] Sharpless, S., ApJ **118** 362 (1953)

[284] Sharpless, S., ApJS **4** 257 (1959)

[285] Shaver, P. A., Pramana **5** 1 (1975)

[286] Shaver, P. A., A&A **91** 279 (1980)

[287] Shaver P. A, Retallack D. S., Wamsteker W., Danks, A. C., A&A **102** 225 (1981)

[288] Shaver P. A., McGee R. X., Newton L. M., Danks A. C., Pottasch S. R., MNRAS **204** 53 (1983)

[289] Shull, J. M. and Beckwith, S., ARA&A **20** 163 (1982)

[290] Sidher, S. D., Sumner, T. J., Quenby, J. J., Gambhir, M, A&A **305** 308 (1996)

[291] Simard-Normandin, M. & Kronberg, P. P., ApJ **242** 74 (1980)

[292] Sironi, G., MNRAS **166** 345 (1974)

[293] Sironi, G.; Bonelli, G., ApJ **311** 418 (1986)

[294] Sivan, J., P., A&AS **16** 163 (1974)

[295] Slavin, J. D. and Cox, D. P., AAS **188** 4403 (1996)

[296] Smoot, G. F., De Amici, G., Friedman, S. D., Witebsky, C., Sironi, G., et al., ApJL **291** 23 (1985)

[297] Smoot, G. F. et al., ApJ **396** 1 (1992)

[298] Snowden, S. L., Cox, D. P., McCammon, D. and Sanders, W. T., ApJ **354** 211 (1990)

[299] Snowden, S. L., Mebold, U., Hirth, W., Herbstmeier, U. and Schmitt, J. H. M. M., Science **252** 1529 (1991)

[300] Snowden, S. L., Hasinger, G., Jahoda, K., Lockman, F. J., McCammon, D. and Sanders, W. T., ApJ **430** 601 (1994)

[301] Snowden, S. L., Egger, R., Finkbeiner, D. P., Freyberg, M. J., Plucinsky, P. P., ApJ **493** 715 (1998)

[302] Sokoloff, D. D., Bykov, A. A., Shukurov, A. et al., MNRAS **299** 189 (1998)

[303] Spangler, S. R. & Reynolds, R. J., ApJ **361** 116 (1990)

[304] Spitzer, L. Jr., ApJ **124** 20 (1956)

[305] Spitzer, L., *Physical Processes in the Interstellar Medium*, New York, Wiley **156** (1978)

[306] Spitzer, L. Jr., ARA&A **28** 71 (1990)

[307] Staggs, S. T., Gundersen, J. O., Church, S. E., *Microwave Foregrounds*, ASP Conf. Ser, N. 181, ed. de Oliveira-Costa, A. & Tegmark, M. (1999)

[308] Stark A. A. & Brand J., ApJ **339** 763 (1989)

[309] Struve, O. and Elvey, C. T., ApJ **88** 364 (1938)

[310] Tasker, N. J., Condon, J. J., Wright, A. E. & Griffith, M. R., AJ **107** 2115 (1994)

[311] Taylor, J. H. and Cordes, J. M., ApJ **411** 674 (1993)

[312] Taylor, J. H., Manchester, R. N. & Lyne, A. G., ApJS **88** 529 (1993)

[313] Taylor, A. R., Goss, W. M., Coleman, P. H., Van Leeuwen, J. & Wallace, B. J., ApJS **107** 329 (1996)

[314] Tegmark, M., Eisenstein, D. J., Hu, W., de Oliveira-Costa, A., ApJ **530** 133 (2000)

[315] Tenorio-Tagle, G. and Bodenheimer, P., ARA&A **26** 145 (1988)

[316] Tenorio-Tagle, G., Rozyczka, M. and Bodenheimer, P., A&A **237** 207 (1990)

[317] Thomas, B. & Day, G., Aust. J. Phys. Ap. Suppl. **11** 3 (1969)

[318] Thomas, B. & Day, G., Aust. J. Phys. Ap. Suppl. **11** 19 (1969)

[319] Thomson, R. C. & Nelson, A. H., MNRAS **191** 863 (1980)

[320] Thuan, T. X., ApJ **198** 307 (1975)

[321] Torres-Peimbert, S., Lazcano-Araujo, A. & Peimbert, M., ApJ **191** 401 (1974)

[322] Tufte, S. L., *The WHAM Spectrometer: Design, Performance Characteristics and First Results*, PhD Thesis, University of Wisconsin, Madison (1997)

[323] Turtle, A. J., Pugh, J. F., Kenderdine, S., Pauliny-Toth, I. I. K., MNRAS **124** 297 (1962)

[324] Uyaniker, B., Fürst, E., Reich, W., Reich, P., Wielebinski, R., A&AS **132** 401 (1998)

[325] Uyaniker, B., Fürst, E., Reich, W., Reich, P., Wielebinski, R., A&AS **138** 31 (1999)

[326] Vallée J. P., ApJ **454** 119 (1995)

[327] Vallee', J. P., A&A **308** 433 (1996)

[328] Vallee', J. P., ApJ **566** 261 (2002)

[329] Valls-Gabaud, D., Publ. Astron. Soc. Aust. **15** 111 (1998)

[330] van Dishoeck, E. F. & Black, J. N., ApJS **62** 109 (1986)

[331] Van Straten, W., Bailes, M., Britton, M., Kulkarni, S. R., Anderson, S. B., Manchester, R. N. & Sarkissian, J., Nature **412** 158 (2001)

[332] Vivekanand, M. and Narayan, R., A&A **3** 399 (1982)

[333] Verschuur, G. L., ARA&A **13** 257 (1975)

[334] Wainscoat, R. J., Cohen, M., Volk, K., Walker, H. J. & Schwartz, D. E., ApJS **83** 111 (1992)

[335] Walsh, W. M., astro-ph/0306075

[336] Wang, Q. D. and Yu, K. C., AJ **109** 698 (1995)

[337] Webster, A. S., MNRAS **166** 355 (1974)

[338] Weiner, B. J. & Williams, T. B., AJ **111** 1156 (1996)

[339] Weisberg, J. M., Rankin, J. and Boriakoff, V., A&A **88** 84 (1980)

[340] Wendker, H. J., A&A **4** 378 (1970)

[341] Westerhout, G., B.A.N **14** 215 (1958)

[342] Wilson, R. W. & Bolton, J. G., P.A.S.P. **72** 331 (1960)

[343] Wilson, T. L., Mezger, P. G., Gardner & F. F., Milne, D. K., A&A **6** 364 (1970)

[344] Wilson, T. L., Fazio, G. G., Jaffe, D., Kleinmann, D., Wright, E. L., Low, F. J., A&A **76** 86 (1979)

[345] Wilson T. L., *Radio recombination lines*, ed. Shaver P. A. & Reidel, Dordrecht, p. 205

[346] Wink, J. E., Altenhoff, W. J. & Mezger, P. G., A&A **108** 227 (1982)

[347] Wink, J. E., Wilson, T. L. & Bieging, J. H., A&A **127** 211 (1983)

[348] Witebsky, C., *COBE* NOTE # 5006, Internal Report (1978)

[349] Witebsky, C., *COBE* NOTE # 5013, Internal Report (1978)

[350] Yates, K. W.; Wielebinski, R., ApJ **149** 439 (1967)

[351] York, D. G., ApJ **213** 43 (1977)

[352] Zaldarriaga, M., ApJ **503** 1 (1998)

[353] Zanstra, H., ApJ **65** 50 (1927)